

**Towards a better understanding of the
impact of heart rate on the BOLD signal:
a new method for physiological noise
correction and its applications**

Dissertation

zur Erlangung des akademischen Grades
doctor rerum naturalium (Dr. rer. nat.)



vorgelegt dem Rat der Fakultät für Medizinischen
der Friedrich-Schiller-Universität Jena

Feliberto de la Cruz Monte de Oca
geboren am 14. August 1985 in Santiago de Cuba, Cuba

Gutachter

1. Prof. Dr. med. Karl-Jürgen Bär, Klinik für Psychosomatik und Psychotherapie,
Universitätsklinikum Jena
2. Prof. Dr. rer. nat. med. habil. Jürgen R. Reichenbach, Institut für Diagnostische und
Interventionelle Radiologie, Universitätsklinikum Jena
3. Prof. Dr. rer. nat. habil. Oliver Speck, Fakultät für Naturwissenschaften,
Otto-von-Guericke-Universität Magdeburg

Tag der öffentlichen Verteidigung: 24.11.2020

Table of contents

List of abbreviations	vii
Zusammenfassung	1
Summary	3
1 Introduction	5
1.1 Objectives and hypotheses	8
1.2 Thesis layout	9
2 Fundamentals	10
2.1 Physical principles of MRI	10
2.1.1 Relaxation mechanisms	12
2.1.2 MR Image formation	12
2.1.3 MRI sequences	14
2.2 The BOLD signal	15
2.3 fMRI methods to measure neural activity	17
2.3.1 Processing of fMRI data	18
2.4 Impact of physiological noise on the BOLD signal	20

2.4.1	Sources of cyclic respiratory noise	21
2.4.2	Sources of cyclic cardiac noise	23
2.4.3	Respiratory variations	24
2.4.4	Heart rate variations	24
2.5	Physiological noise correction methods	26
2.5.1	RETROspective Image CORrection (RETROICOR)	27
2.5.2	Respiration Volume per Time (RVT)	29
2.5.3	Response functions	30
2.6	Aliasing effects	34
3	Materials and Methods	35
3.1	Data acquisition and preprocessing	35
3.1.1	Subjects	35
3.1.2	Physiological recordings and analyses	36
3.1.3	MRI acquisition	38
3.1.4	MRI preprocessing	39
3.1.5	HR regressor	39
3.2	Analysis of heart rate and BOLD spectra	40
3.3	Analysis of cardiac response functions	42
3.3.1	Evaluation of group-specific CRF	44
3.3.2	Individual CRFs over different heart rates	45
3.4	Derivation of CRF from grey matter or cerebrospinal fluid	46
3.5	Noise correction on the default mode connectivity	47
3.6	Analysis of the influence of CRF on the CAN connectivity	48

4 Results	51
4.1 Physiological indices	51
4.2 Relationship between heart rate and BOLD spectra	52
4.3 Heart rate and cardiac response function	54
4.3.1 Evaluation	61
4.3.2 Change in the CRF shape as a function of heart rate	63
4.3.3 Introduction of the heart rate based CRF (CRF_{HR})	65
4.4 HR-based CRF derived from grey matter or cerebrospinal fluid	68
4.5 HR-based CRF for physiological noise correction	69
4.6 Association of functional connectivity in the CAN with heart rate	69
4.6.1 Effects of simulated aliasing on functional connectivity	73
5 Discussion	75
5.1 Heart rate and BOLD spectra	75
5.2 HR-based CRF	77
5.3 HR-based CRF in grey matter or cerebrospinal fluid	80
5.4 HR-based CRF as a physiological noise correction method	81
5.5 HR-based CRF and the central autonomic network	82
5.6 Limitations	85
6 Conclusions and Outlook	87
Appendix	89
A.1 Simulation pipeline	89
A.2 Variance explained at the individual level	90

References	x
Index of Figures	xxviii
Index of Tables	xxx
Ehrenwörtliche Erklärung	xxxi
Acknowledgements	xxxii
Curriculum Vitae	xxxiii

List of abbreviations

Greek Symbols

ε	random noise
π	$\simeq 3.14\dots$
φ_c	cardiac phase
ω_0	larmor frequency
φ_r	respiratory phase
σ^2	variance

SI units

Hz	Hertz
s	second

Acronyms / Abbreviations

ACC	anterior cingulate cortex
aI	anterior insula
ANS	autonomic nervous system
\vec{B}_0	main static magnetic field
BOLD	blood oxygenation level-dependent
bpm	beat-per-minute
CAN	central autonomic nervous
CBF	cerebral blood flow

CBV	cerebral blood volume
CMRO ₂	cerebral metabolic rate of oxygen consumption
CO ₂	carbon dioxide
CRF	cardiac response function
CRF _g	group-specific cardiac response function
CRF _{HR}	HR-based cardiac response function
CRF _i	individual cardiac response function
CSF	cerebrospinal fluid
ΔR_2^*	change in the effective transverse relaxation rate constant
dHb	deoxyhemoglobin
DVC	dorsal vagal complex
FC	functional connectivity
FHR	fast heart rate
fMRI	functional magnetic resonance imaging
FWHM	full-width at half-maximum
GS	whole-brain global signal
IBI	interbeat interval
HbO ₂	oxyhemoglobin
HR	heart rate
HRV	heart rate variability
LF/HF	ratio of low- to high-frequency components
\vec{M}	magnetization vector
MHR	medium heart rate
PCC	posterior cingulate cortex
PETCO ₂	end-tidal partial pressure of carbon dioxide

pI	posterior insula
PPG	photoplethysmogram
PSD	power spectral density
R^2	coefficient of determination
RETROICOR	retrospective correction in image domain
RETROKCOR	retrospective correction in k -space
RMSD	root-mean-square deviation
RMSSD	root-mean-square of successive IBI differences
RRF	respiratory response function
RSA	respiratory sinus arrhythmia
rs-fMRI	resting-state functional magnetic resonance imaging
RV	respiration volume
RVT	respiration volume per time
SCF	spontaneous skin conductance fluctuations
SCL	skin conductance level
SD	standard deviation
SHR	slow heart rate
T_2	transverse relaxation time constant
T_2^*	effective transverse relaxation time constant
TE	echo time
TR	repetition time
VLPFC	ventrolateral prefrontal cortex
VMPFC	ventromedial prefrontal cortex

Zusammenfassung

Funktionelle Magnetresonanztomographie (fMRT) ermöglicht die nicht invasive Untersuchung von Hirnaktivität und ist im Bereich der Neurobildgebung weit verbreitet. fMRT basiert auf dem BOLD-Kontrast (Blood Oxygenation Level-Dependent) der wiederum ein komplexes Zusammenspiel von Blutfluss, Blutvolumen und Sauerstoffverbrauch widerspiegelt. Physiologische Prozesse bewirken substantielle Fluktuationen im BOLD-Signal und verfälschen die zugrunde liegende neuronale Aktivität. Deshalb ist das Entfernen dieser Störeinflüsse ein maßgeblicher Schritt in der Vorbereitung von fMRT-Daten geworden.

Die Variation in der Herzfrequenz (HF) ist das Ergebnis sich gegenseitig beeinflussender physiologischer Mechanismen und stellt die bedeutsamste, aber nur wenig verstandene, physiologische Einflussgröße auf das BOLD-Signal dar. Die Nutzung einer Antwortfunktion, der *cardiac response function* (CRF), welche die HF-induzierten Signaländerungen optimal modelliert, ist eine effektive Methode, um Störungen durch die HF im BOLD-Signal zu reduzieren. Jedoch berücksichtigen gegenwärtige Ansätze zur Korrektur physiologischen Rauschens, namentlich die kanonische und individualisierte CRF, die Variationen der HF zwischen den Teilnehmern nicht. Jene Ansätze sind dadurch nicht auf Strichproben mit unterschiedlichen HF anwendbar oder benötigen zeitaufwendige Qualitätskontrollen einzelner physiologischer Aufnahmen sowie abgeleiteter CRF. Ein besseres Verständnis dafür, wie genau die HF und das BOLD-Signal zusammenhängen und inwiefern die Methoden zur Korrektur physiologischen Rauschens verbessert werden können, würde helfen nicht neuronale von neuronalen BOLD-Fluktuationen zu unterscheiden und somit die MRT-Methodik verlässlicher machen.

Durch die Analyse einer großen Stichprobe gesunder Probanden zeigen die Ergebnisse dieser Arbeit, dass verschiedene HF das BOLD-Signal und deren Frequenzspektren unterschiedlich beeinflussen. Ein weiteres Ergebnis ist, dass die HF einen bedeutenden Einfluss auf den Verlauf der CRF hat. Langsame HF führen zu glatteren CRFs mit einem einzelnen, definierten Maximum, während schneller HF ein zusätzliches Maximum hervorrufen. In dieser Arbeit wird eine neue Methode vorgeschlagen, welche diese Dependenz nutzt, um HF-induzierte Fluktuationen besser als bisher zu modellieren. Diese Methode, HF-basierte CRF genannt, beinhaltet zwei Funktionen: eine für HF unter 68/min und eine für HF über diesem Wert. HF-basierte CRFs können direkt auf fMRT-Daten angewendet werden, beachten dabei aber die interpersonellen Variationen der HF ohne aber individualisierte CRFs zeitaufwendig von jedem einzelnen Probanden zu bestimmen.

Die Leistung von HF-basierten CRFs zur Korrektur physiologischen Rauschens wurde anhand des am besten untersuchten, funktionellen Ruhe-Netzwerks im Gehirn, dem *default mode network*, quantifiziert. Die Konnektivität in diesem Netzwerk reduzierte sich durch Anwendung der HF-basierten CRFs stärker als durch etablierte Methoden. Dies deutet darauf hin, dass eine Überschätzung der Konnektivität durch HF-basierte CRFs vermieden werden kann. Da das zentrale Nervensystem das Herz beeinflusst, wurde ein weiterer Test durchgeführt, um den Einfluss auf die Gehirn-Herz-Interaktion zu bewerten. Diese Analyse ergab, dass die HF-basierte CRF ein geeignetes Modell zur Untersuchung dieser Interaktion in Ruhe darstellt. Nicht-neuronale Fluktuationen konnten verlustfrei entfernt werden, ohne dabei Signalvarianz, welche der neuronalen Aktivität zugeordnet werden kann, einzubüßen.

Diese Arbeit zeigt, dass die HF als ein wichtiger physiologischer Faktor, welcher das BOLD-Signal beeinflusst, in fMRT-Analysen generell berücksichtigt werden sollte. Weiterhin wurde mit der neuen Methode der HF-basierten CRF ein wertvolles Werkzeug zur effektiven Korrektur physiologischen Rauschens in fMRT-Untersuchungen vorgestellt.

Summary

Functional magnetic resonance imaging (fMRI) based on blood oxygenation level-dependent (BOLD) contrast allows non-invasive examination of brain activity and is widely used in the neuroimaging field. The BOLD contrast mechanism reflects hemodynamic changes resulting from a complex interplay of blood flow, blood volume, and oxygen consumption. Physiological processes influencing these parameters cause substantial fluctuations in the BOLD signal, which may obscure the underlying neural activity. Thus, the separation of noise from the signal has become a crucial step in the preprocessing of fMRI data.

Heart rate (HR) variations are the most intriguing and less understood physiological processes affecting the BOLD signal, as they are the result of a wide variety of interacting factors. The use of the response function that best models HR-induced signal changes, called cardiac response function (CRF), is an effective method to reduce HR noise in fMRI. However, current models of physiological noise correction based on CRF, i.e. canonical and individual, either do not take into account variations in HR between subjects, and are thus inadequate for cohorts with varying HR, or require time-consuming quality control of individual physiological recordings and derived CRFs. Gaining deeper insight into the precise association between HR and the BOLD signal, as well as improving physiological noise correction methods, will help to separate non-neural from neural-related fluctuations, thus making the fMRI technique more reliable.

By analyzing a large cohort of healthy individuals, the results presented in this thesis show that different HRs influence the BOLD signal and their corresponding spectra differently. A further finding is that HR plays an essential role in determining the shape of the CRF. Slower HRs produce a smoothed CRF with a single well-defined maximum, while faster HRs cause a second maximum. Taking advantage of this dependence of the CRF on HR, a novel method is proposed to model HR-induced fluctuations in the BOLD signal more accurately than current approaches of physiological noise correction. This method, called *HR-based CRF*, consists of two CRFs: one for HRs below 68 bpm and one for HRs above this value. HR-based CRFs can be directly applied to the fMRI data without the time-consuming task of deriving a CRF for each subject while accounting for inter-subject variability in HR response.

The performance of HR-based CRF as physiological noise correction method was tested in the most widely studied brain network at rest, the default mode network. Here, HR-based CRFs

reduced noise more efficiently than traditional correction methods, suggesting that overestimation of functional connectivity can be avoided by applying these new functions. Because of the well-known influence of the central nervous system on the heart, a further test was performed to assess the impact of HR-based CRFs on brain-heart interaction. This analysis revealed that HR-based CRF is an appropriate model to investigate this interaction at rest. More specifically, the functions removed non-neuronal fluctuations without sacrificing signal variance attributable to neural activity associated with cardiac control.

To conclude, this thesis shows that HR is a crucial physiological factor influencing the BOLD signal, which always has to be considered when analyzing fMRI data. Moreover, the novel introduced HR-based CRF method is a valuable tool to remove HR noise in fMRI studies efficiently.

1 Introduction

Functional MRI based on the BOLD contrast has become a powerful tool for mapping the human brain. However, BOLD signal fluctuations in a given brain area are induced not only by changes in the metabolic demand related to neural activity but also by different physiological processes. In particular, the cardiac and respiratory cycles [68, 203, 252], and the non-periodic variations in heart rate (HR) [53, 135, 221] and respiration rate/depth [26, 25], are often considered as potential confounding factors of the BOLD signal. These factors modulate the transfer function between neural and BOLD signals [153], thus compromising the reliability of the latter as a surrogate of neural activity.

Given the fact that fractional changes of the BOLD signal related to neural activity are in the order of a few percent in most functional tasks [130], the separation of the signal from noise has become a crucial step in the preprocessing of BOLD data. Particularly, non-periodic variations in HR and respiration have received particular attention as they lie in the frequency band of interest of the resting-state BOLD signal (<0.1 Hz). For these signals, much progress has been made in noise correction techniques using deconvolution and by assuming a common physiological response among the population, e.g. canonical cardiac (CRF) and respiratory (RRF) response functions [53, 98]. However, the use of a canonical response function, for which the parameterization is known beforehand and fixed for all datasets, makes this physiological noise correction inflexible to different conditions by ignoring inter-subject variation in physiological response [137, 81].

An alternative to canonical models is the use of individual response functions (CRF_i and RRF_i), as proposed by Falahpour *et al.* [81], and further extended by Cordes *et al.* [64] and Golestani *et al.* [98]. Falahpour *et al.* [81] derived the CRF_i and RRF_i from averaged tissue signals (e.g. whole-brain, white matter, and gray matter) and showed that CRF_i accounted for more variance in the BOLD signal than the canonical CRF. Cordes *et al.* [64] suggested that to determine an optimal CRF_i , the model needs to explicitly include a derivative term to model the second peak found in some CRF_i . Nonetheless, while these approaches address the aforementioned inter-subject variability issue, noise-free physiological recordings are required

for each subject, which is not always possible. Besides, it is well-known that deconvolution techniques are highly sensitive to noise in the recorded signals and, therefore, do not always lead to plausible response functions. Also, a significant presence of physiological noise in the reference tissue is needed to derive “good” response functions. Furthermore, the estimation of individual response functions is a time-consuming task as each estimated response function needs to be reviewed to avoid inconsistent results. Thus, a more in-depth analysis is needed to develop a model that can efficiently separate noise from meaningful BOLD signal fluctuations, and thus increasing confidence in fMRI findings.

Previous work estimating CRF_i showed that the shape of CRF_i varied in accordance with the subject’s HR [64, 81]. Interestingly, one of the most reproducible findings in those studies was the presence of a second maximum at about 17 s in some CRF_i , which was ignored by the authors in [64, 81] and suggested the need for a more comprehensive analysis. Overall, it appears that HR is an essential factor determining the shape of the CRF_i , suggesting that it has to be considered when analyzing large cohorts of subjects with different HRs.

Physiological processes can also influence the BOLD signal through aliasing. At low sampling rates, noise contributions from the cardiac and respiratory cycles can alias into the low-frequency range (<0.1 Hz) of the BOLD signal thought to be responsible for resting-state functional connectivity (FC) [32, 155]. Repetition times (TR) of the MR sequence below 0.3 s or even shorter are needed to obtain fMRI data entirely free of aliasing. Such requirements are hard to meet for whole-brain acquisition, implying that aliased fundamental cardiac frequency and harmonics compromise estimates of brain activity, such as FC. Despite being a major concern for resting-state fMRI (rs-fMRI), there are surprisingly few studies examining the effects of cardiac aliasing on FC.

While the studies above treat HR explicitly as a source of noise, another line of work approaches this topic from a different perspective, considering physiological fluctuations in BOLD data as components of interest. One reason to consider HR-induced fluctuations as a meaningful part of the BOLD signal is the direct influence of the autonomic nervous system on HR. In particular, the central autonomic network (CAN), a term coined by Benarroch to describe a group of cortical and subcortical brain regions involved in the generation of autonomic responses, is responsible for HR variations [21, 20]. The CAN outflow is mediated through preganglionic sympathetic and parasympathetic neurons that innervate the heart via the stellate ganglia and vagus nerve. The interplay of both sympathetic and parasympathetic inputs to the sinoatrial node is the source of the complex variability that characterizes the HR time series [213]. As a consequence, the signal variance explained by HR contains relevant information and can be used to investigate brain correlates of cardiac autonomic regulation [176, 103].

In 2000, Thayer and colleagues developed the Neurovisceral Integration Model to provide a theoretical framework linking cardiac regulation, through activation of the CAN, to cognitive and emotional regulation [237, 238]. This model comprises not only central autonomic nuclei within the brainstem or limbic structures, i.e. insula or amygdala, but also cortical structures, including the anterior and posterior cingulate cortices (ACC and PCC) and the ventromedial prefrontal cortex (VMPFC) [237, 238]. The cortical brain regions, especially the VMPFC, exert top-down control on the response of subcortical structures forming an interconnected network that modulates the activity of subcortical/brainstem downstream regions. Brainstem regions, in turn, regulate autonomic input to the heart by modulating the parasympathetic/sympathetic balance.

The brain-heart interaction is evidenced during fMRI tasks, particularly in those involving physical and mental efforts, where the task elicits substantial changes in autonomic outflow that affect the cardiovascular system [182, 222]. However, such experiments have the inconvenience of producing large subject's movements that may obscure the specific neural response. Similarly, if the task elicits more than one process, e.g. simultaneously demanding cognitive/mental effort and motor activity, the autonomic-controlled cardiovascular adjustments evoked by each process are challenging to disentangle. Analysis of resting-state fMRI data avoids these issues but has the problem of eliciting lower autonomic activity, making the brain-heart interaction hard to detect. Moreover, non-neuronal physiological fluctuations represent a further confound for studies investigating the association of FC and HR responses. This last issue is particularly problematic for CAN regions, such as the PCC and VMPFC. These regions are also part of the so-called default mode network (DMN), which exhibits high neural activity at rest [202] and is extremely sensitive to physiological noise [228, 245]. Appropriate modeling of physiological noise would, therefore, be of great benefit to studies investigating brain-heart interactions during resting-state conditions.

1.1 Objectives and hypotheses

The study of brain-heart interactions is challenging, as non-neuronal cardiac processes, especially HR variations resulting from systemic physiological changes, obscure neural substrates of cardiac regulation. Separating non-neural HR-induced fluctuations from neural-activity-related fluctuations in the BOLD signal is, however, essential for the correct interpretation of functional connectivity and for uncovering neural correlates of cardiac control.

Up to date, the impact of different HRs on the BOLD signal is poorly understood. Current methods for reducing HR-induced fluctuations in the BOLD signal rely on the use of canonical or individual CRFs, which may not be suitable for large subject cohorts with different HRs. Indeed, a canonical CRF, as proposed by Chang *et al.* [53], is unlikely to adequately explain a wide range of HRs because it has been derived from a few subjects with a narrow HR range. Likewise, individual CRFs require careful correction of external physiological recordings as well as a post-inspection of the derived CRF shape, which is time-consuming and highly dependent on expertise.

Thus, the main objective of this thesis is to investigate how different HRs influence the BOLD signal and to extend current models of physiological noise correction to improve the reduction of HR-induced fluctuations.

Given that different HR signals have different frequency spectra, and HR-induced fluctuations are present throughout the whole brain [53, 221], I hypothesize that:

- i** Differences in the frequency spectrum of slow and fast HR signals are reflected in spectral properties of the BOLD signal throughout the whole brain.

Based on the works of Falahpour *et al.* [81] and Cordes *et al.* [64], which showed differences in the shape of individual CRFs, I further hypothesize that:

- ii** HR influences the shape of the individual CRF.

Assuming that hypothesis **ii** is confirmed, it is possible to develop a model that account for the influence of HR on the CRF shape. This model will be referred to as HR-based CRF.

The main idea underlying this thesis is that CRF mainly models non-neural sources. This assumption implies that HR-based differences of the CRF are present in brain regions containing or not containing neural signatures, such as the gray matter (GM) or the cerebrospinal fluid (CSF). Therefore, I hypothesize that:

iii There are HR-based differences of the CRF in both GM and CSF.

As data are acquired in the resting-state condition, I also hypothesize that:

iv HR-based CRFs reduce spurious correlations within the default mode network more efficiently than the canonical CRF.

There is a well-defined set of brain regions involved in central control of autonomic function, the so-called central autonomic network (CAN) [18, 236, 238, 237]. It has been shown that core regions of CAN modulate heart rate, and their functional connectivity relates to HR variability changes [209, 128]. In order to prove that the use of HR-based CRFs does not affect brain-heart interaction, I further hypothesize that:

v Physiological noise correction via HR-based CRFs does not weaken the association between heart rate and functional connectivity in the CAN.

1.2 Thesis layout

The rest of this thesis is organized as follows. Chapter 2 provides the theoretical background required to understand the content of this thesis. These include the basis of MRI and the BOLD mechanism, the fMRI methods used to measure neural activity, the primary sources of physiological noise affecting the BOLD signal, and the most popular methods of physiological noise correction. Chapter 3 describes the materials and methods, while chapter 4 presents the results of the study. Both chapters follow the progression of the research necessary to answer the hypotheses formulated in section 1.1. Chapter 5 presents the discussions and limitations of the research findings. This chapter is separated to discuss each section of the results chapter accordingly. Finally, Chapter 6 summarizes the key findings and indicates directions for future work.

Most of the results presented in this thesis have been published in the following peer-reviewed articles:

- **de la Cruz et al.**, “The relationship between heart rate and functional connectivity of brain regions regions involved in autonomic control.” *NeuroImage*, 196 (2019), pp. 318-328.
- **de la Cruz et al.**, “Impact of the heart rate on the shape of the cardiac response function.” *NeuroImage*, 162 (2017), pp. 214-225.

2 Fundamentals

This chapter briefly summarizes the foundations of MRI and the BOLD mechanism that are required to understand the remaining part of the work. Further topics include a description of fMRI methods used to measure neural activity and the most common fMRI data processing strategies. Particular attention should be paid to the section on the influence of physiological noise on the BOLD signal, where the primary sources of physiological noise are explained in detail. The following section presents a summary of the most popular physiological noise correction methods using external recordings with a particular focus on linear models. The chapter ends with a brief discussion of the aliasing of physiological signals.

2.1 Physical principles of MRI

MRI takes advantage of the fact that the nuclei of some atoms, such as hydrogen (^1H), fluorine-19 (^{19}F), oxygen-17 (^{17}O) or phosphorus-31 (^{31}P), act like spinning magnets. When placed in a strong magnetic field (\vec{B}_0), they partially align with \vec{B}_0 and precess at a frequency ω_0 (also known as the Larmor frequency) that depends on the strength of \vec{B}_0 :

$$\omega_0 = \gamma B_0, \quad (2.1)$$

where γ is the gyromagnetic ratio specific for a given nucleus.

Among the nuclei in the human body, ^1H shows the highest γ ($\sim 2.68 * 10^8 \text{ rad} \cdot \text{s}^{-1} \cdot \text{T}^{-1}$) and is present in biological tissues in great abundance, making ^1H the most frequently imaged nucleus in MRI. If the net magnetization \vec{M} (the resultant sum of all spins, see Figure 2.1A) receives a brief radio frequency (rf) pulse \vec{B}_1 tuned to its Larmor frequency, it tips away from the static magnetic field \vec{B}_0 , emitting energy in an oscillatory fashion as it gradually returns to the equilibrium position with \vec{B}_0 [34, 200]. This signal is called free induction decay (FID) and can be detected by a coil surrounding the sample according to the Faraday's law of electromagnetic

induction. The changing magnetic field due to the precession of the tipped \vec{M} induces an electromotive force (*emf*) in the receiver coil given by [110]:

$$emf = -\frac{d}{dt} \int_V \vec{M}(\vec{r}, t) \vec{B}^{receiver}(\vec{r}) d^3r, \quad (2.2)$$

where $\vec{B}^{receiver}(\vec{r})$ is the magnetic field per unit current produced by the receiver coil at position \vec{r} , and V denotes the sample volume. The MR signal is the *emf* caused by the changing magnetic field across the receiver coil.

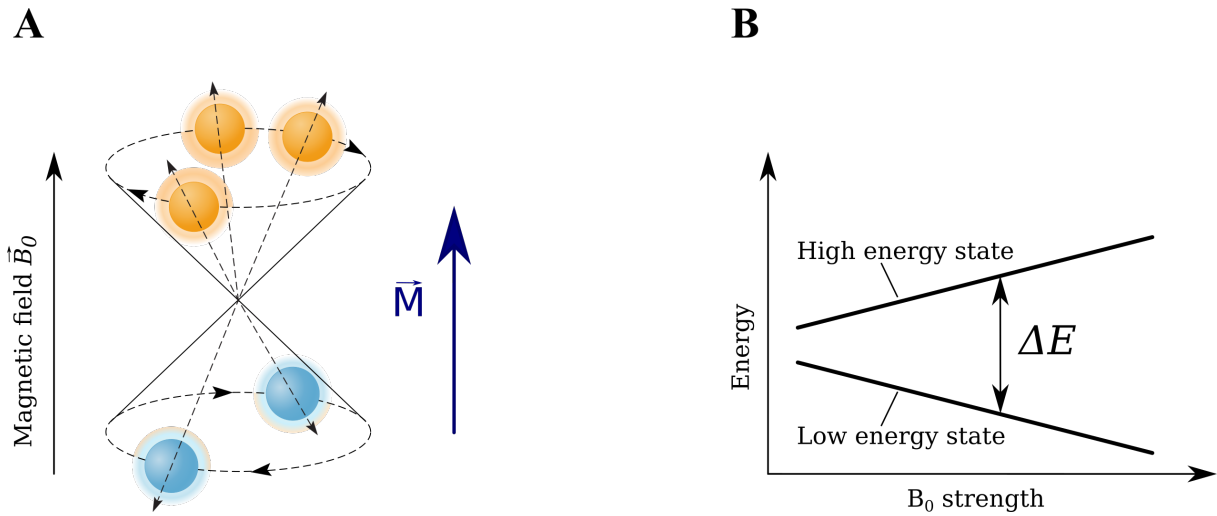


Figure 2.1: **A)** The net magnetization (\vec{M}) is determined by the difference between the number of spins in the low energy level (parallel alignment to \vec{B}_0) and the number of spins in the high energy level (anti-parallel alignment to \vec{B}_0). **B)** Energy-level diagram describing the Zeeman effect for a nucleus with spin $\frac{1}{2}$ (e.g. ^1H). The energy difference (ΔE) between the low and high energy level increases with the strength of \vec{B}_0 . As the energy difference between the states increases, spins are more likely to remain in the lower energy state. Figure adapted from Huettel *et al.* [124].

It should be pointed out that only a small part of the nuclear spin ensemble contributes to the measured signal, as the nuclear spins align differently in the magnetic field \vec{B}_0 due to the Zeeman effect (see Figure 2.1B). Some nuclear spins remain at a low energy level (with a parallel alignment to \vec{B}_0) while others occupy a high energy level (with an anti-parallel alignment to \vec{B}_0). The fraction of spins in the lower energy level depends on the strength of \vec{B}_0 as well as temperature, and is predicted by the Boltzmann distribution:

$$\frac{N_{\uparrow}}{N_{\downarrow}} = \exp\left(\frac{\Delta E}{kT}\right), \quad (2.3)$$

where N_{\uparrow} and N_{\downarrow} represent the number of spins with parallel and anti-parallel alignment with respect to \vec{B}_0 , respectively, ΔE represents the difference in energy between the two states and is

proportional to B_0 , k is the Boltzmann constant (1.381×10^{-23} joules/ $^\circ K$), and T is the absolute temperature in degrees Kelvin.

2.1.1 Relaxation mechanisms

During the recovery of the magnetization along the \vec{B}_0 direction, or z-axis, the energy that the spin system absorbed from the rf pulse is redistributed with its surroundings. This process is called spin-lattice, or longitudinal relaxation, and is governed by a specific relaxation time constant T_1 . Another interaction occurs among the spins themselves that causes dephasing resulting in a reduction of transverse magnetization \vec{M}_{xy} (net magnetization vector perpendicular to \vec{B}_0). This interaction is called spin-spin relaxation, or transverse relaxation, and is governed by the relaxation time constant T_2 . Under experimental conditions, the spin-spin relaxation is also affected by interactions with local magnetic field inhomogeneities. This observed, or “effective“, transverse relaxation time constant T_2^* is always shorter than T_2 . The equation of motion of the net magnetization vector is given by the Bloch equations [34] and describes the changes in net magnetization as the sum of three terms:

$$\frac{d\vec{M}}{dt} = \vec{M} \times \gamma \vec{B} + \frac{1}{T_1} (M_0 - M_z) \hat{k} - \frac{1}{T_2} (M_x \hat{i} + M_y \hat{j}), \quad (2.4)$$

where \hat{i} , \hat{j} and \hat{k} are unit vectors in the x , y , z directions.

The first term indicates that \vec{M} precesses around the main axis of the magnetic field at a rate given by both the γ and the field strength. The second term states that the longitudinal component of the net magnetization M_z recovers at a rate given by T_1 , while the last term reveals that the transverse component of the net magnetization decays at a rate given by T_2 . The Bloch equations form the basis for the quantitative description of the MR phenomena [123].

2.1.2 MR Image formation

To form an MR image, it is further required to encode the position of the object of interest. The encoding is achieved by superimposing magnetic field gradients along the three orthogonal different spatial axes (Figure 2.2), causing the atomic nuclei to precess at different frequencies [146, 162]. Magnetic field gradients modulate the strength of the main static field \vec{B}_0 (usually in a linear fashion) but not its direction. Now, the magnitude of the total magnetic field \vec{B} experienced by a spin system at a given spatial position (x, y, z) and time point (τ) is a

superposition of the static field and the field gradients:

$$B(\tau) = B_0 + G_x(\tau)x + G_y(\tau)y + G_z(\tau)z \quad (2.5)$$

where G_x , G_y , and G_z are the magnetic field gradients along the x -, y -, and z -axes, respectively. The time dependence of G reminds us that the gradients may change during an experiment.

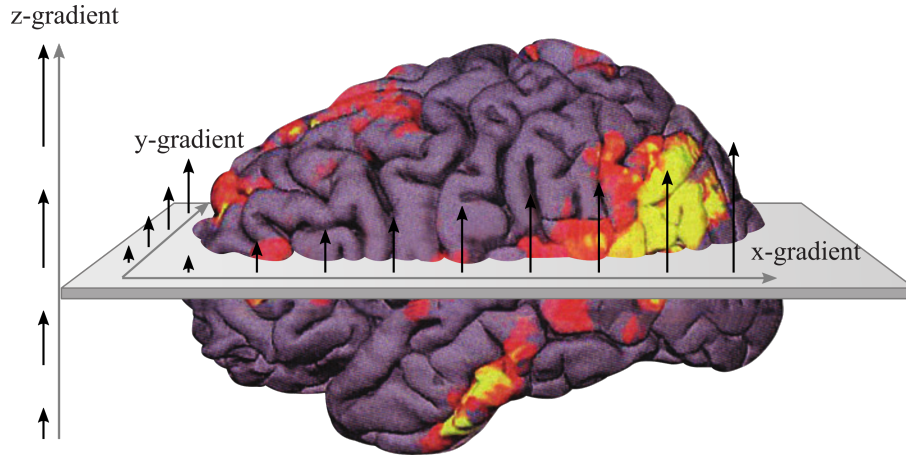


Figure 2.2: Schematic illustration of the magnetic field gradients along the three orthogonal spatial axes x , y , and z . Each of these gradients changes the strength of \vec{B}_0 along the relevant axis but does not alter its direction. Figure adapted from Huettel *et al.* [124].

The spatial dependence of the Larmor frequency produced by the magnetic field gradients can be used to acquire information about the spatial distribution of the atomic nuclei. For example, the acquired MR signal from an object in the presence of a set of three orthogonal gradients can be written as [110]:

$$S(t) = \int_x \int_y \int_z dx dy dz \rho(x, y, z) e^{-i\gamma \int_0^t (G_x(\tau)x + G_y(\tau)y + G_z(\tau)z) d\tau}, \quad (2.6)$$

where $\rho(x, y, z)$ is the spin density at spatial location (x, y, z) and is proportional to the equilibrium magnetization $M_0(x, y, z)$. Equation 2.6 expresses the relationship between the acquired signal, $S(t)$, and the properties of the object, $\rho(x, y, z)$. This equation can be conveniently rewritten in terms of k -space coordinates as [110]:

$$S(k_x, k_y, k_z) = \int_x \int_y \int_z dx dy dz \rho(x, y, z) e^{-i2\pi(k_x x + k_y y + k_z z)} \quad (2.7)$$

where now the time dependence resides implicitly in the spatial frequencies k_x , k_y , k_z with:

$$k_x(t) = \frac{\gamma}{2\pi} \int_0^t G_x(\tau) d\tau, \quad k_y(t) = \frac{\gamma}{2\pi} \int_0^t G_y(\tau) d\tau, \quad k_z(t) = \frac{\gamma}{2\pi} \int_0^t G_z(\tau) d\tau \quad (2.8)$$

The k -space is an array of numbers representing the spatial frequency content of the imaged object. From Equation 2.7, it becomes clear that k -space and image space, $\rho(x, y, z)$, have a straightforward relationship, that is, they are (3D) Fourier transforms of each other. By applying the inverse Fourier transform, we can convert k -space data into an image, a process known as image reconstruction. Conversely, by applying a forward Fourier transform, we can convert image-space data into k -space data [124].

2.1.3 MRI sequences

As explained above, by applying an rf pulse for a short period, the magnetization can be rotated. If the protons are initially aligned along the z -axis, an rf pulse along the x -axis rotates the magnetization from the z -axis onto the y -axis. This pulse is referred to as a 90-degree pulse since it rotates the magnetization by 90 degrees. When the 90° rf pulse stops, the magnetization in the xy plane decays due to T_2^* relaxation, inducing an FID. The FID can be manipulated to generate a new MR signal called the "echo" or, more specifically, gradient-echo (GE) signal since it is produced by dephasing and rephasing gradients [77]. An alternative to the GE signal is the spin-echo (SE) signal [113]. The SE signal is generated by adding a refocusing 180° rf excitation pulse after the 90° pulse, thus removing the T_2^* effects. Figure 2.3 shows both sequences.

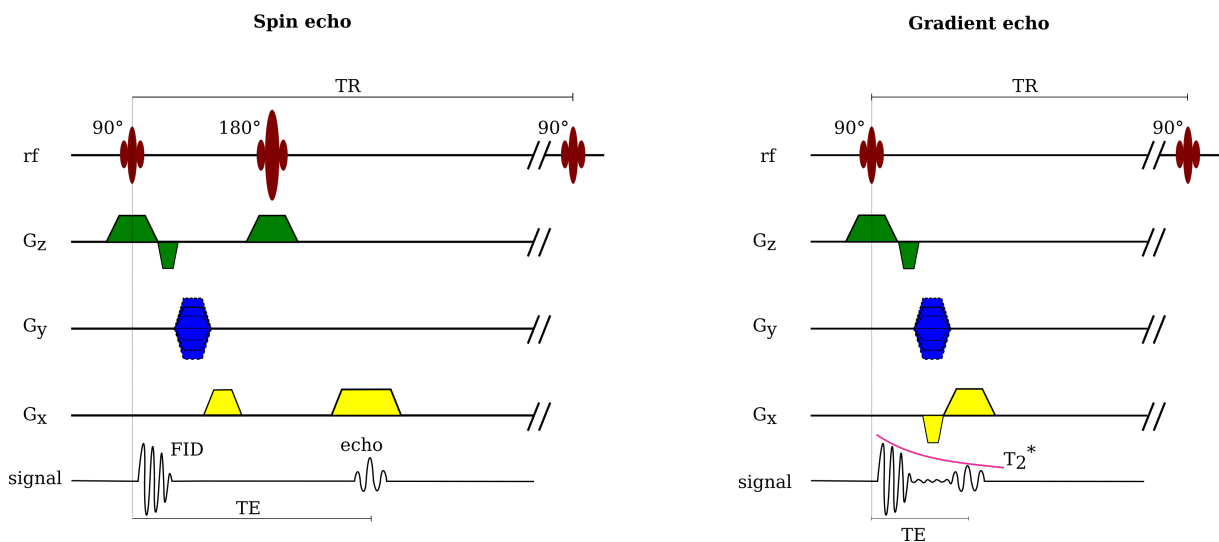


Figure 2.3: Pulse diagram of the spin-echo and gradient-echo sequences including the spatial localization gradients. The slice-select gradient G_z is on during excitations. G_y represents the phase-encoding gradient and G_x the frequency-encoding gradient. The echo time TE is the time between the 90° rf pulse and the maximum of the echo. The repetition time TR or sampling rate is the time between successive 90° pulses and controls the temporal resolution. In the GE sequence, the echo is formed within the FID, which means that T_2^* dephasing occurs and a short TE is needed.

GE and SE MRI sequences use single or multiple excitation pulses (shots) to fill the k -space data required for image reconstruction. Multi-shot imaging sequences produce high-quality

images compared to single-shot techniques but require longer scan times. Single-shot techniques like echo-planar imaging (EPI) [163] are particularly useful for fMRI as they are very rapid and relatively robust against motion artifacts. EPI is a fast imaging technique in which multiple echoes of different phase steps are acquired using rephasing gradients (Figure 2.4, left). To fill k -space, conventional EPI uses an atypical pattern in which alternating lines are scanned in opposite directions (Figure 2.4, right). Gradient-echo EPI (GE-EPI) is especially suitable for fMRI studies due to its intrinsic T_2^* -weighting. The reason is that an activated brain area exhibits a temporary increase in signal on T_2^* -weighted images as a result of a decrease in the relative concentration of deoxyhemoglobin (see section below for further details). For fMRI, a 2D multi-slice GE-EPI acquisition scheme covering the brain area of interest is repeated over time, resulting in an fMRI time series of hundreds of 3D brain images (volumes).

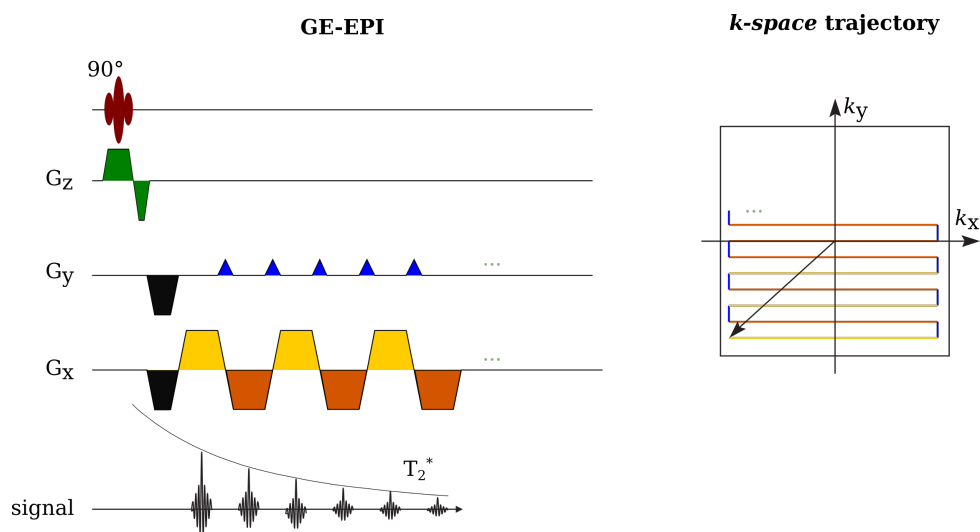


Figure 2.4: A standard 2D GE-EPI pulse sequence (left) and its k -space trajectory (right). The initial negative gradients G_x and G_y bring the trajectory to the lower left corner of k -space, as indicated by the black arrow. Afterward, strong switched frequency-encoding gradients are applied simultaneously with intermittently "blipped" low-magnitude phase-encoding gradients, resulting in a "zig-zag" traversal of k -space. Positive frequency-encoding gradients (yellow) swept k -space from left-to-right, while negative gradients (orange) from right-to-left. The blipped low-magnitude phase-encoding gradients (blue) are responsible for the step-wise increase along the k_y -axis. Gradient echoes are collected with each oscillation of the frequency-encoding gradient G_x . Gradients are shown in different colors for easy comparison between the pulse sequence and its k -space representation.

2.2 The BOLD signal

One type of fMRI signal that has become a valuable tool to examine neural activity is the so-called BOLD contrast [184, 185]. Although there are other techniques for assessing regional brain function non-invasively, such as arterial spin labeling for cerebral blood flow and MR spectroscopy for metabolite analysis, BOLD fMRI has emerged as the most popular technique

due to its ease of use, comparatively low cost, and wide availability [4]. The BOLD contrast is considered to be an indirect measure of neural activity and results from a complex interplay of multiple physiological factors, including cerebral blood flow (CBF), cerebral blood volume (CBV), and cerebral metabolic rate of oxygen consumption ($CMRO_2$) [39, 48]. The biophysical basis of the BOLD effect is that increased neural activity causes local dynamic changes in the relative concentrations of oxyhemoglobin (HbO_2) and deoxyhemoglobin (dHb) in cerebral vessels [184]. In contrast to its oxygenated counterpart, dHb is paramagnetic due to its four unpaired electrons and alters the susceptibility of the blood. In the presence of a magnetic field, dHb creates local magnetic field gradients, which shorten the transverse relaxation time of protons within the extra- and intra-vascular tissue locally (see Figure 2.5A). MR imaging takes advantage of this effect by acquiring T_2 - or T_2^* -weighted images, where increases in the concentration of dHb will result in loss of signal intensity [185].

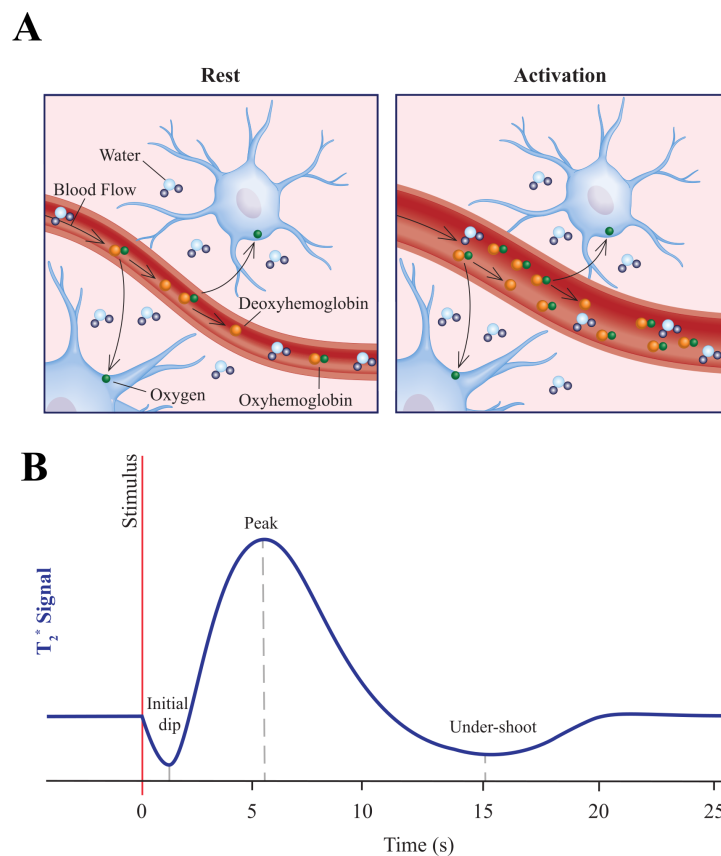


Figure 2.5: The BOLD fMRI mechanism. **A)** When neural activation takes place, the blood flow of the surrounding vasculature increases. This alters the ratio of non-paramagnetic oxyhemoglobin to paramagnetic deoxyhemoglobin leading to changes in the magnetization of water protons in and around small vessels (Figure adapted from Raichle *et al.* [201]). **B)** Illustration of the BOLD fMRI signal response during neural activity.

Moreover, neurons rely exclusively on the glucose and oxygen available in the bloodstream for their proper functioning. Both molecules are efficiently delivered by the vascular system.

When neural activation occurs in a certain brain region, local blood flow increases to meet demand thanks to a mechanism called neurovascular coupling. This increase in blood flow is delayed by about 2 s, which is the time required for oxygenated blood to travel from arteries to capillaries and draining veins [142]. During the first 2 s before measurable hemodynamic changes occur in response to neural activation, neurons make use of the local reservoir of oxygen. This process is observed as a “dip” in the BOLD response or a decrease in the BOLD fMRI signal intensity due to the transient increase of dHb (see Figure 2.5B) [79, 166]. Following, an increase in the local cerebral blood flow and volume occurs due to vasodilation of arterioles, capillaries, and venules close to the activated neurons. Importantly, the delivery of oxygen by the vascular system by far exceeds the amount of oxygen extracted from the tissue, thus reducing the concentration of dHb in the blood, which translates to an increased BOLD signal. The hemodynamic response reaches a peak at around 5-6 s and then progressively returns to baseline, although a prolonged post-stimulus undershoot is frequently observed, possibly due to a sustained increase in CMRO₂ [248] or uncoupling between CBF and CBV [161, 49]. The release of glucose and oxygen to active neurons is faster than that to inactive neurons. This peculiarity constitutes the basis of the BOLD signal, that is, the surplus of HbO₂ in the active area and the dynamic changes in oxy- and deoxyhemoglobin concentrations results in a measurable MRI signal. The signal change of the BOLD response to neural activity increases with higher MR field strengths since the value of the transverse relaxation rate (R_2^*) and its change (ΔR_2^*) also increases with field strength.

2.3 fMRI methods to measure neural activity

Task-based and resting-state are two popular fMRI methods that use the BOLD contrast for measuring and mapping brain activity. Task-based fMRI measures brain hemodynamic changes to explore regions that are functionally involved in a specific task [11, 142, 186]. For this purpose, two comparative measurements are performed - the target and the control condition. Analyzing the BOLD signal differences between the target task (e.g. performing a naming task) and the control condition allows identification of brain regions responding to the given task.

Resting-state fMRI (rs-fMRI) measures spontaneous brain activity that occurs when no explicit task is performed [32]. Contrary to task-based fMRI, rs-fMRI does not rely on a comparison of experimental task and baseline conditions; instead, it detects regions whose BOLD signal fluctuations show a high degree of temporal correlation and presumably belong to a tightly coupled neural network [105]. Another difference between rs-fMRI and task-based fMRI is the processing strategies. For example, unlike task-based fMRI, resting-state measurements cannot be averaged over block intervals to reduce random noise.

Rs-fMRI focuses on spontaneous low-frequency fluctuations in the BOLD signal occurring below 0.1 Hz. Although recent studies have demonstrated the presence of resting-state BOLD signals at frequencies above 0.15 Hz [60, 152], the vast majority of rs-fMRI studies still focus on the <0.1 Hz range. As the underlying neural activity in resting-state is poorly understood, it is difficult to determine to what extent the >0.1 Hz signals are either generated by neuronal activity or reflect other hemodynamic and physiological processes [149]. Another argument against the use of the >0.1 Hz range is that physiological noise contributions to functional connectivity (FC) are more prominent than at <0.1 Hz [59].

The resting-state BOLD signal can be used to examine the FC between specific brain regions [89]. FC refers to the statistical dependence between the activities of two brain regions without any assumption of the mechanism by which these relationships are mediated [85, 88]. FC is the most used method in resting-state studies due to its simplicity, as it does not require any paradigm. Techniques used to assess FC include independent component analysis (a method that blindly separates mixtures of independent source signals; [19, 126]), coherence [231], or the widely used seed correlation analysis [10].

2.3.1 Processing of fMRI data

Once the fMRI data have been acquired, the first stage of the analysis involves data preprocessing. Task-fMRI and rs-fMRI share many preprocessing steps, but rs-fMRI requires additional ones, as it is particularly sensitive to noise given the nature of the resting-state signal. In rs-fMRI, the main aim of preprocessing is to prepare data for FC analysis by reducing the influence of artifacts. A summary of the most frequently preprocessing steps for fMRI is given below [196, 123].

Motion correction

Motion correction, also known as realignment of fMRI time series, is generally the first preprocessing step applied to all fMRI data. The goal of motion correction is to reduce the influence of head motion in the fMRI signal. It is always necessary because small head movements are inevitable. Motion correction works by aligning each scan (image) separately to a chosen reference scan with the least amount of motion artifact [66]. This correction usually considers head movements as a rigid body process, where an affine transformation is sufficient to capture them.

Slice timing correction

Slice timing correction is an optional step in the preprocessing of rs-fMRI, which can be omitted for data with high temporal resolution $TR < 2$ s [120]. This step aims to correct for the slight difference in the time at which each image slice was acquired. Slice timing correction uses interpolation in time to shift the fMRI time series so that all slices appear as if they had been acquired at the same point in time. In practice, one could consider performing slice-timing correction before realignment if one uses either a complex slice order sequence or expects moderate head movements [224].

Spatial smoothing

A further step commonly applied to fMRI data in the preprocessing pipeline is to apply some amount of spatial smoothing to the image to increase the signal-to-noise ratio. Spatial smoothing relies on the assumption that most of the spatial noise is Gaussian, independent from voxel to voxel, and roughly centered around zero. Spatial smoothing is achieved by convolving the image with a 3D Gaussian function of the form:

$$f(x, y, z) = \exp\left(-\left(\frac{x^2}{2\sigma_x^2} + \frac{y^2}{2\sigma_y^2} + \frac{z^2}{2\sigma_z^2}\right)\right), \quad (2.9)$$

where σ_x , σ_y and σ_z are the standard deviations of the Gaussian kernel in each direction. The amount of spatial smoothing that is applied is usually defined by the full-half-width-maximum (FWHM) of the Gaussian kernel, where $FWHM \approx 2.35\sigma_{x|y|z}$. An FWHM of twice the voxel dimensions is found acceptable for fMRI data [196].

Temporal filtering

Temporal filtering is the next conventional preprocessing step applied to fMRI data. Temporal filtering is applied to remove unwanted signal components from the fMRI time series. FMRI data is high-pass filtered to remove very low frequencies (<0.01 Hz), such as slow scanner drifts and physiological fluctuations due to changes in basal metabolism, and low-pass filtered to remove cyclic respiratory and cardiac artifacts (>0.1 Hz).

Registration/Normalization

Registration is a preprocessing step necessary to perform group-level analyses. Here, fMRI data are aligned and warped into a common standard space, e.g. Talairach [234] or Montreal Neurologic Institute (MNI) [80], in order to match up their spatial structures.

Nuisance regression

Nuisance regression is a commonly adopted step in the preprocessing of fMRI data. The term nuisance is used to describe regressors that model BOLD signal fluctuations of no interest. Regressors may include head-motion parameters time series, physiological signals, and signals from non-gray matter tissues, such as white matter and cerebrospinal fluid (CSF). All these regressors are removed from the fMRI time series of each voxel using multiple regression [157]. Sources of physiological noise and their removal will be discussed in more detail in the following sections.

2.4 Impact of physiological noise on the BOLD signal

Physiological noise refers to the fMRI signal changes induced by physiological processes not directly associated with neural activity [57]. Sources of physiological noise include cardiac and respiratory pulsations, respiratory-related susceptibility changes, low-frequency variations in HR and respiration depth/rate, as well as spontaneous fluctuations in blood pressure, vascular tone, oxygen consumption, and arterial CO₂ concentration [173]. This thesis focuses on cardiorespiratory processes, in particular on HR variations, since they are the primary sources of physiological noise [23]. Figure 2.6 summarizes the main sources of noise affecting the BOLD signal, including those of non-physiological origin, which are out of the scope of this study.

Physiological noise due to cardiorespiratory processes can be characterized in two categories [256, 57]. The first type is quasi-periodic, time-locked to the cardiac or respiratory cycles, and therefore referred to as cyclic physiological noise. The second type involves non-periodic low-frequency fluctuations that lie in the same frequency range as spontaneous neural activity (<0.1 Hz) [221, 135, 53, 26]. Importantly, this type of noise results from changes in CBF and CBV, which are also responsible for the BOLD contrast. Hence, it is usually called BOLD-like physiological noise [57]. Sources of BOLD-like noise are variations in HR and respiration depth/rate, which alter CBF and CBV through modulation of arterial CO₂ and blood

pressure [57, 26]. Sources of cyclic physiological noise, as well as HR and respiratory variations, are described in more detail in the following subsections.

The percentage of variance explained by all physiological noise sources is often comparable to that of spontaneous neural fluctuations at rest and the evoked BOLD response in task-based experiments [50]. In brain regions containing large arteries and draining veins or in regions close to the CSF, the physiological contribution to the BOLD signal is several times higher than its neural counterpart [22, 68]. Likewise, the extent of brain areas affected by physiological fluctuations is widely distributed across the brain [53, 221]. Physiological noise has a substantial impact on FC. Although there is an ongoing debate on how much of the physiological signal can be truly considered as “noise” [127, 171, 257], successful measurement of FC requires that all sources of physiological fluctuations are correctly addressed.

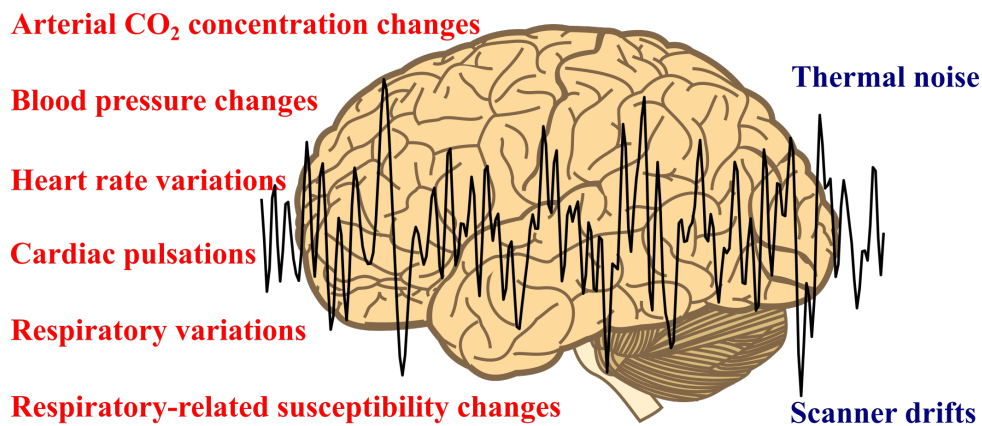


Figure 2.6: Main sources of noise affecting the BOLD signal. Sources of physiological origin are highlighted in red, while those of non-physiological origin are highlighted in blue.

2.4.1 Sources of cyclic respiratory noise

Respiration is the process of moving air into and out of the lungs to bring oxygen to the cells and flushing out carbon dioxide. The respiratory cycle may lead to involuntary head movements and magnetic field changes that distort the MR image of the brain [46, 121, 203]. The noise in the fMRI signal resulting from respiration is primarily observed in the phase of the acquired signal [255]. It has been hypothesized that the presence of noise in the signal phase results from variations in B_0 caused by movements of the chest wall and internal organs. These movements lead to susceptibility variations, which turn into different local Larmor frequencies in the brain [181]. For example, signal phase variations in the human brain at 3 T are caused by a respiration-induced B_0 modulation of about 0.01 parts-per-million (i.e. 1.25 Hz) produced by the movement of organs in the chest [119, 255]. Also, the signal magnitude is affected

2.4 Impact of physiological noise on the BOLD signal

during respiration. The seminal study by Bates *et al.* [15] showed that the signal intensity might change up to 60% of the baseline level when subjects are administered pure oxygen. Due to its paramagnetic properties, oxygen distorts the local magnetic field, causing changes in the fMRI signal.

Another major contribution of respiration to signal fluctuations is due to head movements [121]. Small movements of the head due to breathing are responsible for introducing “spin history” artifacts [91], a complex phenomenon that arises due to accumulated spin excitations between successive MRI scans. For example, if the head suddenly moves during the scan, the current slice being acquired might correspond to a different part of the brain than it did the scan before. This means that the slice will be in a different state of excitation, and therefore the signal intensity will also be different. Also, head movements affect the image phase information [112, 111, 121]. Cyclic respiratory-related head movements lead to scan-to-scan variations in local and global tissue susceptibility, which can be especially pronounced close to air cavities. Overall, the effects of the respiratory cycle on the BOLD signal are mainly observed near CSF areas [252], large veins [43], and boundaries between different brain tissues [30], as shown in Figure 2.7A.

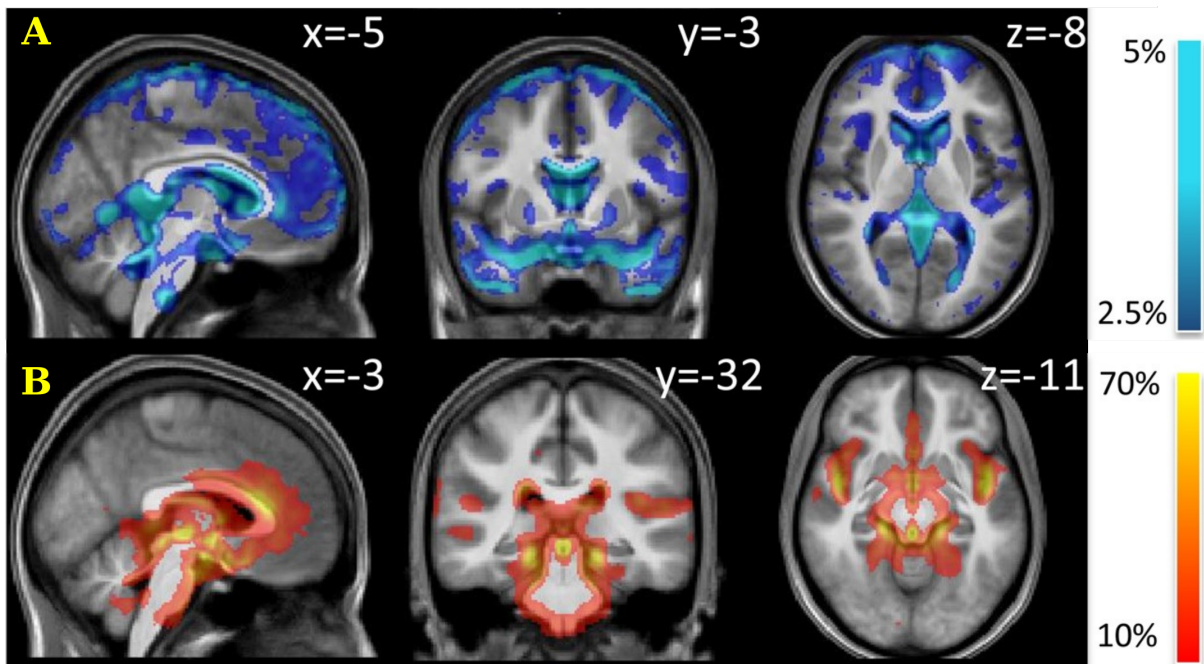


Figure 2.7: Brain areas affected by cyclic respiratory and cardiac noise as modeled by the RETROICOR regressors (2.5.1; adapted from Kasper *et al.* [134]). **A)** The brain areas affected by cyclic respiratory noise include primarily peripheral CSF areas and boundaries between brain tissues, while those affected by cyclic cardiac noise (**B)** are mainly localized in large draining vessels and within neighboring regions of CSF-filled areas. The colorbar indicates the percentage of the signal variance explained by the regressors.

2.4.2 Sources of cyclic cardiac noise

The cardiac cycle is another important source of physiological noise. To understand how it affects the BOLD signal, it is necessary to describe the sequence of events that occur when the heart beats. The cardiac cycle is initiated by the cardiac pacemaker, the sinoatrial node, and consists of two periods, the ventricular contraction (systole) and the ventricular relaxation (diastole). Diastole begins with the closing of the aortic valve and ends with the closing of the mitral valve. During diastole, heart ventricles relax, and the heart fills with blood. Subsequently, systole begins when the mitral valve closes and ends with the closure of the aortic valve. This stage is characterized by ventricular contraction, forcing blood into the arteries. During systole, blood pressure reaches a peak due to the ejected blood caused by the contraction of the left ventricle [260]. Vessel pulsation, CSF movement, and tissue deformation are all associated with the cardiac cycle, which can produce fMRI signal variance [68].

The regular blood-pumping into the vascular system by the heart has a strong impact on the BOLD signal. For example, pulsatile effects of large vessels induce signal fluctuations in areas adjacent to the vessels (see Figure 2.7B), both by causing tissue movement and by producing an influx of unsaturated blood into the slice of interest, which causes spin-history effects [91]. The cardiac cycle leads to uniform bulk motion of large brain regions during systole, such as the diencephalon or the brainstem, which slowly return to their initial configuration during diastole [45, 83, 116]. The fact that the skull constrains the brain volume implies that during each heartbeat, the influx of blood results in a dynamic interaction between the competing space requirements of three main components: brain tissue, blood volume, and CSF [106]. More specifically, the brain vasculature experiences an intense pressure during the systolic phase, which translates into an intracranial pressure wave that moves quickly along the cerebral arterial tree, causing a re-ordering of the cerebral tissue [83, 106]. Arterial expansions are first observed in the frontal lobe and subsequently in the more posterior parts of the brain and exert pressure on the cerebral tissue leading to an inward expansion of the brain during the systolic phase [68]. Such brain motions are responsible for venting CSF into the spinal canal to make room in the cranial cavity for the influx of new blood. Brain tissue movements occur at relatively high velocities during systole, ranging between 0-2 mm/s. The highest velocities are found in the basal ganglia (1.0 mm/s) and brainstem (1.5 mm/s) [83, 106], with peak displacements of about 0.15 mm and 0.2 mm, respectively [78]. Tissue motion related to the cardiac cycle causes BOLD signal variation that undermines the ability to detect hemodynamic changes related to neural activity using fMRI, in particular, for experiments conducted at sub-millimeter resolution [136, 198].

The cardiac cycle also affects the BOLD signal through aliasing (see section 2.6). For example, in standard fMRI studies with low temporal resolution ($2\text{ s} < \text{TR} < 3\text{ s}$), the fundamental respiratory and cardiac frequencies alias back into the lower resting-state frequency range (0.01-

0.1 Hz) [31]. As a result, the BOLD time-series of anatomically separated brain regions may have a similar shape leading to spurious correlations between these regions [22, 31, 64].

2.4.3 Respiratory variations

Respiratory variations are also known to cause widespread BOLD signal fluctuations. Subtle variations in breathing depth and rate induce signal changes through direct modulation of CBF and CBV, which is believed to occur due to alterations in arterial CO₂ levels [26, 253]. Since CO₂ is a potent vasodilator, variations in arterial CO₂ cause blood flow changes that result in signal fluctuations [26, 253]. The interaction between CO₂ variations caused by respiratory processes and BOLD signal fluctuations is part of a complex feedback circuit via chemoreflexes that seeks to maintain optimal blood gas parameters during respiration [1, 114]. Changes in the concentration of arterial CO₂ trigger the activation of central and peripheral chemoreceptors, altering the breathing depth and rate [246]. For instance, an increase in arterial CO₂ activates chemoreceptors that result in increased CO₂ exhalation and, therefore, a reduction of arterial CO₂.

At rest, changes in arterial CO₂ tension can be represented by changes in the end-tidal partial pressure of carbon dioxide (PETCO₂) [98, 206, 253], assuming that arterial blood gases and lung gases are equilibrated [192]. Even without external modifications, PETCO₂ fluctuates over the natural breathing and cardiac cycle through the respiratory sinus arrhythmia mechanism (RSA) [223]. RSA is a naturally occurring variation in HR during a breathing cycle driven by the parasympathetic (vagal) nervous system, in which HR increases during inspiration due to vagal withdrawal, while upon expiration, the vagal tone increases, causing a decrease in HR [95]. PETCO₂ signal, in contrast to arterial CO₂, can be easily derived from external recording devices. In humans, arterial CO₂ fluctuations at rest, as measured by PETCO₂, have been observed mainly in the 0-0.05 Hz range and constitute an important source of low-frequency fluctuations in the BOLD signal [253].

2.4.4 Heart rate variations

Similar to respiratory variations, non-periodic low-frequency HR fluctuations are another significant source of BOLD-like signal changes [53, 68, 221]. Nonetheless, the mechanisms by which HR fluctuations translate into BOLD signal fluctuations are less understood than those related to respiratory processes [57]. Variations in HR are a product of different interacting physiological processes, including respiration and respiration-related arterial pressure changes, vigilance and arousal states, sympathetic and parasympathetic nervous activity, and hormones [71, 3, 62, 187].

Thus, it is challenging to separate HR-induced fluctuations from other contributions to the BOLD signal.

Despite this complexity, multiple lines of evidence suggest that HR variations are mainly mapped into the BOLD signal through modulation of the blood pressure [135, 3]. As mentioned earlier, blood pressure changes cause deviations in CBF and CBV, thereby inducing BOLD-like signal fluctuations. Blood pressure changes occurring at 0.1 Hz, also known as Mayer waves [165], are closely related to HR variations [133]. The link between HR and blood pressure is reinforced by the fact that most of the variance in the mean arterial pressure time series can be explained through low-frequency HR fluctuations. Physiologically, this close relationship is attributed to the baroreflex-mediated autonomic regulation of the sinoatrial node that modulates HR in response to changing pressure [139, 214]. Mayer waves can also be independent of HR and cause BOLD signal fluctuations. While the nature of these waves remains unclear, earlier studies suggest that they have a neural origin, as shown by their close relationship to states of sympathetic activation [165, 94, 174]. Also, blood pressure changes can occur at other frequencies than Mayer waves due to spontaneous fluctuations in vascular caliber [93] and circadian rhythm [167].

Variations in HR are a major concern for fMRI studies, particularly for those conducted at rest since HR changes occur at the same frequencies as slow spontaneous neural fluctuations [135]. In the resting-state, HR variations correlate with the BOLD signal throughout the gray matter [53, 221]. This global correlation is thought to be mediated by changes in vigilance and arousal state, which trigger changes in HR and global neural activity simultaneously [57]. Task-based fMRI can also be affected by HR variations, as may happen in response to emotional stimuli or tasks modulating levels of arousal. In those cases, the HR-induced signal changes may be misinterpreted as reflecting task-related neural activation [28].

It is noteworthy to mention that while the respiratory-induced BOLD signal fluctuations are widely accepted as noise, the HR-induced changes are still a matter of debate [127, 171, 257]. Since the autonomic nervous system constantly regulates HR, by removing the signal variance explained by HR, one may also remove meaningful physiological information [237, 238]. Besides, as the brain also receives input from the internal body, ascending HR signals may play an essential role in shaping resting-state brain dynamics as well as influencing behavioral and emotional responses [7].

2.5 Physiological noise correction methods

Physiological noise can significantly confound estimates of functional connectivity or task activation in BOLD fMRI data. A good starting point for separating sources of noise is to identify spatiotemporal characteristics of the noise in the scanned data. For example, functions describing instrumental drifts are often polynomial functions, whereas functions describing physiological contributions tend to be periodic. Thus, a small order polynomial regression model may be sufficient to remove drift artifacts, while Fourier series are generally employed to remove cyclic physiological noise. Additionally, cardiac and respiratory fluctuations affect different vessel systems [50]. BOLD signal fluctuations at the frequency of the cardiac cycle occur primarily in the arterial vascular system and reflect the propagation of the arterial pressure wave to the peripheral arteries [252]. In contrast, respiratory-related signal changes occur mainly in the venous vascular system due to differences in cerebral venous blood oxygenation during in- and expiration [252].

In the past, several techniques have been developed to filter out these unwanted physiologically induced fluctuations in the BOLD signal, including data-driven approaches and models based on external physiological recordings. Data-driven approaches, such as independent component analysis [19, 126], distinguish components related to the physiologic noise from those related to the neural signal. A major disadvantage of these methods is that the distinction between neural and noise components depends on user-defined algorithmic parameters, such as the number of components and data dimensionality. Denoising methods based on external physiological recordings have recently become more popular as modern MR scanners are equipped with compatible physiological monitoring systems. Touch-free alternatives for physiological recordings using magnetic detection with nuclear MR (NMR) field probes have started to gain attention, particularly for 7 T scanners [73]. The NMR field probes measure small changes in the magnetic field caused by respiratory and cardiac action to produce physiological regressors [108, 250]. However, as the MRI experiments described in this thesis were performed using touch devices for physiological recordings, from now on, only noise correction methods for this technique will be discussed.

One of the most straightforward correction techniques is to remove parts of the fluctuations caused by breathing by regressing the respiration volume per time (RVT). The RVT signal can be considered a good approximation of variations in arterial CO₂, induced by changes in breathing depth and rate [26]. Other popular model-based techniques allow retrospective correction of cyclic artifacts in k -space (RETROKCOR) [122] or image domain (RETROICOR) [97], being the latter the most used in practice [50]. Other correction approaches model the effect of physiological processes on the BOLD signal by using the response function that mediates their

coupling [26, 53, 64, 81, 98]. Response functions, contrary to retrospective models, provide nuisance regressors that account for BOLD-like noise caused by HR or respiratory variations. Figure 2.8 illustrates the most common physiological noise correction methods based on external recordings.

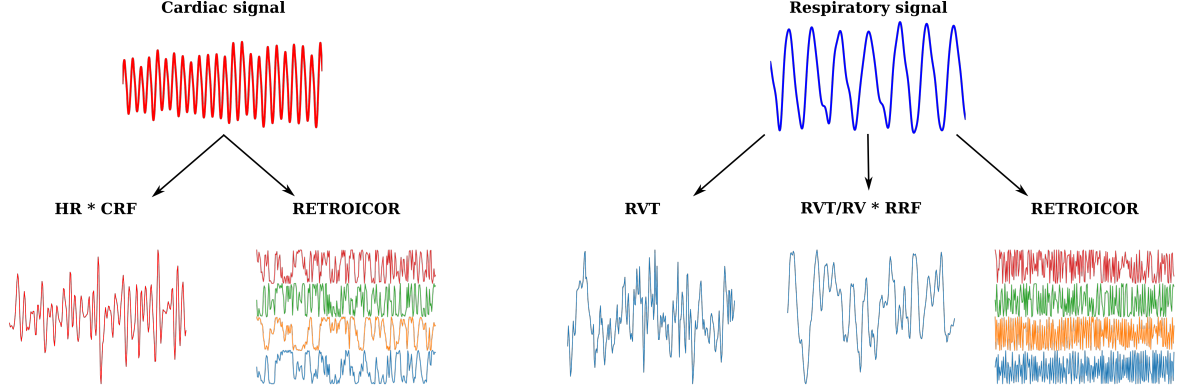


Figure 2.8: Schematic illustration of popular physiological noise correction methods based on external recordings. HR*CRF refers to the regressor formed by convolving the HR signal with the cardiac response function (CRF). Similarly, RVT/RV*RRF represents the regressor formed by convolving the RVT or RV signal with the respiratory response function (RRF; see text).

A description of these methods, as well as their advantages and disadvantages, is given in the following subsections.

2.5.1 RETROspective Image CORrection (RETROICOR)

Assuming that cardiac and respiratory fluctuations can be modeled as quasi-periodic signals, RETROICOR models them using a Fourier series defined by the relative phases of the cardiac and respiratory cycles at the time of image acquisition [97]. Formally, RETROICOR can be written as [116]:

$$y(t) = \sum_{A=1}^{N_A} \left(\beta_{1A} \cos(A\varphi_c(t)) + \beta_{2A} \sin(A\varphi_c(t)) \right) + \sum_{B=1}^{N_B} \left(\beta_{3B} \cos(B\varphi_r(t)) + \beta_{4B} \sin(B\varphi_r(t)) \right) + \sum_{m=1}^{N_m} \Psi_m$$

with Ψ_m as defined in [134]:

$$\begin{aligned} \Psi_m = & \beta_{5m} \cos(m\varphi_c(t)) \cdot \cos(m\varphi_r(t)) \\ & + \beta_{6m} \sin(m\varphi_c(t)) \cdot \cos(m\varphi_r(t)) \\ & + \beta_{7m} \cos(m\varphi_c(t)) \cdot \sin(m\varphi_r(t)) \\ & + \beta_{8m} \sin(m\varphi_c(t)) \cdot \sin(m\varphi_r(t)) \end{aligned}$$

(2.10)

N_A , N_B and N_m are the orders of the expansion, β 's are unknown amplitude coefficients, and $\varphi_c(t)$ and $\varphi_r(t)$ are the phases in the respective cardiac and respiratory cycles at time t . The multiplicative Fourier terms Ψ_m account for interaction effects between cardiac and respiratory cycles and can be chosen with a different order $N_m \leq N_A$ or N_B [116, 44]. The phases of the cardiac and respiratory cycles, φ_c and φ_r , are estimated, respectively, using peak-detection and histogram based methods from external physiological recordings [134]:

$$\varphi_c(t) = 2\pi \frac{t - t_n}{t_{n+1} - t_n}, \quad \varphi_r(t) = \pm \pi \frac{\int_{R_{min}}^{R(t)} H(R) dR}{\int_{R_{min}}^{R_{max}} H(R) dR}, \quad (2.11)$$

where t_n is the time of the cardiac peak preceding t , and t_{n+1} is the time for the subsequent cardiac peak. $R(t)$ is the current amplitude of the respiratory signal, R_{min} and R_{max} are, respectively, the minimum and maximum amplitude values of the respiratory signal, and H is the histogram capturing the frequency of each respiratory amplitude throughout the fMRI time series.

The Fourier expansion is generally performed using two harmonics of each physiological factor, i.e. $N_A = 2$, $N_B = 2$ and $N_m = 0$ [97]. However, in brain areas highly contaminated by physiological noise such as the brainstem, higher-order models that include multiplicative Fourier terms are preferred over low-order models, e.g. $N_A = 3$, $N_B = 4$ and $N_m = 1$ [116]. Multiplicative Fourier terms are used to account for complex physiological processes like the respiratory sinus arrhythmia effect. Nevertheless, increasing the number of regressors using higher-order models and multiplicative Fourier terms may result in a loss of degrees of freedom and leads to overfitting of the fMRI data, i.e. reducing statistical power and removing fluctuations unrelated to physiologic noise [17].

RETROICOR, in contrast to retrospective correction in k -space (RETROKCOR), operates in the image space and treats each voxel separately. By doing the correction in the image space, it overcomes the drawbacks of fitting the Fourier terms to complex raw data and considerably reduces the computational burden for data acquired with multichannel coils. Another major advantage of RETROICOR is that it does not introduce artificial coupling of noise corrections across spatial regions, a problem generally found during corrections in k -space [97].

Nevertheless, estimating the RETROICOR regressors requires certain mathematical assumptions, considered as deficiencies of the model. For example, the coefficients of the Fourier terms are assumed to be constant in time, implying that the amplitude of the fluctuations is also constant in time. This assumption is somewhat unrealistic because real signals show aperiodicity due to small variations in amplitude and phase [211]. All these limitations can be overcome at the expense of increasing the complexity of the RETROICOR model by representing the Fourier

series in terms of differential equations (oscillators) with time-varying frequencies and adding a white noise component to account for the small changes in the shape of the signal [211].

Another drawback of the RETROICOR technique is that the estimation of the cardiac phase associated with the imaged slice is not calculated correctly. The RETROICOR algorithm assumes that the cardiac cycle follows the same inherent pattern regardless of the inter-beat time interval, i.e. equal contraction of all parts during the cardiac cycle. However, this assumption is not entirely accurate as there are differences in the time interval between beats that are rather associated with time variations in the diastolic portion than the systolic phase [68]. However, the failure to remove the naturally occurring slower signal changes due to breath-to-breath variations in depth/rate is the most important limitation of RETROICOR [26]. As mentioned earlier, these subtle changes in respiration cause fluctuations in arterial CO₂ that overlap with resting-state neural activity, representing a significant source of BOLD-like physiological noise [26].

2.5.2 Respiration Volume per Time (RVT)

Low-frequency BOLD fluctuations related to variations in respiratory rates can be reduced by regression of time series generated from external respiratory recordings. One of these regressors is called respiration volume per time (RVT), and contrary to RETROICOR, it attempts to capture the changes in respiration depth and rate that cause periodic fluctuations in arterial CO₂ concentration [26].

RVT is calculated from the envelopes generated by the maxima and minima of the respiratory belt positions at the peaks of inspiration and expiration, respectively [26]. Specifically, the difference between successive maxima and minima envelopes is divided by the duration of the respiration, i.e. the time between peaks of inspiration and expiration (Figure 2.9). It has been shown that for optimal removal of respiratory-related BOLD fluctuations, the RVT plus copies of the RVT signal delayed in time are better for physiological noise correction than the RVT alone [29, 131]. Additionally, RVT can be convolved with the respiration response function (RRF, see 2.5.3), resulting in improved physiological noise correction [29]. Another regressor that models low-frequency respiratory-related fluctuations is the so-called respiratory volume (RV) [53]. RV is computed as the standard deviation of the respiratory waveform on a sliding window, of usually 6 s, centered at each TR sampling point (Figure 2.9). RV offers some advantages in comparison to RVT. For example, it does not rely on the accuracy of detecting respiration peaks and minima as required by RVT. RV is a simple sliding-window measure related to the inspired volume over time, whereas RVT accounts more explicitly for variations in breathing rate by normalizing the depth by the duration of the respiration.

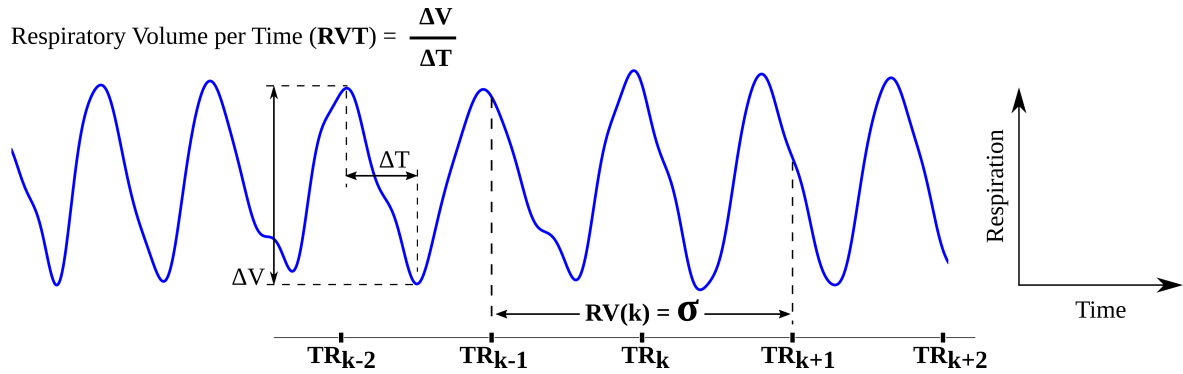


Figure 2.9: Illustration of the definition of respiration volume per time (RVT) and respiratory volume (RV). The symbol σ denotes the standard deviation of the given window.

The RVT method has limitations that need to be considered. For instance, to account for the complex interplay between respiratory fluctuations and the BOLD signal, several time-shifted copies of the RVT time series are regressed out from the fMRI data. The number of RVT copies depends on the number of maxima and minima in the cross-correlation function between RVT and fMRI time series [26]. If the cross-correlation function exhibits multiple maxima and minima, then various shifted RVT waveforms need to be incorporated into the regression model, which may lead to overfitting of the fMRI data.

One way to simultaneously overcome the aforementioned problems associated with the RVT and RETROICOR methods is to convolve the RVT/RV and HR regressors with a respiratory response function (RRF) [29] and a cardiac response function (CRF) [53], respectively. Overall, these response functions help to capture the complex dynamic interaction occurring at low-frequencies between the physiological processes and the BOLD signal while reducing the risk of overfitting.

2.5.3 Response functions

The estimation of the response function that mediates the coupling between physiological factors and the resulting BOLD signal is another alternative for noise correction [29, 53]. Physiological response functions aim to account for BOLD-like noise contributions. As shown previously, the regressor formed by the convolution of the physiological signal (HR, RVT, or RV) with the corresponding response function reduces more variance than the physiological signal alone [29, 53]. A linear model relating physiological and BOLD signals is generally assumed to derive physiological response functions. This approach is similar to that used for modeling the hemodynamic response function (HRF) to task activation, which gives accurate estimates of the HRF [102, 90, 51].

The RVHR model introduced by Chang *et al.* [53] is the most widely used in the analysis of BOLD data. In this model, the time series of a voxel (y) is modeled as the sum of RV convolved with an unknown RV filter (h_r), i.e. the respiratory response function, and HR convolved with an unknown HR filter (h_h), i.e. the cardiac response function, plus a noise term (ε). Golestani *et al.* [98] extended the RVHR model in order to derive the PETCO₂ response function and enable modeling of PETCO₂-related signal fluctuations. The following expression 2.12 corresponds to the original RVHR model of Chang *et al.* [53] but can be easily extended to more physiological factors.

$$y = Xh + \varepsilon, \tag{2.12}$$

with: $X = [X_r, X_h]$ and $h = [h_r, h_h]^T$

X_r and X_h are the convolution matrices of RV and HR, respectively, which have a Toeplitz structure, i.e. its entries are constant along all descending diagonals from left to right [104], and ε represents random noise with variance σ_ε^2 assumed to be equal to the variance of y .

In Equation 2.12, the number of parameters describing the shape of the response functions depends on the duration of the filters and the temporal resolution, i.e. TR. For example, for TR = 2.5 s and filter duration = 30 s, Equation 2.12 turns into a problem with 24 parameters (12 per filter). As the number of parameters increases, the model will be more prone to overfitting or parameters become ill-determined, which can lead to no physiologically plausible response functions [102]. One way to address these issues is to place a prior on the filter parameters to "regularize" the solutions [193, 102, 254]. This approach was pioneered by Goutte *et al.* [102], who placed a Gaussian prior on the HRF parameters, forcing the HRF to be smooth. In that work, the authors also tested several priors, including Gamma, Poisson, and Gaussian, and showed that the latter captured the features of the HRF more accurately, e.g. the post-stimulus undershoot.

In the RVHR model, a Gaussian prior ($h \sim N(0, K)$) is also placed on h , where K is a block-diagonal matrix of the form:

$$K = \begin{bmatrix} K_r & 0 \\ 0 & K_h \end{bmatrix}$$

K_r and K_h are covariance matrices describing the degree of correlation between points in h_r and h_h as a function of their distance and are defined as: $[K_r]_{ij} = [K_h]_{ij} = \sigma_f^2 \exp(-(i-j)^2/2l^2)$ where the length scale l governs the degree of smoothness imposed on the filters and the kernel variance σ_f^2 regulates the distance from which filter values depart from its mean. The quantities σ_ε^2 , σ_f^2 , and l , known as hyperparameters, are usually set beforehand, and their choice has a significant impact on the shape of the filters.

Similar to the HRF, filters are constrained to begin and end at 0, which guarantees that given sudden fluctuations in either RV or HR, the response will have a finite rise time and posteriorly decays to baseline. Estimation of h with its imposed constraints can be achieved using Bayesian and optimization theory. The interested reader can find more detailed information in Goutte *et al.* [102] and Nocedal *et al.* [180]. In Bayesian linear regression, Equation 2.12 is reformulated using probability distributions: $y \sim N(Xh, \sigma_\epsilon^2 I)$ where I is the identity matrix. The goal here is to find the optimal h , also known as *maximum a posteriori* estimate, that maximizes the *posterior distribution* $p(h|y)$, i.e the probability of h given the data. According to Bayes' theorem, $p(h|y)$ is given by:

$$p(h|y) = \frac{p(y|h)p(h)}{p(y)}, \quad (2.13)$$

where $p(y|h) \propto \exp\left(-\frac{1}{2\sigma_\epsilon^2}(y - Xh)^T(y - Xh)\right)$ is the conditional distribution or *likelihood function* and indicates how likely the data are to appear for each possible value h . The proportional sign \propto is used to omit unnecessary factors. The term $p(h) \propto \exp(-\frac{1}{2}h^T K^{-1}h)$ is the *prior distribution* (what is known about h before observing the data). The term in the numerator $p(y)$ is called the *marginal likelihood* or probability of y and is independent of h , and therefore not necessary for estimating h . Thus, Equation 2.13 can be rewritten as: $p(h|y) \propto p(y|h)p(h)$. Since maximizing $p(h|y)$ is equivalent to minimizing $-\log(p(h|y))$, the problem reduces to:

$$-\log(p(h|y)) \propto \frac{1}{\sigma_\epsilon^2}(y - Xh)^T(y - Xh) + h^T K^{-1}h \quad (2.14)$$

Using now optimization theory to take into account the constraints imposed on h , Equation 2.14 transforms to a quadratic problem (QP) of the form:

$$\begin{aligned} & \text{minimize} && \frac{1}{2}h^T Gh + h^T c \\ & \text{subject to} && Sh = 0 \end{aligned} \quad (2.15)$$

$$\text{with: } G = 2\left(\frac{X^T X}{\sigma_\epsilon^2} + K^{-1}\right) \quad \text{and} \quad c = \frac{2}{\sigma_\epsilon^2} X^T y$$

S is a sparse matrix of dimension $[4, (n_r + n_h)]$ used to specify that filters begin and end at 0. The quantities n_r and n_h denote the number of points (TRs) used to determine h_r and h_h , respectively. S is completely filled with zeros except at the positions $(1, 1)$, $(2, n_r)$, $(3, n_r + 1)$ and $(4, n_r + n_h)$.

To solve Equation 2.15, we make use of the Karush-Kuhn-Tucker (KKT) conditions or first-order necessary conditions (see Nocedal *et al.* [180] for more details). The KKT conditions

are used to determine a local optimum point in a constrained nonlinear program and reformulate a QP into a complementary system of linear equations. For example, the KKT conditions for h^* to be a solution of Equation 2.15 state that there is a vector λ^* , also known as Lagrange multiplier, such that the following system of equations is satisfied [180]:

$$\begin{bmatrix} G & S^T \\ S & 0 \end{bmatrix} \begin{bmatrix} h^* \\ \lambda^* \end{bmatrix} = \begin{bmatrix} c \\ 0 \end{bmatrix} \quad (2.16)$$

Based on this model, Chang and colleagues proposed an analytic function for h_h (Figure 2.10), commonly referred in the literature to as "canonical CRF", and parameterized as follow [53]:

$$CRF(t) = 0.6t^{2.7}e^{-t/1.6} - \frac{16}{3\sqrt{2\pi}}e^{-\frac{(t-12)^2}{18}} \quad (2.17)$$

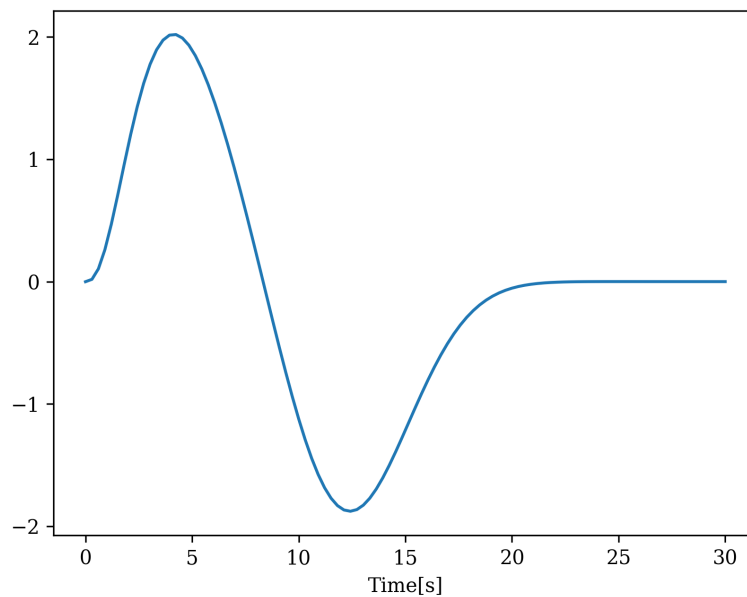


Figure 2.10: Canonical cardiac response function (CRF) proposed by Chang *et al.* [53] to model low-frequency heart rate fluctuations in the BOLD signal.

The canonical CRF has been used in several studies applying physiological noise correction (see for example [42, 56, 140, 251]) and has become the default CRF in popular software for fMRI processing, such as the PhysIO toolbox [134] and the PhLEM toolbox [251]. However, it should be stated that this analytic CRF(t) was derived from a sample that included only three subjects. Therefore, it is very likely that the CRF(t) does not properly model cardiac-related signal changes in a large population with different physiological responses.

2.6 Aliasing effects

In signal processing, the term aliasing refers to the signal distortion that occurs when high-frequency components are mapped into low-frequency components. The unique criterion that needs to be satisfied for aliasing to occur is that the sampled signal contains frequencies higher than half the sampling rate, also known as the Nyquist frequency. Aliasing of physiological signals is an issue commonly found in BOLD data. In particular, the cardiac signal is the most problematic due to the frequency at which it occurs (0.8-1.5 Hz [227]). In BOLD data, aliasing causes time series of distant regions to have a similar shape, thus introducing spurious correlations [155]. Standard processing strategies like temporal filtering do not work when aliasing occurs because aliased frequencies are likely to overlap with frequencies of the signals of interest. Although state-of-the-art accelerated fMRI acquisitions allow high sampling rates with a corresponding millisecond-level temporal resolution, they are still lower than the Nyquist sampling rate required for the fundamental cardiac frequency [84, 143, 183]. For example, the TR used at the Human Connectome Project is 720 ms [247], which means that only fundamental cardiac frequencies below 0.7 Hz can be sampled without aliasing.

3 Materials and Methods

3.1 Data acquisition and preprocessing

3.1.1 Subjects

Eighty-four healthy subjects (43 females, 41 males, average age: 31.58 ± 10.76 years, age range: 20-61 years) were studied using rs-fMRI data and simultaneously acquired physiological recordings. Subjects were selected from a large sample of 142 subjects, recruited from the local university community. Selection criteria were: mean HR during the rs-fMRI scan, quality of rs-fMRI and physiological data, gender, and age. Subjects were also asked to indicate the frequency of physical activities per week, which was scaled from 0 to 4 for statistical purposes, where 0 = no exercise, 1 = 1-2 times per week, 2 = 3-4 times per week, 3 = 5-6 times per week and 4 = more than 6 times per week. The rs-fMRI quality was assessed by visual inspection, looking for image artifacts such as geometric distortions and signal dropout, as well as by statistical quality control for inter-subject homogeneity as implemented in the CAT12 toolbox (<http://dbm.neuro.uni-jena.de/cat/>).

None of the participants had any present or past history of psychiatric, neurological, or other clinically significant disorders, as assessed by the short form of the structured diagnostic interview for DSM-IV (Diagnostic and Statistical Manual) psychiatric disorders Mini-International Neuropsychiatric Interview (MINI) [219] and by their stated medical history. According to the modified version of the Annett's handedness inventory [41], all participants were right-handed. Informed written consent was obtained in accordance with the protocol approved by the local Ethics Committee.

Heart rate groups

Three groups were formed (each comprising 28 subjects) based on the mean HR during the rs-fMRI scan and matched for age and gender. The first group was restricted to HR < 60 bpm (54.84 ± 5.34 bpm) and referred hereto as “Slow HR” (SHR). The second group was defined by the range $60 \text{ bpm} < \text{HR} < 75 \text{ bpm}$ (66.95 ± 3.52 bpm) and called “Medium HR” (MHR). Finally, a third “Fast HR” (FHR) group was defined with HR > 75 bpm (81.27 ± 7.64 bpm). Table 3.1 summarizes the demographic data for each of the three groups.

Table 3.1: Main demographic and physiological characteristics of the heart rate groups. Values are represented by mean \pm standard deviation.

Parameter	Slow HR	Medium HR	Fast HR	<i>p</i> -value [†]
Number of participants (n)	28	28	28	
Sex (m/f)	16/12	9/19	16/12	0.10 [‡]
Age [years]	31.14 ± 10.43	32.11 ± 10.83	31.50 ± 11.00	0.95
Self-rated Frequency of Physical Exercise	3-4 times/week(11 ^a)	1-2 times/week(27 ^a)	1-2 times/week(27 ^a)	0.85 [‡]
Heart rate [beats/minute]	54.84 ± 5.34	66.95 ± 3.52	81.27 ± 7.64	4.43×10^{-33}

[†] *p*-values from one-way ANOVA

[‡] *p*-values from χ^2 test

^a number of participants providing information

These three groups were used in sections 3.2 and 3.3, while in sections 3.4 and 3.6, the whole sample (84 subjects) was divided into two groups. In section 3.5, the whole sample was used without forming groups. All this is succinctly summarized in Table 3.2.

3.1.2 Physiological recordings and analyses

Cardiac and respiratory activity and skin conductance were recorded (500 Hz) during rs-fMRI data acquisition using an MR-compatible BIOPAC MP150 polygraph (BIOPAC Systems Inc., Goleta, CA, USA). Skin conductance (SC) was measured continuously (constant voltage technique) at the left hand’s palm with Ag/AgCl electrodes placed at the thenar and hypothenar eminence. Respiratory activity was assessed by a strain gauge transducer incorporated in a belt tied around the chest, approximately at the level of the processus xiphoideus. The cardiac signal, photoplethysmograph (PPG) signal, was recorded using a pulse oximeter attached to the proximal phalanx of the index finger of the subject’s left hand. The PPG, or pulse oximeter waveform, measures blood volume change in the microvascular bed of tissue by measuring the varying intensity of light traveling through the tissue [230]. The PPG can be used as a surrogate technique for the electrocardiogram (ECG) and is usually preferred to ECG systems for cardiac recordings since ECG-derived signals exhibit greater susceptibility to electromagnetic and biologic interference [24].

Table 3.2: Group arrangements in each section of this chapter.

# Groups	Heart rate range
<i>3.2 Analysis of heart rate and BOLD spectra</i>	
3	Slow, HR < 60 bpm
	Medium, 60 bpm < HR < 75 bpm
	Fast, HR > 75 bpm
<i>3.3 Analysis of cardiac response functions</i>	
3	Slow, HR < 60 bpm
	Medium, 60 bpm < HR < 75 bpm
	Fast, HR > 75 bpm
<i>3.4 Derivation of CRF from grey matter or cerebrospinal fluid</i>	
2	Slow, HR < 68 bpm (46)
	Fast, HR > 68 bpm (38)
<i>3.5 Noise correction on the default mode connectivity</i>	
1	All subjects (84)
<i>3.6 Analysis of the influence of CRF on the CAN connectivity</i>	
2	Slow, HR < 68 bpm (46)
	Fast, HR > 68 bpm (38)

Note: Values in parentheses are number of subjects. Details for estimating the HR value of 68 bpm are provided in [3.3.2](#) and [4.3.2](#).

PPG, respiratory, and SC signals were digitally filtered at 0.05-3 Hz, 0-10 Hz, and 0-10 Hz, respectively, to remove MRI-related or movement artifacts. The SC signal was also median filtered (window of 150 samples) and smoothed (over 250 samples) to remove spikes. Subsequently, cardiac and respiratory peaks were automatically detected using an in-house program written in Matlab (Mathworks, Natick, USA). An expert visually assessed the quality of detected peaks and corrected them when necessary. On average, less than 2% of peaks required correction. An interbeat-interval (IBI) time series was then defined as the peak-to-peak interval of the PPG signal. Heart rate variability (HRV) indices were estimated from the IBI time series according to established standard procedures [160, 109]. HRV indices included the root-mean-square of successive IBI differences (RMSSD), the ratio of low- to high-frequency components (LF/HF), and respiratory sinus arrhythmia (RSA). RMSSD and RSA are known to reflect parasympathetic activity, while LF/HF is considered a marker of sympatho-parasympathetic balance. Finally, the respiratory rate was calculated as the inverse of the interbreath interval of the respiratory signal and expressed in breaths/minute.

Changes in arousal may modulate neural activity in several brain areas and should be especially considered during the passive resting-state investigation [75, 191, 232]. Skin conductance changes are mainly dependent on the activity of sweat glands innervated by the sympathetic system and can be used to index sympathetic arousal [9]. Indices of sympathetic arousal [8, 37], mean SC level (SCL), and the number of spontaneous SC fluctuations (SCF), were computed

from the SC signal. SCL was estimated by averaging the signal, whereas SCF was identified by a pattern matching algorithm using the characteristic shape of an SCF described mathematically in [150]. Figure 3.1 summarizes the processing of physiological signals and calculated indices.

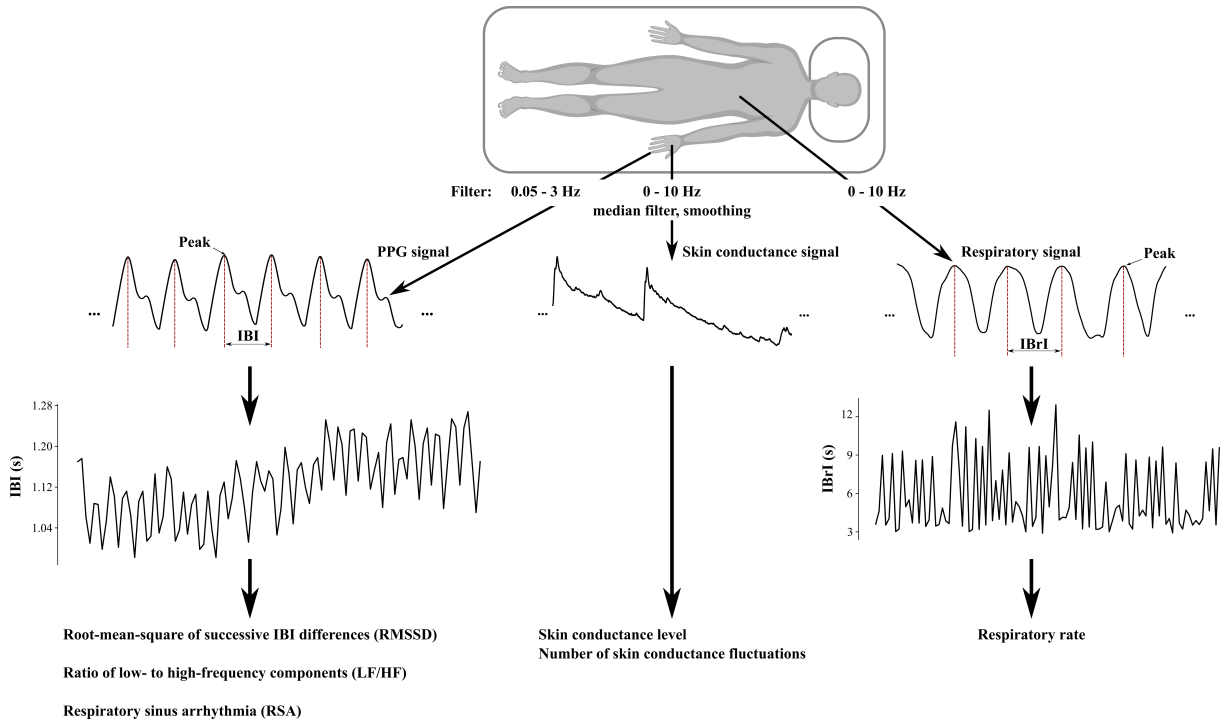


Figure 3.1: Illustration of the processing of physiological signals and the corresponding indices used in this study. The first step is the filtering of recorded signals to remove MRI-related or movement artifacts. The second step is the extraction of interbeat (IBI) and interbreath (IBrI) intervals time series from PPG (photoplethysmograph) and respiratory signals, respectively. Finally, the physiological indices from IBI, IBrI, and skin conductance signals are calculated.

3.1.3 MRI acquisition

MRI data were collected on a 3 T whole-body system equipped with a 12-element head matrix coil (MAGNETOM TIM Trio, Siemens). The measurement protocol consisted of a resting-state scan followed by a high-resolution anatomical scan. Participants were instructed to keep their eyes closed during the entire measurement and to move as little as possible. T_2^* -weighted images were obtained using a gradient-echo EPI sequence accelerated by parallel imaging using GRAPPA [107] ($TR = 2520$ ms, $TE = 30$ ms, flip angle (FA) = 90° , inter-slice gap = 0.625 mm, GRAPPA factor = 2) with 45 contiguous transverse slices of 2.5 mm thickness covering the entire brain and including the lower brainstem. The matrix size was 88×84 with an in-plane resolution of 2.5×2.5 mm² corresponding to a field of view (FOV) of 220 mm \times 210 mm. A series of 240 whole-brain volume sets was acquired in one session, lasting approximately 10 minutes.

High-resolution anatomical T_1 -weighted volume scans (MP-RAGE) were obtained in sagittal slice orientation (TR = 2300 ms, TE = 3.03 ms, inversion time = 900 ms, FA = 9° , FOV = 256 mm \times 256 mm, matrix size = 256 \times 256, number of sagittal slices = 192, GRAPPA factor = 2) with an isotropic resolution of 1 mm³.

3.1.4 MRI preprocessing

Preprocessing of resting-state fMRI data was performed using AFNI (<http://afni.nimh.nih.gov/>) and SPM12 (<http://www.fil.ion.ucl.ac.uk/spm>). The first five volumes were discarded, allowing magnetization to reach a steady state. Physiological noise correction was carried out by removing all respiratory-related fluctuations. The model included four regressors generated by the RETROICOR algorithm to reduce artifacts synchronized with the respiratory cycle [97] and five respiration volumes per time (RVT) regressors that model slow blood oxygenation level fluctuations [29]. The RVT regressors consisted of the RVT function and four delayed terms at 5, 10, 15, and 20 s. RETROICOR and RVT regressors were generated on a slice-wise basis by AFNI's RetroTS.m script [131], which takes the cardiac and respiratory time series synchronized with the fMRI acquisition as input. The cardiac signal was not included in the RETROICOR model to avoid altering the cardiac noise contribution in the fMRI signal.

Further preprocessing steps of fMRI data included slice-timing correction using Fourier interpolation, rigid-body realignment to the mean of all images, and spatial smoothing using a Gaussian kernel with full-width at half-maximum (FWHM) of 6 mm. Additional steps were removal of linear and quadratic trends and the six regressors estimated from rigid-body realignment. Due to the controversial interpretation of the functional connectivity results using global signal regression, this step was not included as part of the preprocessing of functional data [173]. Similarly, no passband-filtering was performed. Afterwards, a within-subject registration was conducted between functional and anatomical images using SPM12. Co-registered anatomical images are then used to generate a deformation field to warp any functional image into Montreal Neurological Institute (MNI) space [6].

3.1.5 HR regressor

The construction of the HR regressor was performed following the approach proposed by Chang *et al.* [53]. Briefly, the HR time series at k th TR was computed by averaging the time intervals between adjacent peaks contained in a window of $3TR$ defined by the $(k - 1)$ th, k th, and $(k + 1)$ th TRs interval, and converted to units of beats-per-minute. The HR regressor can be convolved with a cardiac hemodynamic response function (CRF) to model low-frequency

cardiac contributions in the BOLD signal. Figure 3.2 illustrates all steps for extracting the HR regressor.

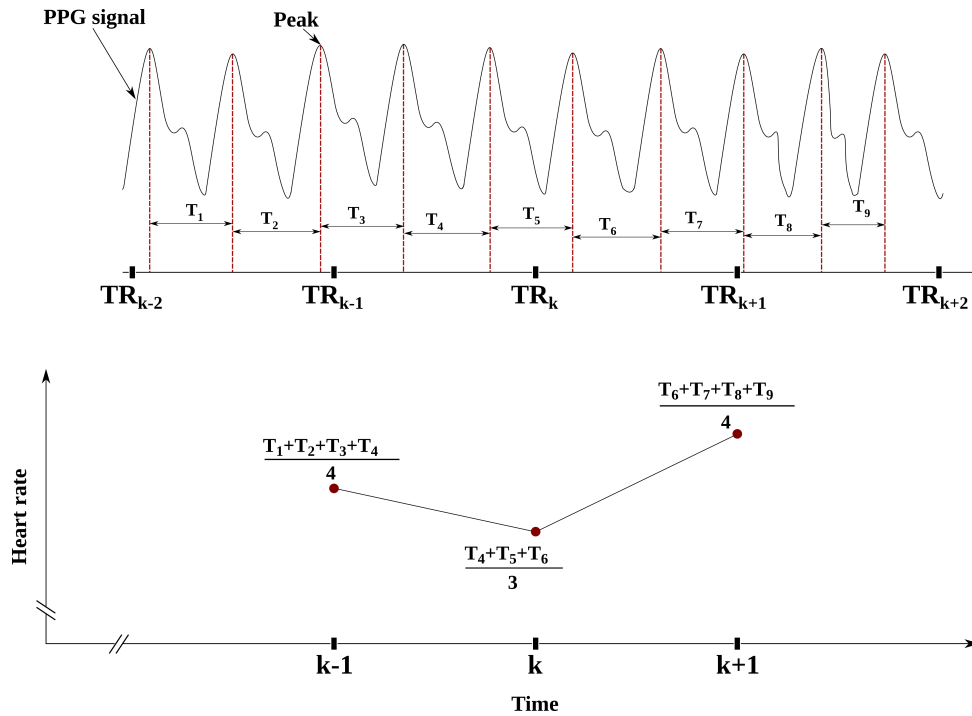


Figure 3.2: Illustration of the processing steps for the extraction of the HR regressor from the PPG signal (see 3.1.2). T_n represents the time interval between adjacent peaks in the PPG signal. The formation of the $HR(k)$ is performed by averaging all time intervals between adjacent peaks contained in the TR_{k-1} , TR_k , TR_{k+1} window.

3.2 Analysis of heart rate and BOLD spectra

To test the hypothesis of an association between frequency spectra of HR and BOLD signals, power spectral densities (PSDs) were estimated from HRV and whole-brain global (GS) signals. PSD is the frequency response of a random or periodic signal and informs about the distribution of average power as a function of frequency. The PSD was derived using the multitaper method [239], which is less sensitive to noise and non-stationarity than conventional Fourier analysis [169]. The rationale for using HRV is that HR and HRV are inversely related to each other [208, 170], i.e. higher HR corresponds to little HRV and vice versa. Besides, the frequency range of interest for resting-state BOLD signals largely overlaps with that of HRV, which facilitates the comparison of power spectra. The GS was calculated by averaging the time series over all voxels in the brain.

The HRV spectrum was estimated from the IBI time series. Importantly, the IBI time series is inherently unevenly sampled as the number of samples within each beat-to-beat interval

is different. This implies the necessity for resampling since the signal should have uniform sampling whenever the spectral analysis is applied using a transformed domain approach [118]. Hence, before PSD estimation, the IBI time series was resampled at 4 Hz [160] using cubic spline interpolation. The HRV spectrum was calculated from 0-0.5 Hz according to the guidelines in [160].

Each PSD was normalized by the total spectral power to allow meaningful comparisons between subjects with different overall levels of signal power. Subsequently, HRV and BOLD spectral powers were separately compared between groups using the Mann-Whitney U-test (see Table 3.1 for group descriptions). All tests were two-tailed, and the level of statistical significance was set at $p < 0.05$. Due to the multiple test situation in the between-group comparisons, a Bonferroni correction was applied in these tests. The spectral power was calculated as the area under the PSD curve in the frequency range of interest. HRV and BOLD spectral powers were derived within 0-0.2 Hz and 0.01-0.2 Hz, respectively. Frequencies below 0.01 Hz in the BOLD spectrum are primarily driven by scanner artifacts and ultra-slow metabolic oscillations [225] and, therefore, not relevant for fMRI. Finally, a linear regression analysis was conducted to examine the relationship between BOLD and HRV spectral powers in the <0.2 Hz frequency range. Figure 3.3 illustrates the processing steps described above.

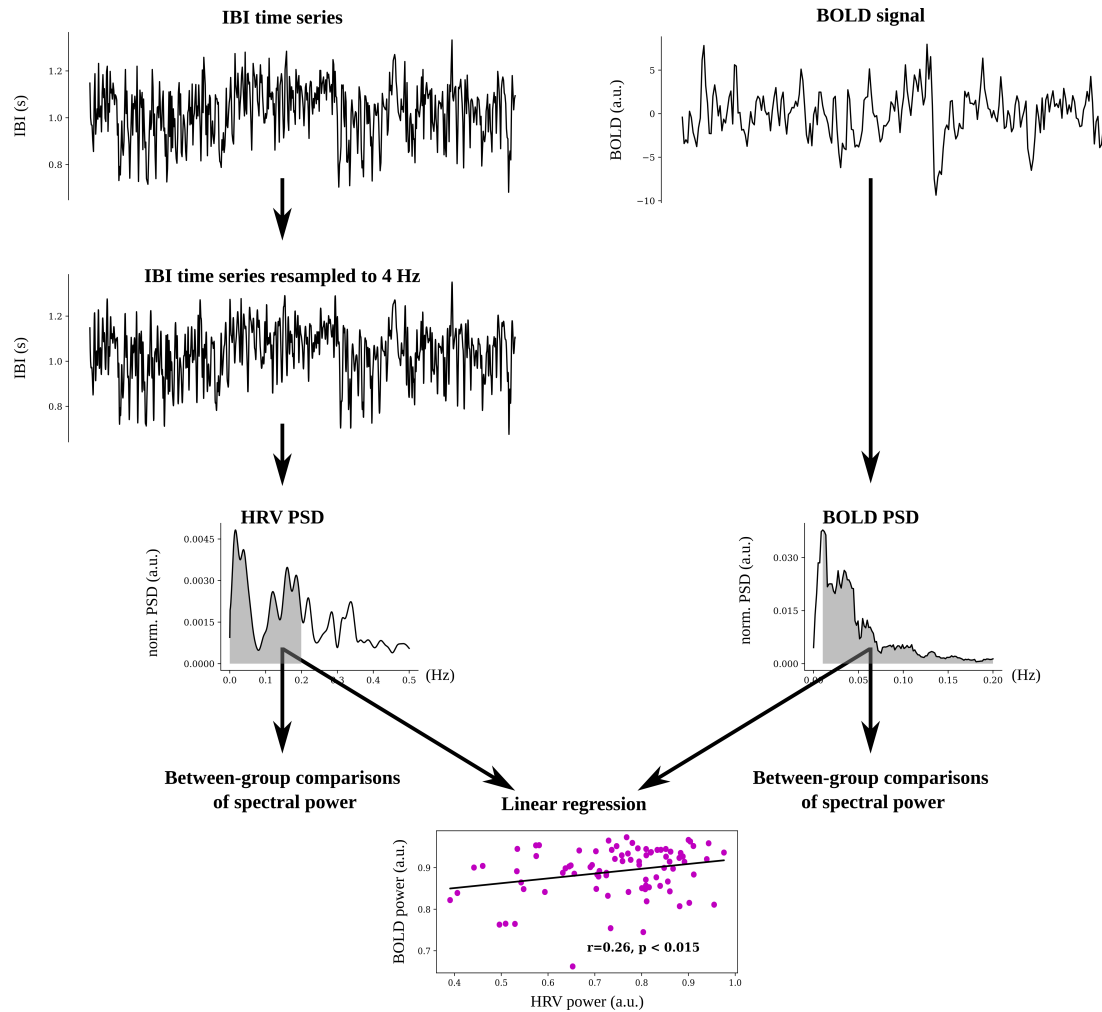


Figure 3.3: Illustration of the processing steps for analyzing HR and BOLD spectral powers. The IBI time series was resampled to 4 Hz before estimating the HRV power spectrum. HRV and BOLD spectral powers (area of the grey colored regions) were compared separately between groups and to each other via linear regression.

Abbreviations: IBI: interbeat-interval; HRV: heart rate variability; PSD: power spectral density; a.u.: arbitrary units.

3.3 Analysis of cardiac response functions

To address the inter-subject variability issue associated with the use of a canonical CRF, Falahpour *et al.* [81] suggested the deconvolution of individual respiratory and cardiac response functions from average brain tissue signals. In that work, individual response functions were deconvolved using the linear model in Equation 2.12 but with the GS as the reference BOLD signal. Although GS may contain some contribution of neural activity, GS is generally assumed to be dominated by physiological noise [58, 199], and therefore a good candidate for deriving physiological response functions [81].

Here, individual CRFs were also derived from the GS. Since CRF was the only response function of interest, the respiratory term in the linear model 2.12 was removed. The rationale is that most respiratory effects are minimized during physiological noise correction and potential interaction effects between cardiac and respiratory components, if present, are limited to a few voxels when fMRI data are acquired at 3T [17, 64]. Thus, the following model was used to derive the CRF:

$$y = Xh_h + \varepsilon \quad (3.1)$$

where X_h is the convolution matrix of the HR regressor and h_h the desired CRF. As it was previously shown in section 2.5.3, Equation 3.1 leads to a quadratic problem of the form:

$$\begin{aligned} &\text{minimize} && \frac{1}{2}h^T Gh + h^T c \\ &\text{subject to} && Sh = 0 \end{aligned} \quad (3.2)$$

where $G = 2\left(\frac{X^T X}{\sigma_\varepsilon^2} + K^{-1}\right)$ and $c = \frac{2}{\sigma_\varepsilon^2} X^T y$

This quadratic problem was solved assuming a Gaussian process for h_h , and a duration of 30 s, i.e. 12 scans at TR = 2.52 s. The hyperparameters l and σ_f^2 , representing the degree of smoothness and amplitude of the Gaussian process, were set to 2 and 1, respectively [53]. The hyperparameter σ_ε^2 was defined equal to the variance of GS, as done by Falahpour *et al.* [81]. The deconvolution of h_h was performed in Python using the *CVXOPT* package (cvxopt.org/). The derived CRF were averaged within each group in order to estimate a group-specific CRF (CRFg). Table 3.3 shows all CRFs that were generated or used through this study.

Table 3.3: Cardiac response functions generated or used through this study.

CRFc	Canonical CRF was estimated in an early study by Chang <i>et al.</i> [53] on physiological noise modeling using recordings from 3 subjects. The CRFc has been widely applied as standard approach for noise correction.
CRFi	Individual CRFs are estimated from individual data. Recent studies showed that CRFi vary considerably from subject to subject [81, 64].
CRFg	To assess the influence of different HRs on response functions, individual CRFs were estimated and averaged over subjects within each HR group (slow, medium, fast).
CRF_{HR}	To account for changes in individual CRFs depending on HR, HR-based CRFs are introduced in this thesis using an specific HR threshold (68 bpm) to distinguish between CRFs suitable for slow (<68 bpm) or fast HR (>68 bpm).

Note: Details for the HR cutoff at 68 bpm are provided in 3.3.2 and 4.3.2.

The coefficient of determination (R^2) was used to quantify the proportion of variance in the BOLD signal explained by the HR regressor convolved with three different methods: 1) the *canonical CRF* according to Chang *et al.* [53], 2) the *individual CRF* according to Falahpour *et al.* [81], and 3) the *group-specific CRF* (CRFg) proposed in the present study. R^2 is given by:

$$R^2 = \frac{\sum(\hat{y}_i - \bar{y})^2}{\sum(y_i - \bar{y})^2} \quad (3.3)$$

where y_i are the observed values, i.e. the BOLD signal, \hat{y}_i are the predicted values of y , and \bar{y} is the mean. The R^2 was calculated in each voxel in the subject's original space and multiplied by 100 to give a percentage value. These maps were transformed into MNI space by applying the deformation field obtained in 3.1.4. The significance of R^2 values was verified by determining the F -statistic:

$$F = \frac{R^2/k}{(1 - R^2)/(n - k - 1)} \quad (3.4)$$

where k is the number of independent variables (=1), n number of observations (=235). The F -statistic has an exact F -distribution with $(k, n - k - 1)$ degrees of freedom.

3.3.1 Evaluation of group-specific CRF

The estimated group-specific CRFs were evaluated according to several criteria.

Group-specific CRF across brain regions

As the CRF depends on the presence of low-frequency cardiac noise in the BOLD signal, and this type of noise varies throughout the brain [53, 221, 81], there is a possibility that between-group CRFg differences disappear for certain brain areas. Therefore, the shape of the CRFg was examined across different brain regions, namely the frontal cortex, the temporal cortex, the occipital cortex, and the parietal cortex. Masks for cortical regions were created using the WFU Pick Atlas tool for SPM [159, 158].

Different processing strategies

Different fMRI preprocessing strategies can also influence the shape of the CRFg. fMRI data were initially corrected for respiratory noise by removing RVT and respiratory RETROICOR regressors as surrogates for low- and high-frequency respiratory contributions. However, several definitions of respiratory regressors exist. For instance, low-frequency respiratory variations can be indexed either by RVT or RV, where each of them explains different variance in the BOLD signal [29, 53].

Similarly, high-frequency respiratory waveforms can be generated either by RETROICOR or by resampling the raw respiratory signal at the corresponding TR, as defined by Cordes *et al.* [64]. Besides, a common practice in fMRI data processing is to remove high-frequency cardiac components using cardiac RETROICOR regressors. This analysis was not previously performed to avoid altering the availability of cardiac noise in the BOLD signal. For the current evaluation analysis, cardiac RETROICOR regressors were also included along with RV and Cordes' high-frequency respiratory signals.

Specificity of group-specific CRFs

Finally, a between-group analysis was conducted to evaluate the specificity of the CRFg. The rationale for this analysis is that the CRFg is assumed to be the best function in its corresponding group (in terms of explained variance) modeling HR-induced fluctuations. Thus, exchanging any CRFg for another must decrease the explained variance as compared to the best CRFg (e.g. convolving HR regressors from the fast HR group with the CRFg from the slow HR group). To prove this assumption, each HR regressor from the slow HR group was convolved with the CRFg modeling fast HRs. The same procedure was applied to those HR regressors belonging to the fast HR group using the CRFg from the slow HR group.

3.3.2 Individual CRFs over different heart rates

The deviation of individual CRFs from a group average, i.e. CRFg, was also examined. This analysis allows us to accurately find HR ranges in which individual CRFs have similar shapes, and are, thus, useful for refining the formation of HR groups. By doing so, one can derive *HR-based* CRFs that can be applied later by simply knowing the subject's mean HR. The comparison of an individual CRF with its corresponding group-specific CRF was performed using the root-mean-square deviation (RMSD) index. For this analysis, only group-specific CRFs from slow and fast HR groups were considered. The RMSD was calculated as follow:

$$\begin{aligned} \text{RMSD}_{\text{SHR}_i} &= \sqrt{\frac{1}{12} \sum_{t=1}^{12} (\text{CRF}_{\text{gSHR},t} - \text{CRF}_{i,t})^2} \\ \text{RMSD}_{\text{FHR}_i} &= \sqrt{\frac{1}{12} \sum_{t=1}^{12} (\text{CRF}_{\text{gFHR},t} - \text{CRF}_{i,t})^2}, \end{aligned} \tag{3.5}$$

where CRF_{gSHR} and CRF_{gFHR} refer to the group-specific CRF from the slow and fast HR groups, respectively, and CRF_i are individual CRFs.

3.4 Derivation of CRF from grey matter or cerebrospinal fluid

RMSD values were plotted as a function of HR to find one or more cross-over points. The number of cross-over points will depend on the kind of function used to fit the data. For example, a linear fit will produce one cross-over or zero in case that the fitted lines for $\text{RMSD}_{\text{SHR}_i}$ and $\text{RMSD}_{\text{FHR}_i}$ do not cross. A cross-over point is a HR value at which the CRF changes its shape, e.g. from a curve with one peak to a curve with two peaks. Heart rates on each side of the cross-over point have similar CRF shapes, and groups are now based on this property.

If a CRF has not a well-defined form, the RMSD may be higher for the CRF_g assumed to correspond to that CRF. Therefore, K-means clustering was applied to quantify the number of subjects that were misclassified by the RMSD approach. K-means is one of the popular clustering algorithms, which identifies groupings of data objects based on the inter-object similarities computed by a chosen distance metric. K-means clustering was performed for the whole sample in an unsupervised manner with the squared Euclidean distance as the distance metric and both CRF_{gSHR} and CRF_{gFHR} as cluster centers.

3.4 Derivation of CRF from grey matter or cerebrospinal fluid

HR-based CRFs were derived from grey matter (GM) and cerebrospinal fluid (CSF) to examine the influence of neural-related fluctuations on the CRF shape. GM signal is influenced by both neural and non-neural sources, while CSF only contains non-neural contributions. Masks for both tissues were obtained by segmenting the co-registered anatomical images. Segmentation was performed using the unified segmentation algorithm available in SPM12 [6]. The algorithm uses a Gaussian mixture model for modeling tissue intensities, and so fits one (or several) Gaussians to the intensity histogram of each tissue class. This procedure is guided by a spatial prior on the probability of different tissues at a given position. The final step uses a simple Markov random field model post-processing to clean up the segmented tissue maps. A Markov random field is a method of describing the local structure of an image by defining a neighborhood system on the voxels of the image and a probability density function over the labeling of the voxels [168]. In this way, the Markov random field algorithm removes isolated voxels, which are unlikely to be a member of a certain tissue class.

The segmented tissue maps were binarized and resliced to functional data resolution. Finally, BOLD signals from GM and CSF were extracted by averaging all voxels within these masks. A notable advantage of the SPM segmentation is that prior probability maps are based on a large sample of healthy adults across the lifespan [100], which reduces bias when examining subjects of different ages.

3.5 Noise correction on the default mode connectivity

The effect of CRF as a potential physiological noise correction method was assessed on the default mode network (DMN) connectivity. In agreement with previous studies investigating the effect of physiological noise correction on the DMN [53, 99], a spherical ROI of 10 mm radius was drawn in the PCC for seed correlation analyses (MNI coordinates $x = -4$, $y = -56$, $z = 22$; Figure 3.4).

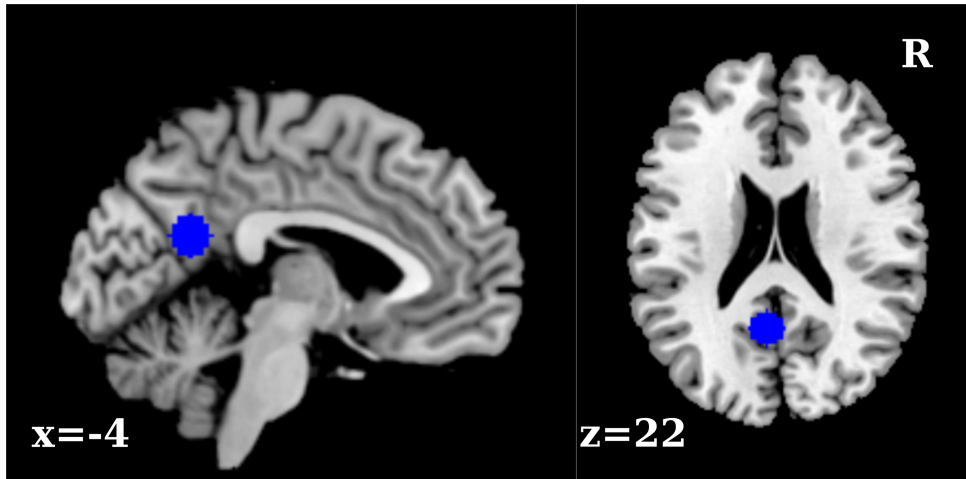


Figure 3.4: Location of the seed region in the posterior cingulate cortex.

To obtain resting-state functional connectivity (FC) maps, physiological noise correction was performed on the preprocessed rs-fMRI data using the regressor formed by the convolution of the HR regressor with its corresponding *HR-based* CRF (CRF_{HR} , see Table 3.3). Residual data were then pass-band filtered to retain frequencies between 0.01-0.1 Hz. Noise correction and temporal filtering were conducted in one step using the AFNI program: 3dTproject. Filtered data were subsequently normalized to MNI space using the deformation field and written to a final voxel size of $2 \times 2 \times 2 \text{ mm}^3$. The next step involved the correlation (Pearson) of the average time series within the PCC mask with all brain voxels. The Pearson correlation coefficient was converted into a more normally distributed variable via the Fisher Z transform [258]. The resulting functional connectivity maps were thresholded at voxel-level $p < 0.001$ (uncorrected). For comparison purposes, the same procedure was repeated convolving the HR regressor with the canonical CRF during the physiological noise correction step.

3.6 Analysis of the influence of CRF on the CAN connectivity

The impact of CRF on the central autonomic network (CAN) connectivity was also examined in a physiological noise correction framework. This analysis aims to answer the question of whether the noise modeled by CRF undermines the known associations between HR and FC in the CAN in subjects with different HRs. The CAN connectivity was assessed using the right amygdala as a seed region [56]. A mask for the right amygdala (Figure 3.5) was created using the WFU Pick Atlas tool for SPM [159, 158].

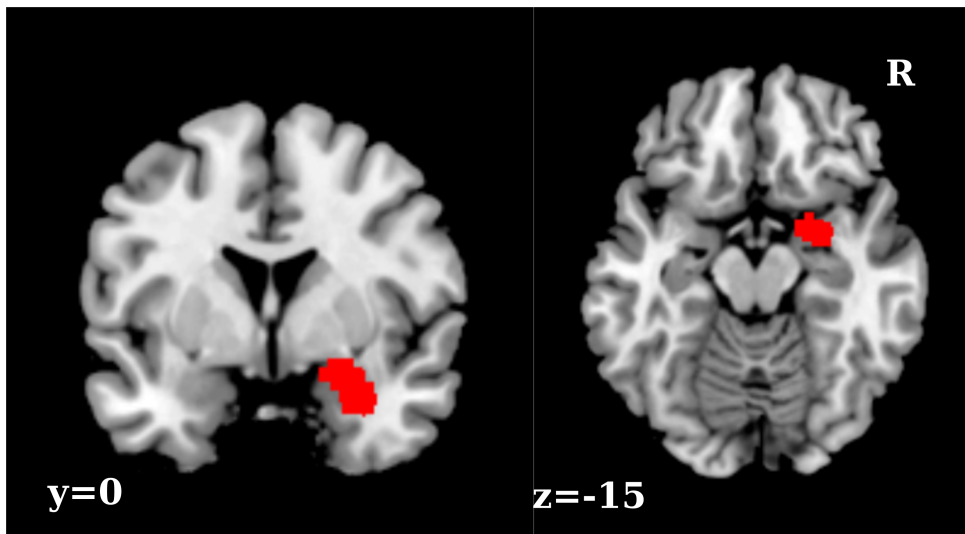


Figure 3.5: Location of right amygdala seed region.

For this analysis, subjects were separated into slow and fast HRs according to the HR cross-over point derived from the analysis described in 3.3.2. Processing of rs-fMRI data was conducted similarly as in the previous section, i.e. physiological noise correction using the HR regressor convolved with its corresponding *HR-based* CRF, time filtering (0.01-0.1 Hz), normalization to MNI space, correlation between the right amygdala time series and all brain voxels and Fisher's Z transformation. Similarly, processing without physiological noise correction was performed for comparison purposes. The effect of physiological noise regression on the amygdala connectivity was assessed using a two-sample t-test comparing groups with slow and fast HRs. The resulting statistical map was thresholded at voxel-level $p < 0.005$ and cluster corrected at $p < 0.05$ using Monte Carlo simulations (*ClustSim* function implemented in the AFNI program 3dttest++). *ClustSim* computes the probability of a random field of noise producing a cluster of a given size after the noise is thresholded at a given level [65].

Also, for comparison purposes, an independent sample consisting of 18 subjects was scanned and processed in the same way as the large sample of 84 subjects. For this small sample, T_2^* -weighted images were obtained using a multiband multislice GE-EPI sequence (TR = 484 ms,

TE = 30 ms, flip angle = 90°, multiband factor = 8) with 56 contiguous transverse slices of 2.5 mm thickness covering the entire brain and including the lower brainstem. The matrix size was 78 × 78 with an in-plane resolution of 2.5 × 2.5 mm² corresponding to a FOV of 195 mm × 195 mm. A series of 1900 whole-brain volume sets was acquired in one session lasting approximately 15 minutes. Due to the small size of this sample, the voxel-level statistical threshold was set at $p < 0.005$ and not corrected for multiple comparisons.

Simulations of aliasing effects

The TR of 2.52 s used for the main sample did not resolve the fundamental cardiac frequencies. Therefore, it is conceivable that cardiac aliasing effects may influence the association between HR and FC in the CAN. To address this important issue, a simulation of aliasing effects on functional connectivity was conducted using different TRs and HRs.

Time series of neural activity were generated using a vector autoregressive (VAR) model simulating Local Field Potentials (LFPs). Accumulating evidence suggests that LFPs response is a strong predictor of BOLD activity given the high correlation between LFPs and BOLD response [154]. As a generator of LFPs, a slight variation of a simple VAR model defined by Roebroek *et al.* [207] was adopted. VAR modeling of fMRI time-series has been widely used for the identification of effective connectivity of distinct brain regions [207, 218]. The VAR model can be thought of as a linear prediction model that predicts the current value of the time series y based on a linear combination of the most recent past p values given by:

$$y_n = \sum_{i=1}^p A_i y_{n-i} + v_n, \quad (3.6)$$

where A_i are the autoregression coefficients, v represents white noise with covariance matrix $\text{var}(v_n) = \Sigma$ and measures how well the VAR model can predict current values of y from their past values.

In this study, two interacting neural populations were generated as a realization of a bi-dimensional first-order VAR process with autoregression coefficients $A = \begin{bmatrix} 0.9 & 0 \\ 0.2 & 0.9 \end{bmatrix}$ and white noise with covariance matrix $\Sigma = \begin{bmatrix} 1 & 0 \\ 0 & 1 \end{bmatrix}$ [207]. A timestep of 2 ms (matching the physiological data recording frequency) was assumed and time series were generated with a length of 650 s, from which the first 50 s were discarded to allow the system to enter a steady state [218], thus simulating a standard rs-fMRI acquisition of 10 minutes. To generate BOLD signals, the VAR model output was convolved with the canonical hemodynamic response function (hrf) expressed

3.6 Analysis of the influence of CRF on the CAN connectivity

as the difference between two gamma functions [96] and a duration of 25 s:

$$hrf = c_1 t^{n_1} e^{-t/t_1} - a_2 c_2 t^{n_2} e^{-t/t_2}, \quad (3.7)$$

where $n_1 = 6.0$, $t_1 = 0.9$, $n_2 = 12.0$, $t_2 = 0.9$, $a_2 = 0.35$ and c_i are scale factors given by:

$$c_i = \max(t^{n_i} e^{-t/t_i}), \quad (3.8)$$

Cardiac noise was generated using sinusoidal waveforms with random phases at the fundamental frequency. Harmonics up to order two were subsequently added to the sinusoid to account for an additional source of aliasing. Since the amplitude of harmonics tends to decrease with the order of the harmonic [63], the first and second harmonic were a half and a quarter of the amplitude of the fundamental frequency sine wave, respectively. The resulting sinusoid was then converted into a non-stationary signal after adding a fifth-order polynomial trend [178] with random coefficients. This trend explicitly accounts for the effect of ultra-slow non-periodic variations in the PPG signal due to some physiological or emotional activity [179]. The presence of non-stationarity was confirmed by the Augmented Dickey-Fuller test ($p < 0.05$) [76]. Since the specific amount of physiological cardiac noise is not clear due to the variability reported in previous studies [23, 68, 221], cardiac pulsations were defined as the dominant source of noise (40%).

Cardiac-corrupted BOLD signals were sampled at three different TRs: $TR = 2.52$ s to simulate fMRI signal acquisition in the present study, $TR = 0.72$ s to simulate data acquired in the Human Connectome Project [247], and $TR = 0.1$ s to simulate the absence of aliasing. After sampling, additional white Gaussian noise (20%) was added to mimic measurement error and noise in the acquisition [207]. Finally, BOLD signals were pass-band filtered into the resting-state band (0.01-0.1 Hz), and functional connectivity was estimated. The “true” connectivity, i.e. the correlation between both BOLD signals without any source of noise, was 0.3 - a typical value encountered in simulations [27, 220, 190] and real data [259, 87]. The whole procedure was repeated by varying the frequency of the PPG signal over the range 40-120 bpm in steps of 1 bpm. An illustration of a simulated cardiac signal and the processing pipeline is shown in Figure A.1 in Appendix A.1.

4 Results

4.1 Physiological indices

As described in section 3.1.1, the entire dataset (84 subjects) was initially divided into three groups, slow HR (54.84 ± 5.34 bpm), medium HR (66.95 ± 3.52 bpm), and fast HR (81.27 ± 7.64 bpm), as shown in Figure 4.1.

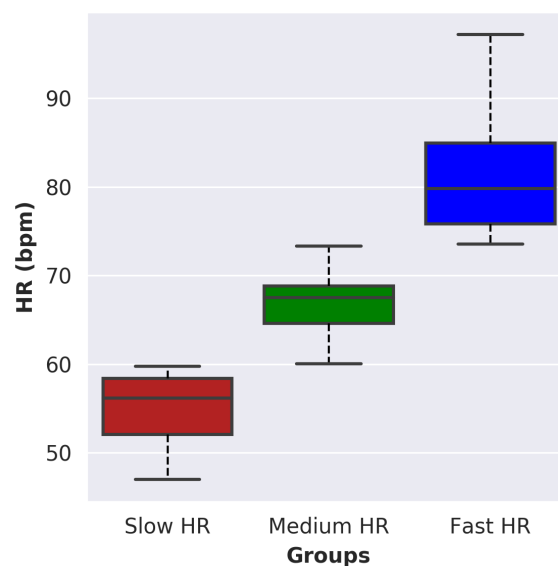


Figure 4.1: Boxplot showing the heart rate groups. The groups differ significantly from each other (ANOVA, $p < 10^{-32}$). The central line of the box represents the median, while the ends of the boxes represent upper and lower quartiles (i.e. where the middle half of the data lie). The whiskers (dashed lines extending from opposite edges of the box) show the minimum and maximum values.

Table 4.1 summarizes the demographic data and calculated physiological indices across HR groups. Along with age and gender, there were no significant differences between groups in reported frequency of physical exercise, respiratory rate, number of spontaneous skin conductance fluctuations, and skin conductance level. All HRV indices, i.e. RMSSD, LF/HF, and RSA, differed significantly between groups.

4.2 Relationship between heart rate and BOLD spectra

Table 4.1: Demographic and physiological data. Values are represented by mean \pm standard deviation.

Parameter	Slow HR	Medium HR	Fast HR	<i>p</i> -value [†]
Number of participants (n)	28	28	28	
Sex (m/f)	16/12	9/19	16/12	0.10 [‡]
Age [years]	31.14 \pm 10.43	32.11 \pm 10.83	31.50 \pm 11.00	0.95
Self-rated frequency of physical exercise	3-4 times/week(11 ^a)	1-2 times/week(27 ^a)	1-2 times/week(27 ^a)	0.85 [‡]
Respiratory rate [breaths/minute]	15.71 \pm 2.80	16.84 \pm 2.97	15.75 \pm 4.02	0.37
RMSSD [ms]	73.86 \pm 29.06	47.36 \pm 20.81	34.08 \pm 16.14	3.02x10 ⁻⁸
LF/HF	1.09 \pm 0.47	1.45 \pm 1.13	2.61 \pm 2.70	4.14x10 ⁻³
Respiratory sinus arrhythmia [ms]	112.01 \pm 50.74	82.94 \pm 42.53	71.16 \pm 38.65	3.41x10 ⁻³
Spontaneous skin conductance fluctuations	15.64 \pm 21.60	23.18 \pm 24.17	25.93 \pm 25.50	0.26
Skin conductance level [μ s]	0.88 \pm 0.76	0.62 \pm 0.38	0.95 \pm 0.95	0.24

[†] *p*-values from one-way ANOVA

[‡] *p*-values from χ^2 test

^a number of participants providing information

RMSSD = root-mean-square of successive IBI differences; ms = milliseconds; μ s = microseconds; LF/HR = ratio of low- to high-frequency components of HRV

4.2 Relationship between heart rate and BOLD spectra

Power spectral densities (PSDs) were estimated from HR variability (HRV) and whole-brain global signals to test the hypothesis of an association between HR and BOLD spectra. PSDs were computed by using the multitaper method, which provides high spectral resolution and reduces estimation bias in comparison to the traditional Fourier transform.

Figure 4.2A shows the average PSD of HRV. Both groups with slow and fast HR showed similar PSD in the range below 0.05 Hz (Figure 4.2A, left). Interestingly, all HR groups displayed a well-defined second maximum in the range 0.05-0.18 Hz peaking around 0.1 Hz, whose amplitude was proportional to HR. This behavior changes above 0.18 Hz, where the faster HR group exhibited smaller PSD values. Statistical comparisons of spectral power in the 0-0.2 Hz frequency range (area under the curve) revealed a significant effect of group ($F(2, 81) = 4.73, p < 0.05$), with the FHR group showing significantly higher power than the SHR ($p < 0.001$) and MHR ($p < 0.05$) groups (Figure 4.2A, right).

Figure 4.2B (left) shows the average PSD of the whole-brain global signal. The spectra display the characteristic frequency distribution commonly found in resting-state BOLD data for frequencies above 0.01 Hz, i.e. the power spectrum is proportional to the inverse of the frequency (grey dashed curve). The 1/*f*-like curve is particularly noticeable for SHR and MHR groups, while the spectrum of the FHR group exhibits similarities with the HRV spectra. Specifically, the FHR group also showed the second peak at around 0.1 Hz as its HRV counterpart. Moreover, between-group comparisons of spectral power revealed that the FHR group had significantly ($p < 0.01$) higher power in the 0.01-0.2 Hz frequency range than the SHR group (Figure 4.2B, right).

4.2 Relationship between heart rate and BOLD spectra

To assess the relationship between HRV and BOLD spectral powers, individual HRV power in the 0-0.2 Hz range was correlated with individual BOLD power in the 0.01-0.2 Hz range for all 84 volunteers. This correlation analysis yielded a significant positive relationship ($r = 0.26$, $p < 0.05$) between spectral powers (Figure 4.2C), suggesting that different HRs relate to different profiles of BOLD signal.

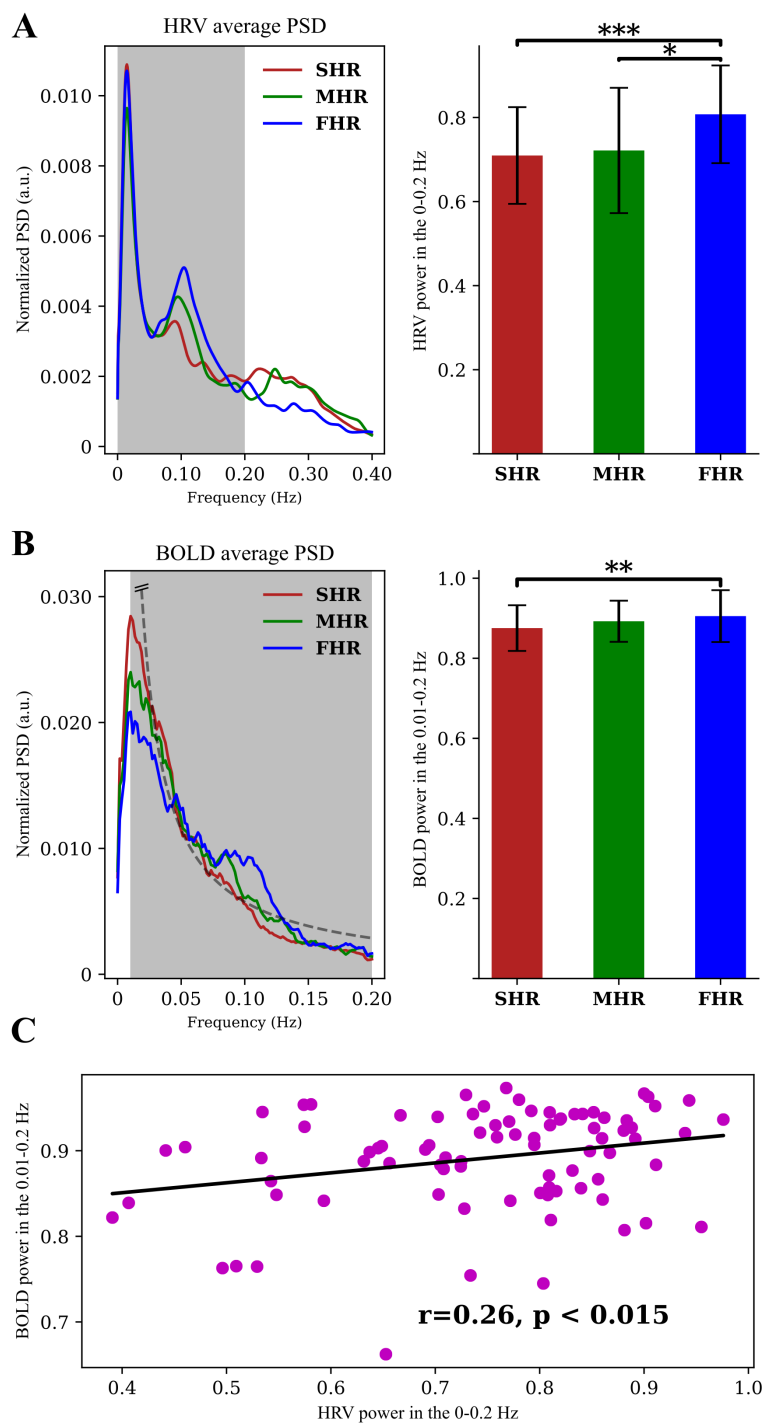


Figure 4.2: **A)** Group average PSDs of HRV (left). Between-group comparisons of HRV spectral power in the 0-0.2 Hz range (grey colored area) revealed significantly higher power in the FHR than in the SHR and MHR groups (right). **B)** Group average PSDs of the BOLD whole-brain global signal (left). BOLD spectra follow approximately a $1/f$ curve (grey dashed). Between-group comparisons of BOLD spectral power in the 0.01-0.2 Hz range (grey colored area) revealed significantly higher power in the FHR than in the SHR group (right). **C)** Linear regression analysis between HRV and BOLD spectral powers.

Abbreviations: SHR, slow heart rate group; MHR, medium heart rate group; FHR, fast heart rate group; * $p < 0.05$, ** $p < 0.01$, *** $p < 0.001$, Bonferroni-corrected Mann-Whitney U-test.

4.3 Heart rate and cardiac response function

To test the hypothesis that HR is an essential factor influencing the shape of the CRF, individual CRFs were averaged within each HR group, i.e. slow HR, medium HR, and fast HR groups. Averaging allows us to amplify between-group differences that may arise as a result of varying HR while minimizing the peaks that are due to noisy CRFs.

Figure 4.3 shows the average group-specific CRF (referred to herein as CRF_g) extracted from the whole-brain global signal. The CRF_g of the SHR group (CRF_{gSHR}; Figure 4.3A) displays a similar shape to the canonical CRF. However, there are some marked differences in the peak and dip between the two functions. The CRF_{gSHR} shows a maximum at 3 s, which occurs slightly earlier than the canonical CRF (4 s), as well as a minimum at 11 s in contrast to the 12 s of the canonical CRF. The CRF_g of the MHR group (CRF_{gMHR}; Figure 4.3B) also displays a similar shape as the canonical CRF and peaks approximately at 3 s (similar to CRF_{gSHR}), but its minimum occurs slightly earlier (~10 s) than that of the CRF_{gSHR}. Interestingly, the CRF_{gMHR} exhibits larger standard errors than the CRF_{gSHR} and the CRF_g of the FHR group (CRF_{gFHR}), in particular, for the time points of the “post-stimulus overshoot period” indicated by the magenta rectangle in Figure 4.3B. This observation suggests that the shape of the CRF_{gMHR} may be considered a mixture of CRF_{gSHR} and CRF_{gFHR}. Conversely, the CRF_{gFHR} (Figure 4.3C) shows a more pronounced second maximum at 17 s as well as an earlier dip (~10 s) than the CRF_{gSHR} and the canonical CRF.

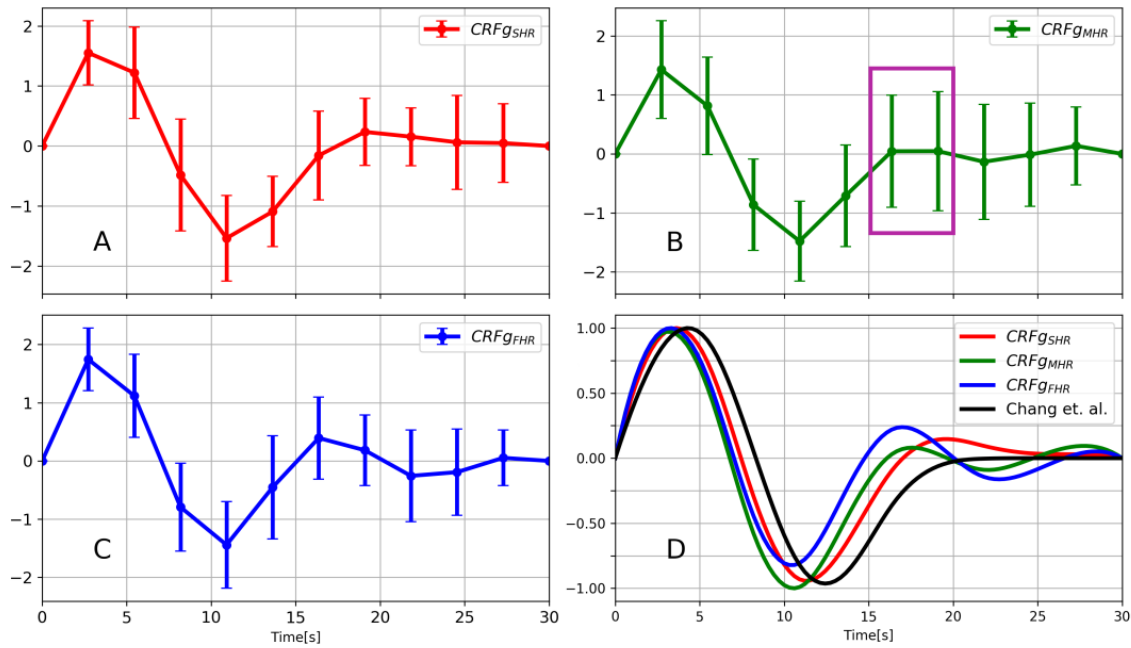


Figure 4.3: Group-specific averaged CRFs. (A) CRF of the slow heart rate group ($CRF_{g_{SHR}}$), (B) CRF of the medium heart rate group ($CRF_{g_{MHR}}$), and (C) CRF of the fast heart rate group ($CRF_{g_{FHR}}$). The error bars show the standard errors. (D) The canonical CRF (black line, Chang *et al.* [53]) is depicted along with all CRFg after interpolation and normalization between -1 and +1 for illustration.

In a next step, the *canonical CRF* as proposed by Chang *et al.* [53] (referred to herein as CRF_c), the *individual CRF* as suggested by Fahlapour *et al.* [81] (referred to herein as CRF_i), and the group-specific CRFs (CRF_g) were convolved with the HR regressor and compared to each other in terms of:

- (1) the percentage of brain voxels (relative to the whole-brain mask) with significant R^2 ($p < 0.01$), where R^2 is the BOLD signal variance explained by the convolved HR regressor.
- (2) the percentage of R^2 averaged over voxels with significant results, i.e. over voxels in (1).

Canonical CRF

(1) After convolving the HR regressor with the CRF_c , the percentage of brain voxels where R^2 exceeded the statistical threshold ($p < 0.01$) varied between 6% and 10% depending on the HR group (Table 4.2 and Figure 4.4). For instance, on average, 10.3% of all brain voxels had significant R^2 in subjects with slow HR. This amount was markedly lower in both groups with faster HR, i.e. the MHR and FHR groups, where the percentage of brain voxels was 6.1% and 6.3%, respectively.

This varying fraction of brain voxels across groups was naturally reflected in the number of brain regions identified in each group (Figure 4.4). In the SHR group, these regions were widely

distributed throughout the brain. Major clusters were located in the visual cortex and core regions of the default mode network, namely the posterior cingulate cortex/precuneus, the angular gyrus, and the medial prefrontal cortex. Other areas sharing significant variance are the midcingulate cortex, the thalamus, and the right insula, which are all involved in autonomic processing and are part of the central autonomic network. As expected, the fraction of brain voxels was strongly reduced in the MHR and FHR groups. Even in areas sensitive to physiological noise like the sinuses, the CRFc did not explain much variance. R^2 maps of three representative subjects from each group are shown in Figure 4.5 to illustrate better the effect of reduced variance explained by the CRFc at faster HRs.

(2) The percentage of R^2 , averaged over significant voxels, was around 4% in the MHR and FHR groups. In the SHR group, it was slightly higher (4.3%), in line with the observation that the CRFc seems more suitable for modeling slower HRs. Percentages of brain voxels and average R^2 for each subject are shown in Table A.1 in Appendix A.2.

Based on the results in (1) and (2), the range of HR in which the CRFc effectively models HR-induced fluctuations appears to be restricted to subjects exhibiting slow HR, which evidences the necessity to create additional CRFs to include further ranges of HR.

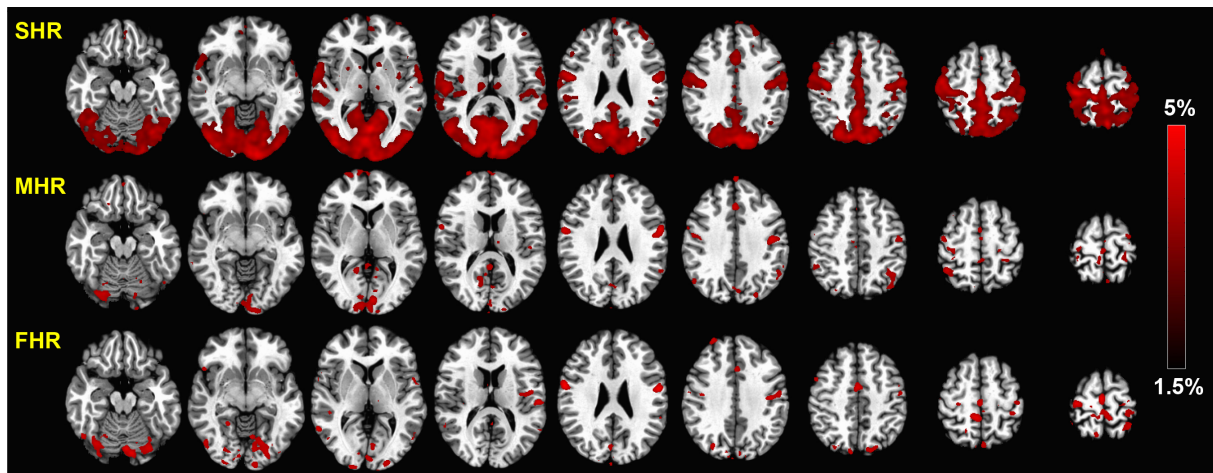


Figure 4.4: Group average R^2 maps for slow heart rate (SHR), medium heart rate (MHR), and fast heart rate (FHR) groups after convolving HR with the canonical CRF as proposed by Chang *et al.* [53]. While the variance explained by the canonical CRF covers an extensive area in the SHR group, these areas are much smaller in both groups with faster HR. The color bar indicates percent signal variance explained by the CRFc.

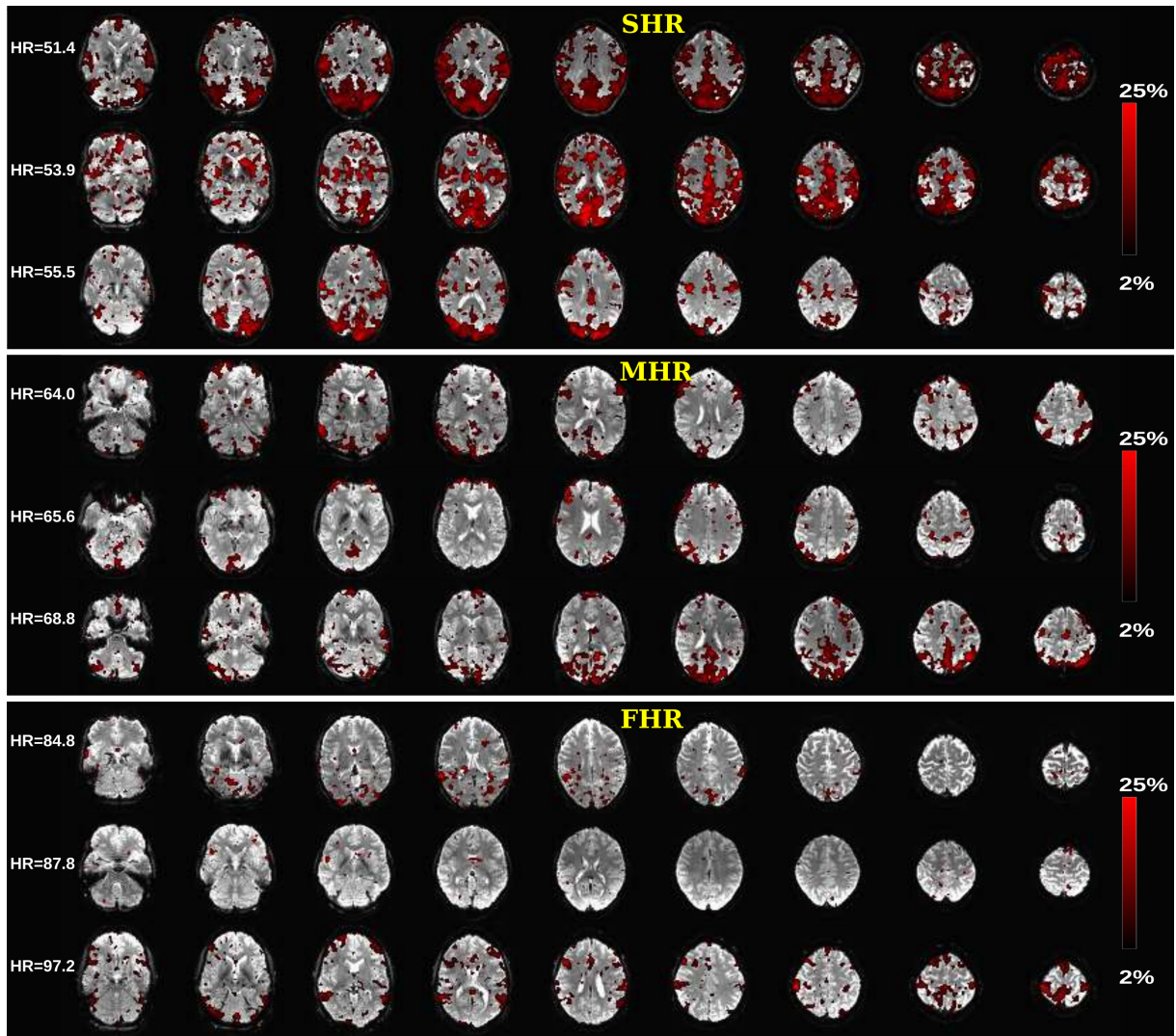


Figure 4.5: R^2 maps of three representative subjects in each group ($p < 0.01$, F -test). Each R^2 map represents the percentage of variance explained by the HR regressor convolved with the canonical CRF. Similar to the group results, the canonical CRF explains variance over an extensive area in the SHR group, but the area rapidly decreases for faster HR (MHR and FHR). The numbers on the left side represent the subject's HR in units of beats-per-minute. Color bars indicate percent signal variance explained by the CRF_c.

Abbreviations: SHR, slow heart rate group; MHR, medium heart rate group; FHR, fast heart rate group.

Individual CRF

(1) Figure 4.6 shows the group average R^2 maps after convolving each subject's HR regressor with its corresponding CRF_{*i*}. Except for the SHR group, CRF_{*i*} explained significant signal variance ($p < 0.01$) over a greater spatial extent than the CRF_c. On average, the percentage of brain voxels where R^2 exceeded the statistical threshold was 7.9%, 9.5%, and 7.8% in the SHR, MHR, and FHR groups, respectively. The spatial distribution of these voxels did not differ considerably from that obtained with the CRF_c. The occipital cortex was the region with the greatest spatial extent significantly modeled by the CRF_{*i*}.

(2) The percentage of signal variance accounted for by the CRF_i , averaged over significant voxels, was slightly lower than that by the CRF_c in the SHR group (CRF_i 4.2%, CRF_c 4.3%). However, in the MHR (CRF_i 4.3%, CRF_c 4.0%) and FHR (CRF_i 4.1%, CRF_c 4.0%) groups using the CRF_i led to a slightly higher explained variance compared to using CRF_c , as shown in Table 4.2. Although these differences may seem small at first glance, they are relevant for physiological noise correlation since the BOLD signal variance attributable to neural activity is typically on the order of only a few percent [216]. Percentages of brain voxels and average R^2 for each subject are shown in Table A.1 in Appendix A.2.

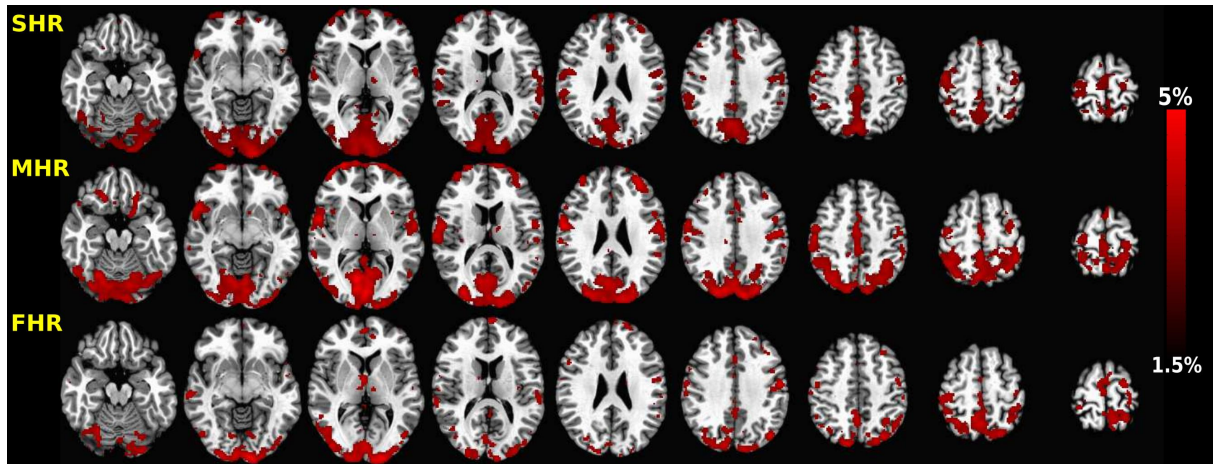


Figure 4.6: Group average R^2 maps for slow heart rate (SHR), medium heart rate (MHR), and fast heart rate (FHR) groups after convolving HR with its corresponding CRF_i . In the MHR and FHR groups, the CRF_i explained significant variance in the BOLD signal over a greater spatial extent than the canonical CRF. The color bar indicates percent signal variance explained by the CRF_i .

Group-specific CRF

(1) Figure 4.7 shows the group average R^2 maps after convolving the HR regressor with the corresponding CRF_g . A sharp increase in the number of voxels, where R^2 exceeded the statistical threshold ($p < 0.01$), was mainly observed in the MHR (51%) and FHR (38%) groups compared to the results obtained with CRF_c (see Table 4.2). There was also a considerable increase in the number of voxels in the SHR group (14%) convolving the HR regressor with the CRF_{gSHR} . The CRF_g method also accounted for a larger portion of the brain than CRF_i . For example, using the CRF_g increased the number of brain voxels by 48.1% in the SHR group and by 11.5% in the FHR group in comparison to CRF_i . However, using the CRF_{gMHR} slightly reduced the number of brain voxels in its group by -3.2% when compared to CRF_i .

For comparison purposes, Figure 4.8 shows the same three representative subjects per group shown in Figure 4.5. Compared to applying the CRF_c , CRF_g increased notably the percentage of voxels in subjects with HR of 65.6 bpm, 87.8 bpm, and 97.2 bpm.

4.3 Heart rate and cardiac response function

(2) The application of CRFg slightly outperformed the use of CRFc in explaining variance in the BOLD signal. With CRFg, the explained variance, averaged over significant voxels, increased by 2.3%, 7.5%, and 2.5% in the SHR, MHR, and FHR groups, respectively. Compared to CRFi, CRFg was more effective in the SHR group, in which the explained signal variance increased by 4.8%. Percentages of brain voxels and average R^2 for each subject are shown in Table A.1 in Appendix A.2.

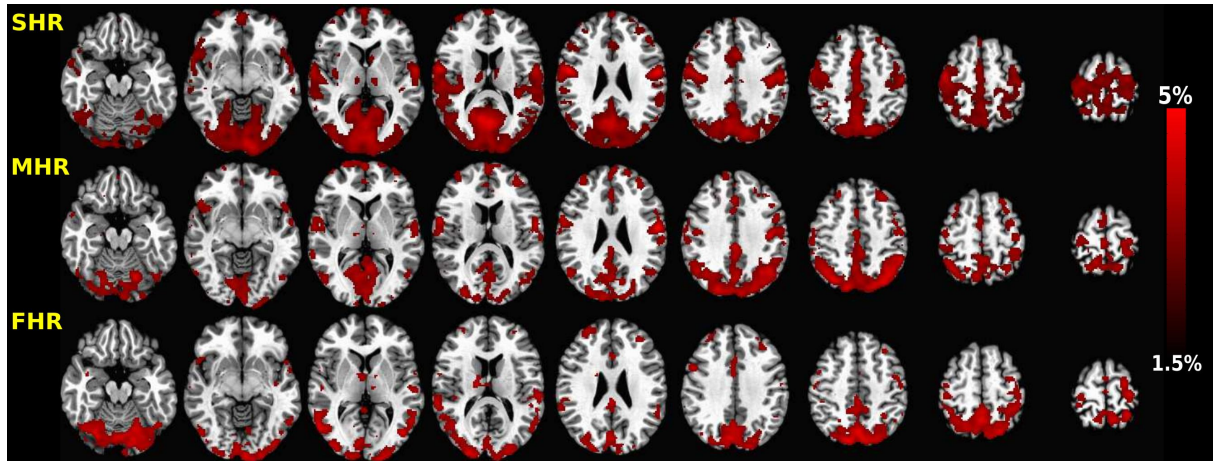


Figure 4.7: Group average R^2 maps for slow heart rate (SHR), medium heart rate (MHR), and fast heart rate (FHR) groups after convolving HR with the CRFg. The percentage of significant voxels increased in comparison to the CRFc. The color bar indicates percent signal variance explained by the CRFg.

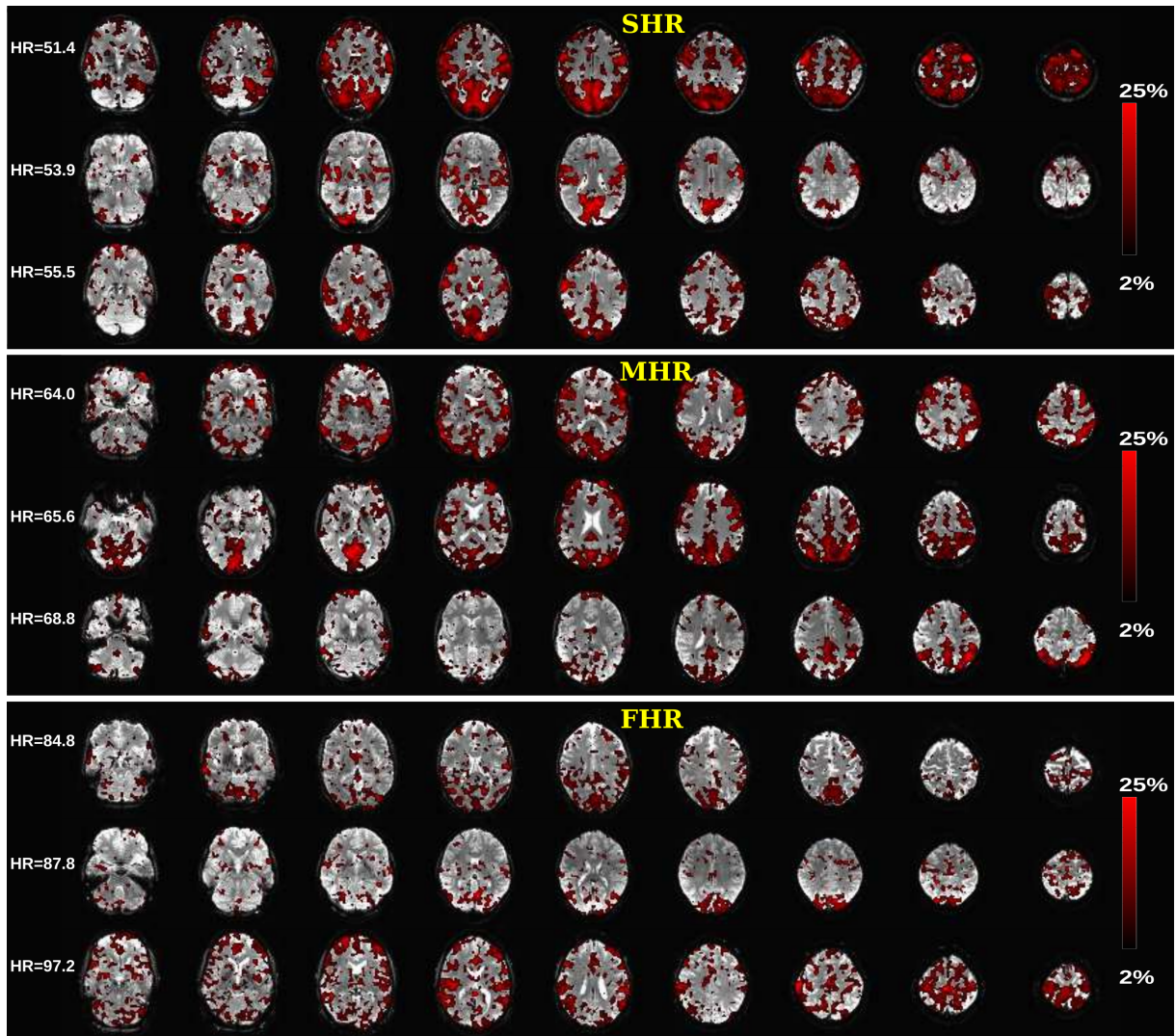


Figure 4.8: R^2 maps of the same three representative subjects shown in Figure 4.5 after convolving HR with the CRFg ($p < 0.01$, F -test). A large increase in the number of brain voxels is observed in subjects within the MHR and FHR groups. Color bars indicate percent signal variance explained by the CRFg. *Abbreviations:* SHR, slow heart rate group; MHR, medium heart rate group; FHR, fast heart rate group.

In summary, the results indicate that HR plays an essential role in determining the CRF shape. While the canonical CRF modeled HR-induced fluctuations at slower HRs very well, it has a rather modest performance for faster HRs. The individualized method was particularly suitable for medium and fast HR groups. In both groups, individual CRFs explained significant signal variance over a greater spatial extent than the canonical CRF. However, an individualized approach can be substituted by a more generalized one such as the group-specific CRF, which preserves the inter-subject variability and works, in general, better than canonical and individual CRF methods (see Table 4.2).

Table 4.2: Average percentage of variance explained in each group after convolving the HR regressor with different cardiac response functions. % voxels: indicates percentage of voxels in the brain with significant R^2 ($p < 0.01$, F -test). Mean % R^2 corresponds to % R^2 values averaged over significant voxels, while SD indicates the standard deviation.

	canonical CRF		individualized CRF		group-specific CRF	
	% voxels	% R^2 mean \pm SD	% voxels	% R^2 mean \pm SD	% voxels	% R^2 mean \pm SD
Slow HR	10.3	4.3 \pm 1.3	7.9	4.2 \pm 1.3	11.7	4.4 \pm 1.5
Medium HR	6.1	4.0 \pm 1.2	9.5	4.3 \pm 1.4	9.2	4.3 \pm 1.4
Fast HR	6.3	4.0 \pm 1.1	7.8	4.1 \pm 1.3	8.7	4.1 \pm 1.2
Grand mean	7.6	4.1 \pm 1.2	8.4	4.2 \pm 1.3	9.9	4.2 \pm 1.4

4.3.1 Evaluation

From the previous analysis, it seems that CRFg is well suited to model HR-induced fluctuations in the BOLD signal. Further post hoc analyses were conducted to evaluate CRFg according to different criteria.

CRFg across brain regions

Small within-group differences in the CRF shape were detected across all brain regions, with the most prominent occurring in the occipital lobe, as shown in Figure 4.9. This region also showed the highest inter-subject variability and the smallest amplitude of the CRFg. Overall differences were principally observed in the amplitude and, to a lesser extent, in the CRFg shape. Despite all this, most regional group-specific CRFs resemble the whole-brain CRFg (black curve), indicating that the dependence of CRFg on HR is more dominant than the spatial variability of HR-related noise.

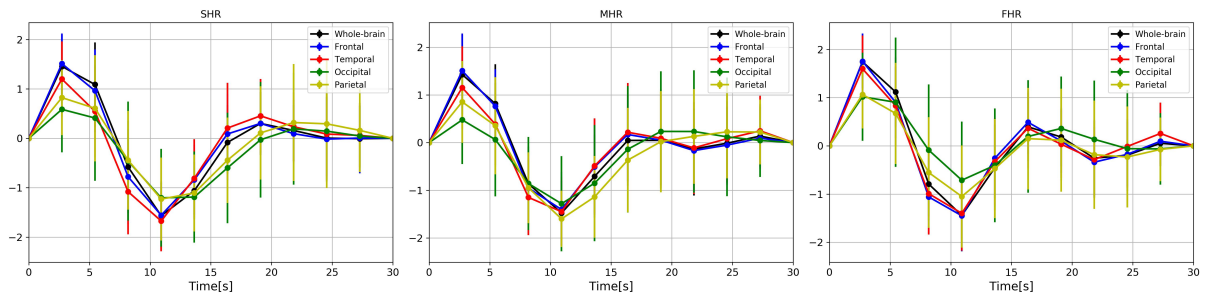


Figure 4.9: Group-specific CRF estimated from different brain regions, namely the frontal cortex, the temporal cortex, the occipital cortex, and the parietal cortex. The CRFg derived from the GS is also shown for comparison purposes.

Abbreviations: SHR, slow heart rate group; MHR, medium heart rate group; FHR, fast heart rate group; GS, whole-brain global signal.

CRFg using different processing strategies

Changing the physiological regressors during the noise correction step leads to slight changes in the shape of the CRFg in comparison to the initial approach, as shown in Figure 4.10. Differences mainly resided in the amplitude of the CRFg, which were more noticeable in the SHR group than in the groups with faster HR. The FHR group was barely affected by the new physiological noise correction approach. In summary, this analysis revealed that CRFg is robust to different physiological noise correction approaches, or in other words, the dependence of CRFg on HR still holds if one removes respiratory and high-frequency cardiac noise from the fMRI data.

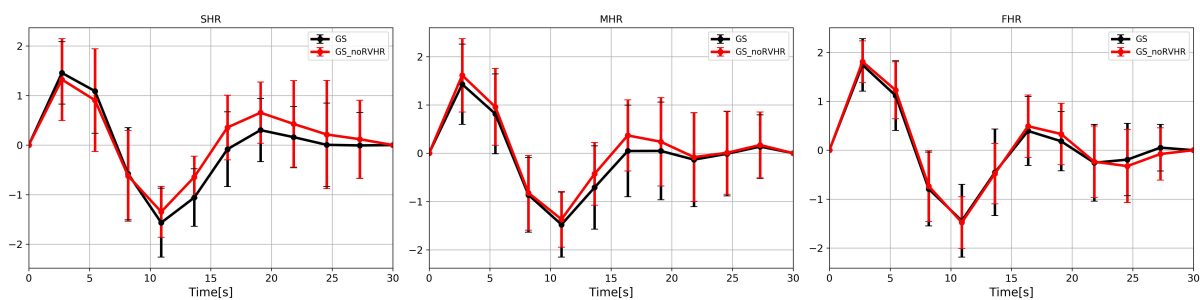


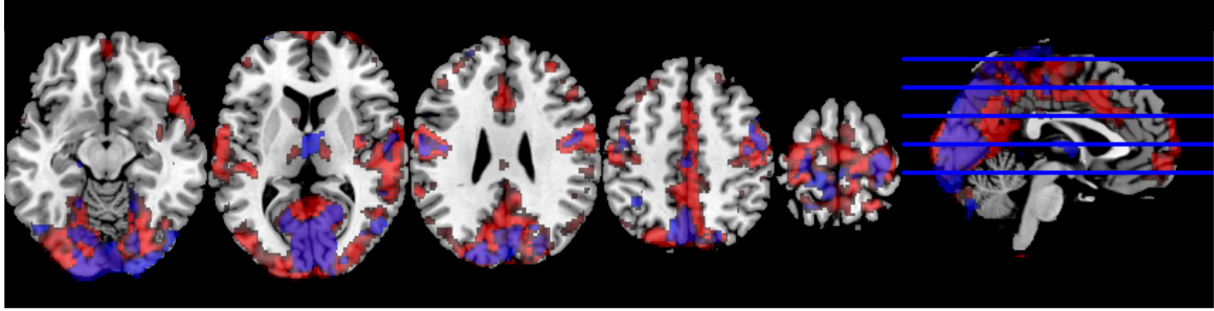
Figure 4.10: Comparison of CRFg using different physiological noise correction methods. GS: original CRFg; GS_noRVHR: CRFg derived after regressing out RV and high-frequency components of the respiratory and cardiac signals.

Abbreviations: SHR, slow heart rate group; MHR, medium heart rate group; FHR, fast heart rate group.

Specificity of CRFg

Figure 4.11 shows the results of exchanging the CRFg between HR groups to assess the specificity of the CRFg. The top row shows the group average R^2 map with the CRFg_{FHR} used in the SHR group (blue map), and the bottom row shows the group average R^2 map with the CRFg_{SHR} used in the FHR group (blue map). For comparison purposes, the convolution with the “correct” CRFg is shown in red. Both groups showed a substantial reduction in the number of voxels with significant R^2 when using a “wrong” CRFg, with the largest reduction occurring in the SHR group. Convoluting with CRFg_{FHR} reduced the number of voxels by 38% in the SHR group and by 17% in the FHR group after convolution with CRFg_{SHR}. Reductions were more prominent in medial and temporal regions in the SHR group, whereas the parietal cortex was the most affected region in the FHR group. The fact that exchanging the CRFg decreases considerably the explained variance indicates that each group is presumably described by one specific response function.

$\text{SHR} * \text{CRFg}_{\text{FHR}}$, $\text{SHR} * \text{CRFg}_{\text{SHR}}$



$\text{FHR} * \text{CRFg}_{\text{SHR}}$, $\text{FHR} * \text{CRFg}_{\text{FHR}}$

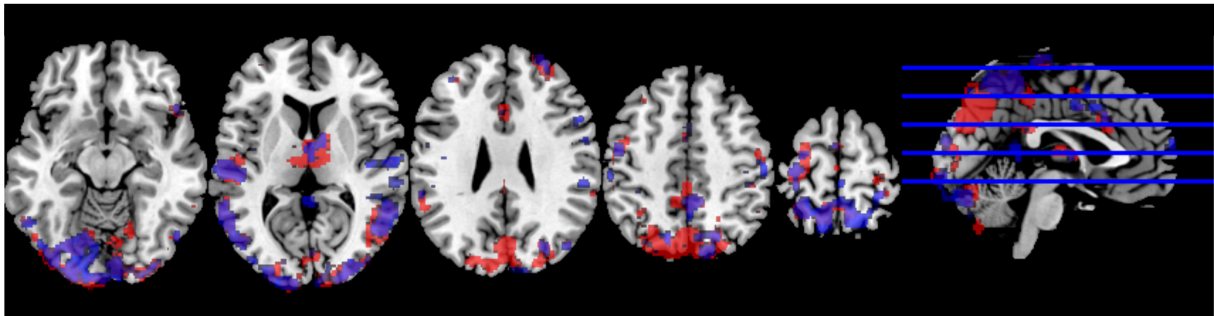


Figure 4.11: Group average R^2 maps obtained by using a “wrong” CRFg. Convolution with the “wrong” CRFg is shown in blue, while convolution with the “correct” CRFg is shown in red for comparison. The convolution of the HR regressor with the CRFg from another group considerably decreases the number of voxels with significant R^2 in comparison to the correct CRFg. Reductions are stronger in the SHR group, evidencing that a unique and specific CRF presumably describes each group. All R^2 maps are thresholded between 1.5% and 5%.

Abbreviations: SHR, slow heart rate group; FHR, fast heart rate group.

4.3.2 Change in the CRF shape as a function of heart rate

Arbitrary ranges of HRs were initially defined to separate the sample into three groups and test the hypothesis that HR is an essential factor influencing the shape of the CRF_i . As indicated earlier, the CRFg_{SHR} is characterized by a smooth shape similar to that of the canonical CRF, while the CRFg_{FHR} depicts two pronounced peaks. Furthermore, it was observed that CRFg_{SHR} and CRFg_{FHR} exhibited smaller standard errors compared to CRFg_{MHR} , indicating higher stability of the CRF shape for these two groups. On the other hand, the CRFg_{MHR} showed larger standard errors, which suggest that the MHR group potentially contains a mixture of both CRFg_{SHR} and CRFg_{FHR} . In light of these findings, one can assume the existence of an HR point at which the CRF changes from a single- to a double-peak shape.

To find this HR point, the root-mean-square deviation (RMSD) between CRFg_{SHR} and CRFg_{FHR} , and all individual CRFs was computed (Equation 3.5). Before computing RMSD, all CRFs were scaled between -1 and +1. RMSD results were then fitted as a function of HR with

4.3 Heart rate and cardiac response function

straight lines by linear regression, yielding $y = 0.0021x + 0.0327$ and $y = -0.0023x + 0.3310$ for $CRF_{g_{SHR}}$ and $CRF_{g_{FHR}}$, respectively. The fact that both curves show small slopes is in line with the stability of the shape of individual CRFs in the slow and fast HR groups.

The point at which both fitted curves cross each other corresponds to the proposed HR at which the CRF changes from a single- to a double-peak shape and will be referred to as the cross-over point. Figure 4.12 shows the scatter plots between the RMSDs and the heart rate together with the fitted functions. The change in the shape of individual CRFs occurs at approximately 68 bpm. Below this point, the transfer function that mediates the interaction between HR and the BOLD signal can be better characterized by a CRF similar to $CRF_{g_{SHR}}$, while above 68 bpm, the $CRF_{g_{FHR}}$ seems adequate for modeling HR variations.

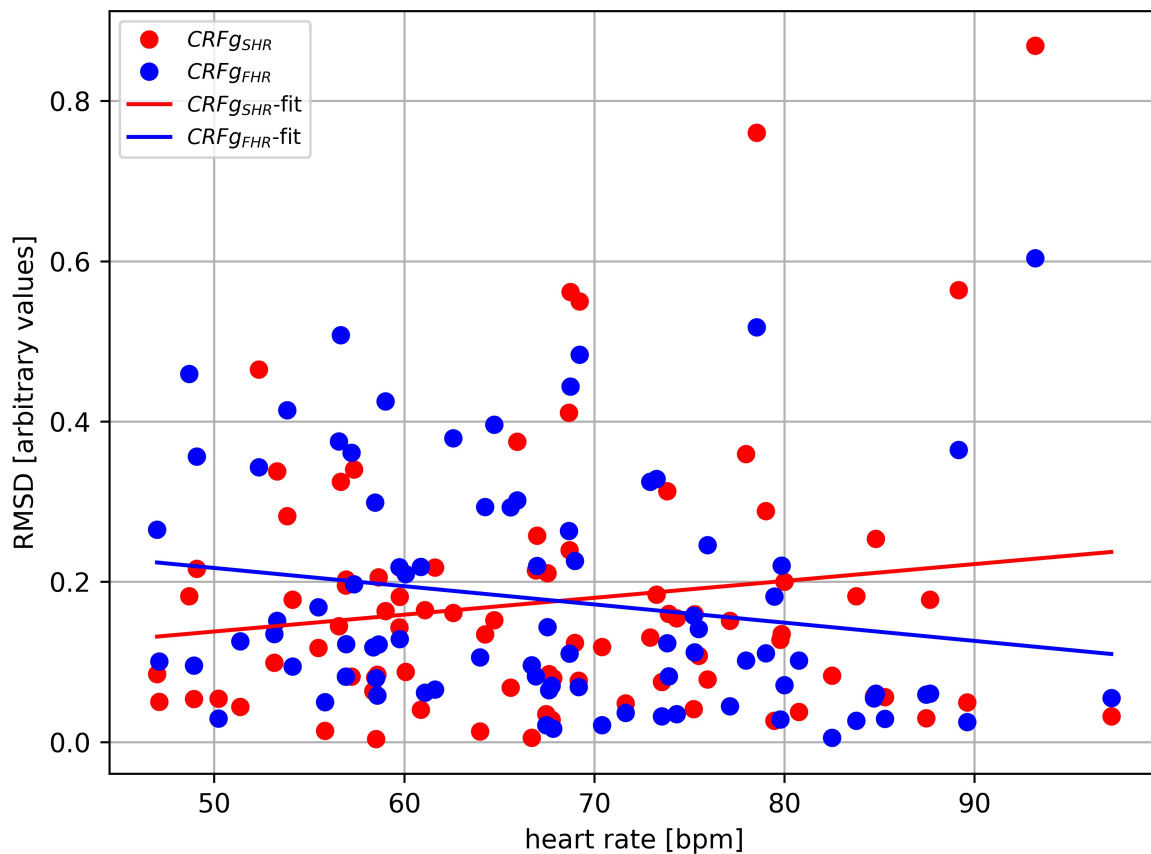


Figure 4.12: RMSD between individual CRFs and CRF_g of fast (points blue) and slow heart rate (points red) groups. The data were fitted with straight lines. The point at which both fitted function cross (68 bpm) is the point where the CRF changes from a single- to a double-peak shape.

Furthermore, K-means clustering was applied to quantify the number of subjects that were misclassified by the RMSD approach. In the SHR group, 27% of subjects were misclassified by the $CRF_{g_{SHR}}$, while in the FHR group, 24% were misclassified using the $CRF_{g_{FHR}}$. Unsurprisingly, around half of the misclassified subjects in the SHR group were situated in the

transition zone between 65-70 bpm. This result is in line with the finding that individual CRF outperforms the CRFg method in the MHR group in terms of the percentage of brain voxels with significant R^2 (see Table 4.2).

The change in the shape of the CRF can be seen in Figure 4.13. Individual CRFs are depicted over a broad range of HRs to illustrate the stability of the CRF shape better. These CRFs showed stable behavior up to 67 bpm with forms roughly comparable to that of the CRFg_{SHR}. Above 67 bpm and up to 97 bpm, the CRF shape is also stable and is characterized by a second maximum and an earlier dip compared to the CRF describing subjects with HR below 67 bpm.

CRF shape across different heart rates [beats/minute]

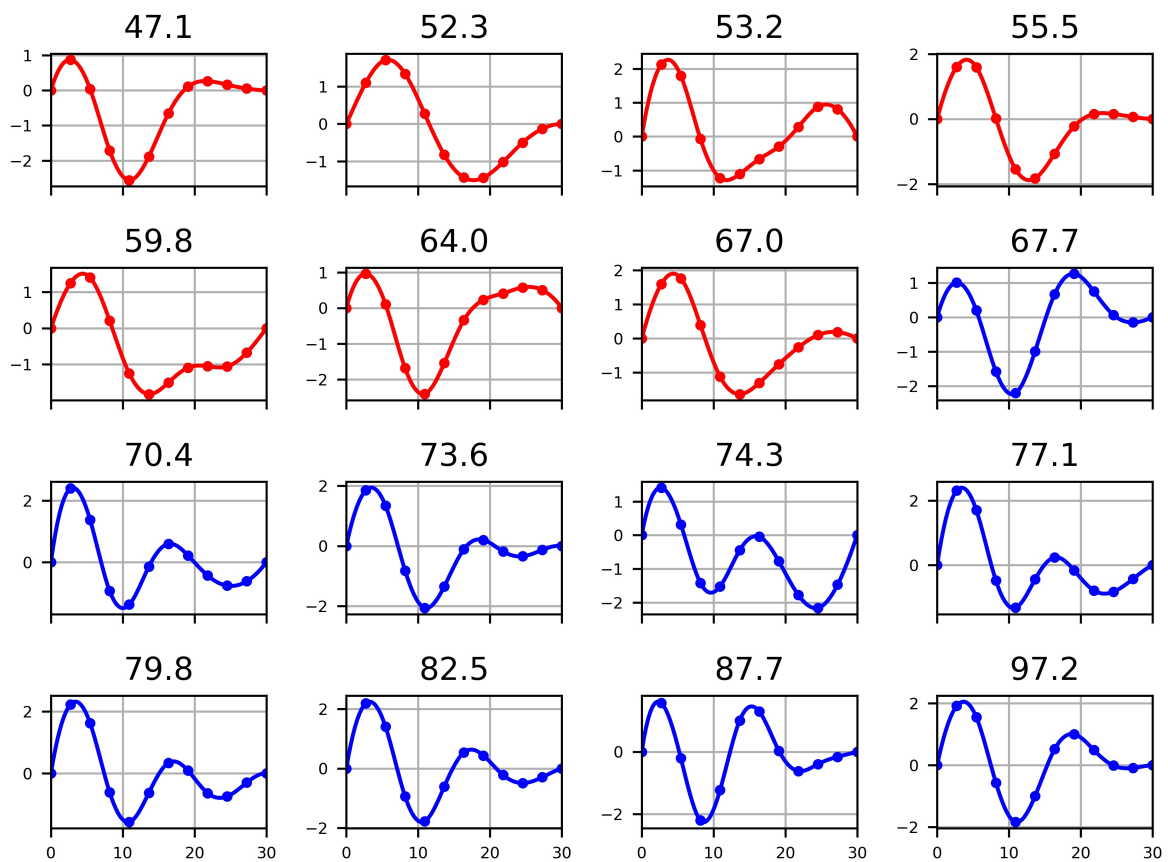


Figure 4.13: Individual CRF across subjects with different heart rates. The CRF of subjects with heart rates below 67 bpm (red curves) has a shape resembling that of the CRFg_{SHR}. Above 67 bpm (blue curves), the shape of the CRF exhibits two well-defined maxima similar to the CRFg_{FHR}.

4.3.3 Introduction of the heart rate based CRF (CRF_{HR})

As pointed out in the previous section, individuals can be separated into two HR groups according to the shape of the CRF. By doing so, one can average all individual CRFs in each of these

4.3 Heart rate and cardiac response function

groups to generate a new CRF, i.e one for slow HR called $\text{CRF}_{\text{HR-slow}}$ and one for fast HR called $\text{CRF}_{\text{HR-fast}}$. These functions will be referred to as *HR-based* CRFs to differentiate them from the group-specific CRFs. HR-based CRFs can be thought of as optimized CRFs that explicitly account for the dependence of the CRF shape on HR. Both functions were parameterized as the sum of a Gamma and a Gaussian function plus a derivative term, as shown in Equation 4.1 [64]. The incorporation of a derivative term allows capturing the features of HR-based CRFs such as the second peak in the $\text{CRF}_{\text{HR-fast}}$ more precisely. The coefficients of the fit are listed in Table 4.3.

$$h(t) = h^0(t) + \alpha \frac{d}{dt} h^0(t) \quad \text{where} \quad h^0(t) = a_1 t^{a_2} e^{-\frac{t}{a_3}} - a_4 e^{-\frac{1}{a_5}(t-a_6)^2} \quad (4.1)$$

Table 4.3: Fit coefficients obtained from the parameterization of HR-based CRFs. $\text{CRF}_{\text{HR-slow}}$ is the HR-based CRF of the slow HR group (<68 bpm); $\text{CRF}_{\text{HR-fast}}$ is the HR-based CRF of the fast HR group (>68 bpm).

	$\mathbf{a_1}$	$\mathbf{a_2}$	$\mathbf{a_3}$	$\mathbf{a_4}$	$\mathbf{a_5}$	$\mathbf{a_6}$	α
$\text{CRF}_{\text{HR-slow}}$	0.18	2.1	3.69	2.35	29.84	11.97	2.52
$\text{CRF}_{\text{HR-fast}}$	0.01	2.47	3.5	0.17	21.9	12.55	39.58

This study recommends the use of $\text{CRF}_{\text{HR-slow/fast}}$ to model HR-induced fluctuations in the BOLD signal more accurately. Based on the subject's mean HR, one can choose the corresponding CRF_{HR} and remove HR-related noise. Figure 4.14 summarizes the HR-based CRF model.

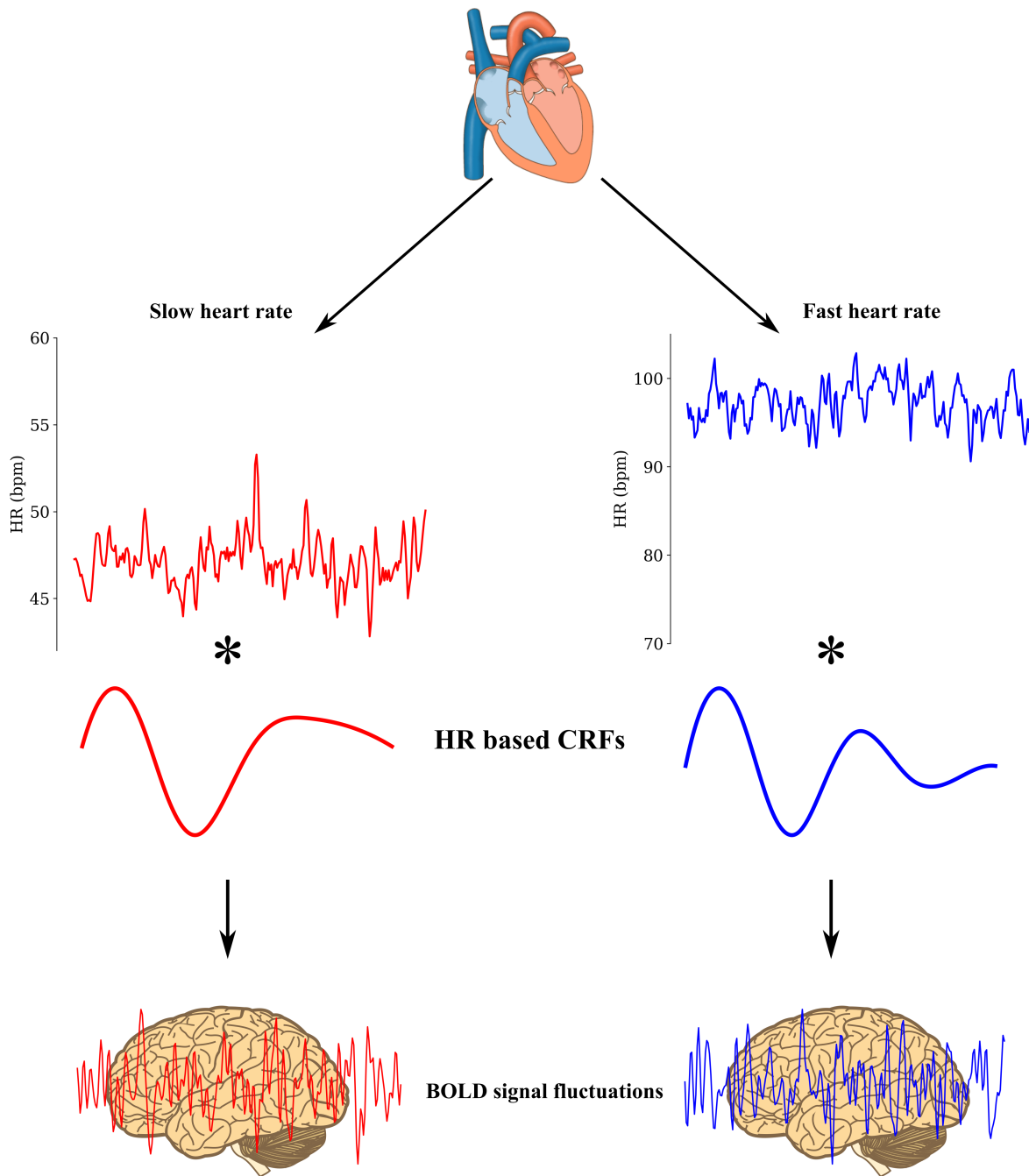


Figure 4.14: Illustration of the HR-based CRF model. Different heart rates cause hemodynamic responses, which are represented by HR-based CRFs, resulting in different BOLD signal fluctuations. The HR-based CRF for slow heart rates (< 68 bpm) is smooth with a well-defined maximum (depicted in red), while the HR-based CRF for fast heart rates (> 68 bpm) presents two maxima (depicted in blue). Mathematically, BOLD signal fluctuations are represented by the convolution of the heart rate regressor with the HR-based CRF. The symbol * indicates the “convolution” operator.

4.4 HR-based CRF derived from grey matter or cerebrospinal fluid

In this section, the hypothesis that HR-based CRFs derived above ($CRF_{HR-slow}$ and $CRF_{HR-fast}$) are not (or only slightly) influenced by fluctuations of neural origin was tested. It is known that a correct estimation of CRF relies on the quality of the recorded cardiac signal and the presence of HR-related low-frequency fluctuations in the BOLD signal. Regarding the latter, neural activity occurring approximately at the frequencies of HR variations may indirectly influence the shape of the CRF. Therefore, HR-based CRFs need to be further examined in the absence of neural activity.

For this analysis, the sample was divided into two groups according to the HR cross-over value of 68 bpm. HR-based CRFs were derived from gray matter (GM), and cerebrospinal fluid (CSF) tissues for comparison. The BOLD signal of GM contains contributions from all cardiac-related noise components, but also the neural signal. On the other hand, the BOLD signal from CSF is dominated by physiological artifacts and does not contain a neural signature.

Figure 4.15 shows $CRF_{HR-slow}$ and $CRF_{HR-fast}$ in both tissues as well as the canonical CRF. Apart from some differences in the amplitude, HR-based CRFs in GM were comparable to those extracted from CSF. Interestingly, the latter were delayed by about 1-2 s relative to the GM. This effect led to an approximation of the main features of the $CRF_{HR-slow}$ to the canonical CRF in CSF, i.e. time-to-peak and time-to-dip. Overall, the $CRF_{HR-fast}$ still presented its two maxima regardless of the tissue of reference, suggesting that cardiac-related artifacts mainly explain the presence of the second maximum in this function.

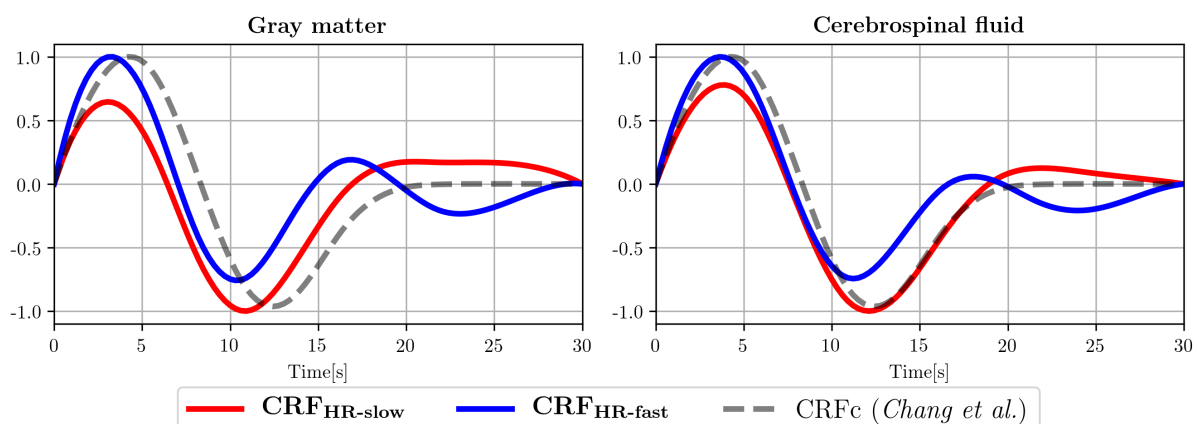


Figure 4.15: HR-based CRFs extracted from gray matter and cerebrospinal fluid. CRFs are interpolated and normalized between -1 and +1 for illustration.

Abbreviations: $CRF_{HR-slow}$, HR-based CRF of the slow heart rate group (<68 bpm); $CRF_{HR-fast}$, HR-based CRF of the fast heart rate group (>68 bpm); CRF_c , canonical CRF.

4.5 HR-based CRF for physiological noise correction

After establishing the HR-based CRFs and confirming that they are not heavily influenced by neural activity, the ability of HR-based CRFs to efficiently reduce spurious correlations was examined. To accomplish this, $CRF_{HR-slow/fast}$ were used in a framework for physiological noise correction in the default mode network (DMN) connectivity, which is active during the resting-state condition and prone to physiological noise. For comparison, the same procedure was performed using the CRFc.

For this analysis, the entire study cohort was separated into two groups based on the HR cross-over value of 68 bpm, and each HR regressor convolved with its corresponding HR-based CRF, i.e. $CRF_{HR-slow}$ or $CRF_{HR-fast}$. A reduction in functional connectivity occurred in all subjects with both correction methods. The amount of percentage reduction was variable, as shown by the relatively large standard deviation in Table 4.4. Reductions were mostly localized in areas highly susceptible to cardiac noise, such as the occipital sinus or the ventricles. The HR-based CRF model achieved a significantly greater reduction ($p < 0.005$) in functional connectivity compared to the canonical one. Based on this result, the HR-based CRF model seems to be a suitable method for physiological noise correction in the resting-state condition.

Table 4.4: Average percentage reduction of voxels showing significant (voxel-level: $p < 0.001$ uncorrected) functional connectivity to PCC using different correction methods (CRFc and HR-based CRF) compared to no correction.

	CRFc	HR-based CRF	<i>p</i> -value (HR-based vs. CRFc)
All subjects (84)	-5.2 ± 2.4	-6.8 ± 3.9	0.005

4.6 Association of functional connectivity in the CAN with heart rate

Finally, the hypothesis that removal of physiological noise modeled by HR-based CRFs does not weaken known associations between HR and functional connectivity (FC) in the central autonomic network (CAN) in subjects with different HRs was tested. This analysis was accomplished by examining the association of the amygdala connectivity and HR during the resting-state condition. The amygdala is part of the CAN, and its activity changes in concert with cardiovascular responses.

4.6 Association of functional connectivity in the CAN with heart rate

For this analysis, the entire dataset was divided again into two groups according to the HR cross-over value of 68 bpm. FC of the right amygdala (seed) was computed without and with physiological noise correction using HR-based CRFs. In addition, the latter procedure was also applied to an independent study group (18 subjects) to test the reproducibility of the association of amygdala connectivity and HR in a rather small sample. Here, two groups were similarly created according to the HR (slow HR: 52.20 ± 4.41 bpm, 9 subjects; fast HR: 80.14 ± 8.14 bpm, 9 subjects).

The top row of Figure 4.16 shows brain regions with significant FC differences between the slow and fast HR groups when no physiological noise correction is applied. Significant connectivity differences were mainly observed in the anterior and posterior insula, left ventrolateral prefrontal cortex (VLPFC), anterior cingulate cortex, and the dorsal vagal complex (DVC). The same regions were found using HR-based CRFs for physiological noise correction (middle row of Figure 4.16). FC values were essentially not affected by HR-based CRFs, as shown in the bar plots on the left side of Figure 4.16. Using HR-based CRFs led to an increase in the size of most clusters. For example, the cluster comprising the insula increased in size by 26% (see Table 4.5 for details).

The results of the replication sample are depicted in the bottom row of Figure 4.16. Comparable results in FC differences were observed after physiological noise correction using HR-based CRFs. Even in this small sample, it is possible to find an HR dependence of FC between key autonomic regions, such as the amygdala and the insula.

Functional connectivity differences between slow and fast HR groups for seed right amygdala

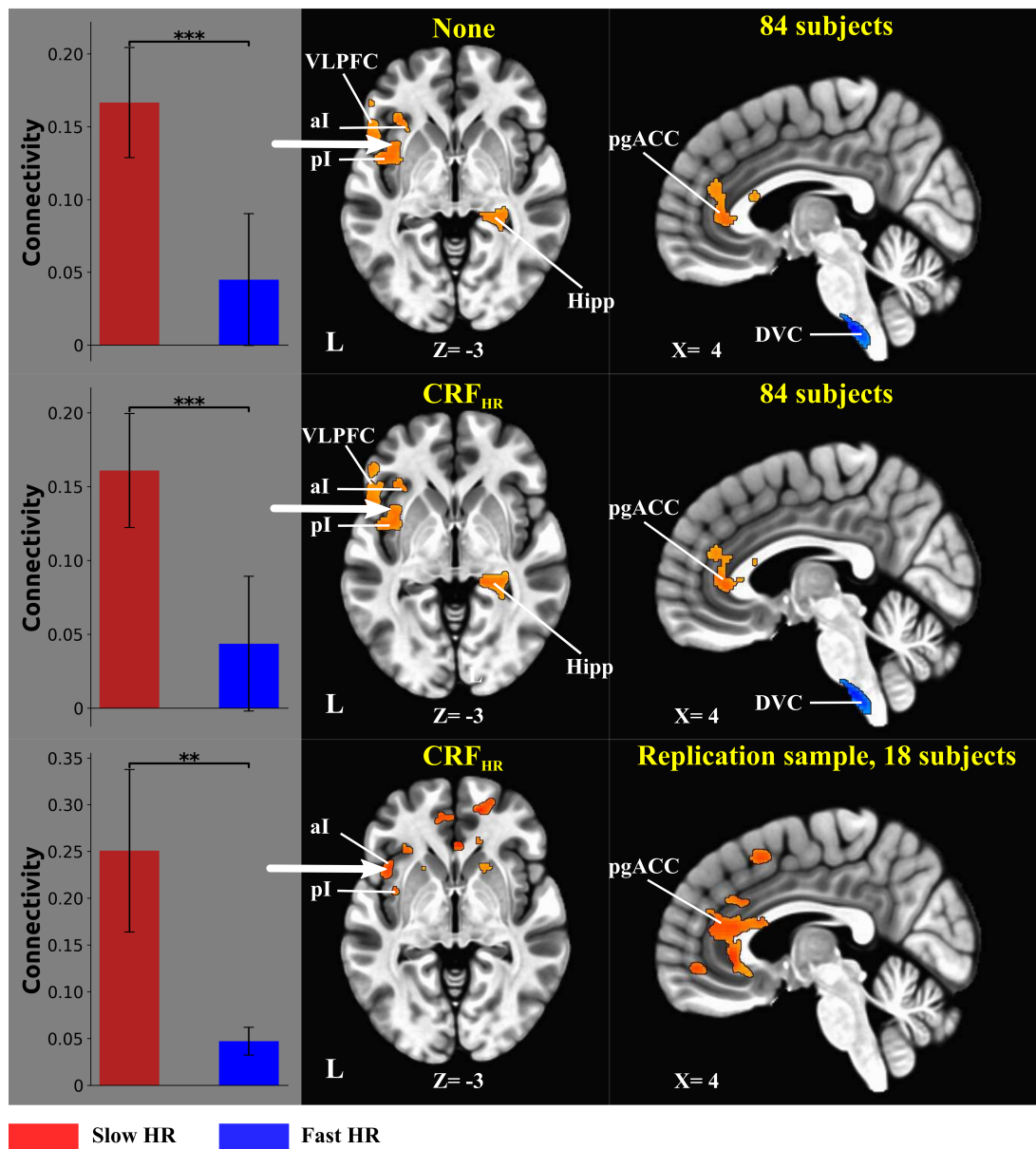


Figure 4.16: Brain regions showing significant differences in functional connectivity between slow and fast HR using the right amygdala as seed region. The top row shows between-group functional connectivity differences when no physiological noise correction is applied (voxel-level: $p < 0.005$, cluster-level: $p < 0.05$ corrected). The middle row shows between-group functional connectivity differences after removing the physiological noise explained by HR-based CRFs (voxel-level: $p < 0.005$, cluster-level: $p < 0.05$ corrected). The bottom row shows between-group functional connectivity differences in the replication sample after removing the physiological noise explained by HR-based CRFs (voxel-level: $p < 0.005$). Bars depicted on the left side represent post-hoc t-tests on connectivity values extracted from the largest cluster in the insula.

Abbreviations: CRF_{HR}, HR-based CRF; *** $p < 0.001$; ** $p < 0.01$; VLPFC, ventrolateral prefrontal cortex; aI, anterior insula; pI, posterior insula; Hipp, hippocampus; pgACC, pregenual anterior cingulate cortex; DVC, dorsal vagal complex.

4.6 Association of functional connectivity in the CAN with heart rate

Table 4.5: Brain regions showing significant functional connectivity differences to the right amygdala between the slow and fast HR groups in the large cohort (n=84).

Functional Connectivity to:	Right/Left	Brodmann's Area	Cluster size*		MNI coordinate			t-value
			None	CRF _{HR}	X	Y	Z	
Seed: Right Amydala								
Insula	L	13	958	1211	-40	4	-3	3.86
Ventrolateral Prefrontal Cortex	L	44/45/47			-50	30	0	4.7
Hippocampus	R	35	450	535	16	-28	-10	5.02
Anterior Cingulate Cortex		32/34	416	445	0	40	10	3.93
Dorsal Vagal Center			474	514	0	-36	-59	-4.61
Premotor Cortex	R	6	488	405	44	-4	38	-5.03

* voxel level $p < 0.005$ uncorrected, cluster level $p < 0.05$ corrected
None refers to no physiological noise correction
CRF_{HR} refers to physiological noise correction using HR-based CRFs

In order to illustrate the relationship between FC and HR more closely, FC values were extracted from the insula cluster in the large dataset (n=84) after physiological noise correction and entered into a regression model with HR. As shown in Figure 4.17, the right amygdala-left anterior insula connectivity significantly correlated with HR ($r = -0.73$, $p < 0.001$) in the slow HR group, while this correlation was close to zero in the fast HR group. For the entire dataset, a nonlinear exponential function adequately describes FC as a function of HR. This curve summarizes the above findings of stronger connectivity for slower HR and smaller connectivity for faster HR.

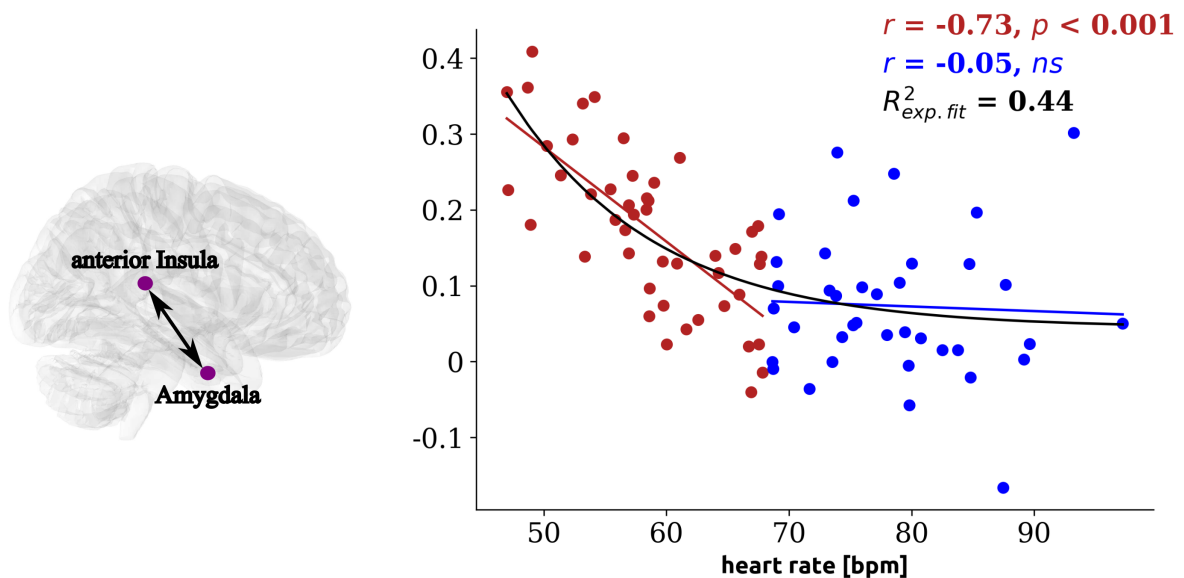


Figure 4.17: Association between right amygdala - left anterior insula connectivity and heart rate. Red and blue points represent subjects in the slow and fast heart rate group, respectively. The entire dataset was fit with the exponential curve in black color. For more plots of this kind, I refer the reader to my recent paper: de la Cruz *et al.* [70]

4.6.1 Effects of simulated aliasing on functional connectivity

As indicated in section 2.6, aliasing is a potential confounding factor that could cause HR-related between-group differences in FC. Aliasing shares frequencies with BOLD signal fluctuations of interest and cannot be removed with conventional methods. Thus, a simulation was performed to examine the effect of aliasing on FC patterns across different HRs and sampling rates (TR).

FC values varied considerably for TR = 2.52 s without any apparent relation to HR, as shown in the scatter plot in Figure 4.18. Neither linear nor exponential functions fitted the data adequately. For TR = 0.72 s, the variability in FC values was smaller than for TR = 2.52 s, but again showing no HR dependence. At this short TR, the aliased cardiac signal tends to reduce the FC, as can be seen in the histogram on the right side of Figure 4.18, which is skewed towards FC lower than 0.3. It should be noted that an HR higher than the sampling rate does not necessarily imply that its fundamental frequency aliases into the investigated resting-state low-frequency range (0.01-0.1 Hz). This is the reason why some HRs at TR 2.52 s and 0.72 s show FC very close to the original value of 0.3. Finally, as expected in the absence of aliasing, i.e. TR = 0.1 s, FC remained stable over the entire HR range corresponding to the correlation of 0.3, and deviations were only due to the added Gaussian noise. Based on these findings, cardiac aliasing does not seem to be the leading cause of the nonlinear relationship found between HR and FC (see Figure 4.17).

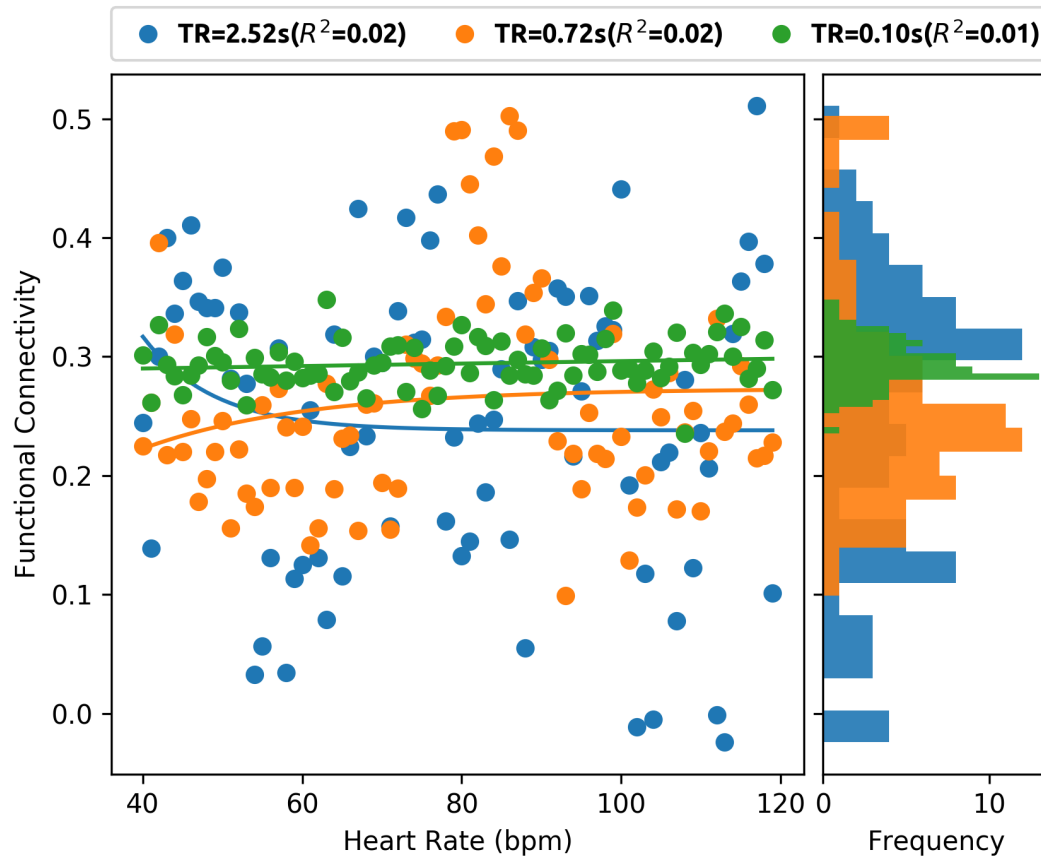


Figure 4.18: Effect of simulated cardiac aliasing on functional connectivity for a wide range of heart rates and different sampling rates (TR). R^2 values in parentheses indicate the variance explained by the exponential function used to describe the functional connectivity as a function of heart rate. The side plot shows functional connectivity histograms at the respective TR.

5 Discussion

Using a large cohort of healthy individuals with different HRs allowed us to demonstrate that HR plays an essential role in shaping the BOLD signal and the cardiac response function (CRF).

Spectral analysis showed that different HRs influence the BOLD signals and their corresponding spectra differently. This relation is captured by the transfer function commonly called the CRF, which depicts the interaction between changes in HR and the BOLD signal. Consequently, it is not accurate to model HR variations in individuals with different HR by using a single canonical CRF, as usually done in the literature. Although individual CRFs can capture more variance in the BOLD signal than the canonical CRF, the results of this thesis suggest that there is no need for such a time-consuming estimation of individual CRFs, as these functions have a similar shape over a wide range of HRs. The two HR-based CRFs introduced in the present work, i.e. $CRF_{HR\text{-slow}}$ and $CRF_{HR\text{-fast}}$, can be directly applied according to the HR of the subject, thus facilitating the analysis of BOLD data.

Moreover, using HR-based CRFs reduces spurious correlations in the “default mode” connectivity more efficiently than applying the traditional canonical CRF. Similarly, HR-based CRFs enhance the spatial extent of clusters showing between-group differences in CAN connectivity by removing variance that obscures the underlying neural activity.

5.1 Heart rate and BOLD spectra

In agreement with the hypothesis that HR and BOLD signals spectra are associated, spectral analysis revealed that the power in the low-frequency band of HR variability (0-0.2 Hz) correlates positively ($r = 0.26$, $p < 0.05$) with the power of the whole-brain global signal (0.01-0.2 Hz). This finding is consistent with another report in which low-frequency fluctuations of less than 0.1 Hz in HR showed a high degree of temporal correlation with hemodynamic variables such as oxy-hemoglobin concentration [135]. Furthermore, the strong correlation of HR with the alpha

rhythm [72, 71], an *EEG* index of resting-state neural activity, supports the association between HR and BOLD power spectra.

During the spectral analysis, frequencies in the BOLD signal below 0.01 Hz were ignored, as they are mainly caused by scanner instabilities [225]. These ultra-low oscillations have been observed in cadavers [225] and phantoms [156], providing evidence for a non-physiological origin. The removal of the <0.01 Hz frequencies has become a standard step in resting-state fMRI preprocessing.

Accumulating evidence suggests that HR variations manifest themselves in resting-state BOLD signals through blood pressure changes [135, 173]. The role of the heart as the principal cardiovascular controller and of its inherent ability to generate blood pressure oscillations is supported by the fact that resting HR correlates with mean arterial blood pressure [132, 188, 189]. Nevertheless, the correlation observed in this study between power spectra densities may arise indirectly from correlations between respiration and HR. It is well known that respiration modulates the beat-to-beat distance via the respiratory sinus arrhythmia (RSA) mechanism. RSA was significantly different between the HR groups (see Table 4.1) and can thus be considered a possible influential factor. However, RSA did not significantly ($p > 0.27$) explain the correlation between HR and BOLD power spectra, as revealed in a separate analysis using multiple linear regression.

One should also consider the possibility of neuronal mediation. For example, changes in the arousal state can simultaneously trigger changes in HR and global neural activity. However, arousal, as assessed by skin conductance response indices (spontaneous fluctuations and level), did not differ among the groups and was thus discarded as a possible source conditioning the relation between HR and BOLD power spectra. In the same line of thought, it is reasonable to assume the presence of one or more brain regions that generate slow oscillations of neural activity that directly modulate HR [238] and are simultaneously accompanied by hemodynamic fluctuations [195]. Indeed, the existence of a “central pacemaker,” which regulates HR, has been recently identified in cingulate regions [195]. However, this possibility should be interpreted with caution since a significant correlation ($r = 0.29$, $p < 0.005$) between power spectral densities was also observed in CSF tissue, which does not contain neural activity.

Undersampled physiological signals can also contribute to changes in the BOLD spectrum through aliasing [31, 155]. However, it is challenging to accurately quantify the aliasing contribution since the low sampling rate ($TR = 2.5$ s) used in this study allowed all fundamental cardiac frequencies and higher-order harmonics to alias into the BOLD signal. Thus, one cannot exclude the possibility that the amount of aliasing affecting the BOLD spectra might have been proportional to HR, i.e. the faster the HR, the higher the aliasing into the BOLD signal,

and, hence, driving the correlation between HR and BOLD power spectra. Further studies are required to clarify the consistency and reproducibility of this relationship in the presence of higher sampling rates.

All heart rate spectra and the BOLD spectrum from the fast HR group displayed a peak at ~ 0.1 Hz. This rhythm, commonly known as Mayer or M-waves [165], is characteristic of the human arterial blood pressure and HR, but has also been reported in the brain in the form of hemodynamic and neural oscillations [204, 212, 249, 194]. The 0.1 Hz peak resides in a frequency range that is thought to be mediated by both the sympathetic and parasympathetic systems [205]. The amplitude of the 0.1 Hz peak in the HR spectra seems to be proportional to HR, i.e. the fast HR group showed the highest amplitude at 0.1 Hz, while the slow HR group showed the lowest (see Figure 4.2). In addition, the amplitude of this peak is commonly related to a resonance effect created by respiration [148]. When breathing slows down to the frequency of the baroreflex feedback loop, it creates resonance, a nonlinear effect that is greater than the additive effect of both breathing and baroreflex influences, and causes a pronounced high-amplitude peak in the HR power spectrum at ~ 0.1 Hz [164]. However, in this study, resonance cannot explain the varying amplitude of the 0.1 Hz peak since the measured respiratory rates are above the 6 breaths/minute required to create resonance.

Taken all together, HR is an essential factor that should always be considered when interpreting fMRI data. The forward relationship driven by HR ($\Delta\text{HR} \rightarrow \Delta\text{BOLD}$) constitutes clear evidence of how peripheral signals influence central ones. This influence can be crucial when examining changes in brain activation with fMRI using a task or an intervention that elicits cardiovascular reactions. Transient changes in HR most probably corrupt the recorded BOLD signal and might be interpreted as neural activation. Awareness of physiological noise in fMRI has increased over the years, yet it is still not a routine to record physiological signals during the scans. Although the underlying mechanisms of the coupling of HR and BOLD signals remain unclear, the analysis of BOLD data without consideration of HR is incomplete and can lead to misinterpretations.

5.2 HR-based CRF

To model low-frequency cardiac influences on the BOLD signal, Chang and colleagues introduced a canonical CRF that was derived from only three subjects. Although questioned by some authors [64, 81, 137], this function has been widely used in modern neuroscientific research (e.g. [42, 54, 134] among others). The most notable limitation of a generalized function is its inability to account for possible intra-subject variations in physiological response triggered by

the unique biological characteristics of each individual [81]. Therefore, optimizing the shape of the CRF based on each subject's data could accommodate an individual's variation. Indeed, analyzing single-subject data has become more desirable for fMRI researchers interested in comparing individual results [137]. A recent study examining the effect of physiological noise correction on FC in pharmacological data revealed that the canonical CRF negatively impacted FC in regions of interest for the experiment and increased false positives. Therefore, these observations raise concerns about the use of canonical response functions in pharmacological studies [137].

This thesis shows that different HRs influence the BOLD signal differently so that different CRFs are necessary to model HR-induced fluctuations more accurately. Individual CRFs accounted for more variance in the BOLD signal than the canonical CRF, as observed in subjects from the medium and fast HR groups (see Table 4.2 for details) and previous studies [64, 81]. However, the use of an individualized approach may not always lead to satisfactory results, especially when physiological recordings contain a significant portion of noise. Indeed, averaging individual CRFs within a specific HR range was more effective than the individualized approach, as shown by the higher fraction of brain voxels with significant variance using group-specific CRFs (see Table 4.2). One possible reason for this finding is the influence of a noisy physiological signal (e.g. due to subject movement or bad sensor position) in the deconvolution process, where averaging across subjects may help to minimize such undesired effects.

At the subject level, there were some individuals in whom the canonical CRF outperformed individual and group-specific CRFs in terms of percentage of brain voxels with significant variance (see Table A.1 in Appendix A.2). It is difficult to provide a definite explanation for this finding since the exact shape of the CRF is unknown, but it may be attributed to a reduced portion of physiological noise in the whole-brain global signal of these subjects. Another possible explanation is that the canonical CRF coincidentally matched the BOLD signal fluctuations better than the other CRFs. At the same time, the fact that this unexpected result mainly occurred with subjects from the slow HR group supports the notion that the canonical CRF is an appropriate function for samples with slow HRs.

A HR cross-over value was found at approximately 68 bpm, at which CRF changes from a single- to a double-peak shape, using the root-mean-square deviation (RMSD) index. Likewise, plotting individual CRFs over different HRs (see Figure 4.13) showed that the data could be separated into two groups using this HR cross-over value. The two groups were used to derive two new CRFs, called *HR-based* CRFs. However, one should be cautious in taking the 68 bpm as a definite HR cross-over value. For example, the K-means clustering algorithm revealed that there were misclassified subjects using the RMSD index. The majority of them were subjects with HRs between 65-70 bpm. Hence, it is more appropriate to say that there is a transition range

instead of a single cross-over point, at which the CRF changes its shape. This observation may explain why the use of individual CRFs outperformed the group-specific CRFs and the canonical CRF in the medium HR group in terms of percentage of brain voxels with significant variance, and thus, suggest the use of the individualized approach in this HR range.

Individual CRFs from subjects with faster HR (>68 bpm) is characterized by a second maximum, which is not present (or less pronounced) in individuals with slow HR. This second maximum was reported in previous studies investigating CRF but was not explained [64, 81, 98]. The small sample sizes and limited HR range used in those studies did not enable the authors to draw any conclusions about the relationship between CRF shape and HR. Overall, a second maximum has been repeatedly reported at 19 s [81] and 18 s [64, 98], which corresponds to the second maximum at 17 s of the CRF_{HR-fast}. The presence of a second maximum has also been observed in the hemodynamic response function of certain brain regions, but no consensus exists regarding the mechanism leading to its formation [92, 172, 175, 240]. In summary, it can be concluded that the second maximum of the CRF is characteristic of subjects with faster HR and possibly “captures” the 0.1 Hz peak simultaneously present in the HR and BOLD spectra of these subjects.

The scanning time can also influence the shape of the CRF [81]. Although the scan duration in the present work was sufficiently long to provide a reliable estimation of the CRF, the interaction between physiological processes and the BOLD response might be non-stationary [177]. In this context, a window approach, similar to that used for dynamic functional connectivity [125], could provide more detail about the interaction of HR with the BOLD signal.

In the present study, the derivation of individual CRF was performed using the physiological noise information embedded in the whole-brain global signal (GS). The GS contains not only physiological noise but also relevant neural information and non-physiological noise, such as thermal and system noise [173, 216]. Nonetheless, the strong correlation found in previous studies between GS and physiological variables, e.g. PETCO₂ [253], suggests dominant physiological noise contribution to the GS. It is also noteworthy to mention that GS could be influenced by other brain regions and tissues [81], each showing different CRF. Indeed, this study found slight inter-regional differences in the shape of average CRFs, but, in general, the features of each regional average CRF, such as the number of maxima and time-to-peak, remained unchanged as compared to the whole-brain (see Figure 4.9).

Furthermore, a reduced model was used to deconvolve the CRF, which does not take into account respiration. To reduce the influence of respiration on HR, a set of regressors was created using the RETROICOR algorithm and the RVT signal together with its lagged terms. These regressors were removed from the BOLD signal using linear regression but not orthogonalized

with respect to HR. The rationale was to keep the HR signal unaffected by this step. This means that dependencies between regressors are possible, which may influence the estimation of the CRF. However, since no significant differences ($p > 0.37$) were observed among HR groups regarding the respiratory rate, the influence of respiration on the CRF estimation was considered negligible. Nevertheless, the possibility that respiration may influence the shape of the CRF was considered. In a separate analysis, cardiac and respiratory response functions were simultaneously deconvolved using the full model (Equation 2.12). The outcome was that the inclusion of the respiratory term yielded minimal differences in the CRF relative to the reduced model, thus supporting the initial assumption that accounting for respiration has only minimal effects on the estimation of the CRF. However, in samples with significantly varying respiratory rate, it is advisable to also account for the effects of respiration and to perform the deconvolution simultaneously for HR and respiration.

In summary, HR-based CRFs can be thought of as optimized cardiac hemodynamic response functions. They efficiently account for the dependence of hemodynamic changes on HR variations. HR-based CRFs embrace the most relevant features of canonical and individual models; that is, they are global but still preserve the inter-subject variability. Using this approach, researchers interested in removing the influence of HR variations on the BOLD signal need only to know the mean HR of an individual and choose the corresponding HR-based CRF (see Table 4.3 for parameterization coefficients and Figure 4.14 for a summary).

5.3 HR-based CRF in grey matter or cerebrospinal fluid

The main idea underlying this thesis is that CRF primarily captures non-neural sources. This implies that differences in HR-based CRFs are also visible in brain regions containing or not neural signatures. Thus, CRFs were derived from gray matter (GM) and cerebrospinal fluid (CSF) in the same way as done for the whole-brain. This analysis revealed that between-group differences in the shape of HR-based CRFs remained in both brain tissues, confirming the hypothesis that the neural signal has little impact on the CRF.

Despite this finding, some issues deserve further attention. For example, variability in amplitude and shape of HR-based CRFs were observed when comparing both tissue signals. Compared to GM, HR-based CRFs derived from CSF were delayed approximately by 1 s in the overshoot as well as by 2 s in the undershoot and second maximum. This result is somewhat unexpected because GM has a high vascular density. In particular, the larger vessels in GM have a long delay in their hemodynamic stimulus response due to a prolonged blood flow transit time [147].

One possible explanation is that the CSF mask is contaminated by partial volume effect (PVE) with GM. Tissue masks were obtained from T_1 -weighted images, which have an adequate contrast for tissue segmentation. However, the spatial transformation from T_1 to functional data resolution leads inevitably to tissue deformation and hence to overlaps with large vessels. Besides, the CSF mask is smaller than the GM mask, implying that PVE effects are more noticeable. Even though large vessels are also part of the GM, their impact is diminished when including a higher number of brain voxels [81].

5.4 HR-based CRF as a physiological noise correction method

The main challenge in the analyses of resting-state data, or functional connectivity, is the separation of the neuronally-induced BOLD signal changes from the many other sources of noise. The present study presents a new approach, HR-based CRF, aimed to reduce HR variations of non-neuronal origin. The performance of the HR-based CRF as a possible method to “clean” the rs-fMRI data was compared with the canonical CRF on the “default mode network” connectivity. HR-based CRFs led to a significantly stronger reduction ($p < 0.005$) in FC in comparison to the canonical CRF, therefore qualifying as a potential noise correction method.

The default mode network (DMN) is highly active during resting state, and thus a good target for physiological noise correction [47, 105]. In contrast to other large-scale brain networks, DMN is activated during internally-oriented tasks, while deactivated during externally-oriented cognitive processing. Physiological noise, particularly HR variations, is problematic for the interpretation of the BOLD signal in the DMN. Some authors have even suggested that DMN may not be of neural origin but rather a result of changes in cardiac or hemodynamic processes [7, 129, 241]. These particularities make the DMN the preferred network for assessing the effectiveness of physiological noise correction methods [53, 228, 245].

However, one should recall that it is difficult and open to debate to determine whether the correlations removed are actually of non-neural origin [7, 127]. For example, the HR variations removed by HR-based CRFs can be driven by neuronal activity. This hypothesis is plausible, given that the interaction between the brain and the heart is bidirectional [7, 151, 238, 237]. It is well documented that cortical and subcortical regions are constantly monitoring and regulating autonomic functions such as HR [20, 238, 237]. In this context, HR can be seen as a carrier of meaningful physiological information, and its removal from the BOLD signal also implies the removal of the variance of interest [72, 71].

5.5 HR-based CRF and the central autonomic network

The central autonomic network (CAN), particularly the amygdala, prefrontal cortex, and insula, appears to play an essential role in regulating the cardiovascular system. Neuroimaging data have shown that activity in these CAN areas and their functional couplings change in concert with HR responses [67, 182, 197, 209, 128, 236]. As hypothesized, HR-based CRF did not weaken the association between HR and functional connectivity of regions involved in autonomic control. More specifically, the significant FC differences observed between slow (< 68 bpm) and fast HR (> 68 bpm) groups in the CAN areas remained despite the removal of HR-induced fluctuations via HR-based CRFs.

Physiological noise correction enhanced the spatial extent of clusters showing between-group differences in CAN connectivity. This suggests that non-neuronal cardiac processes introduce global variance that obscures the underlying autonomic neural activity, and illustrates the efficacy of HR-based CRFs to remove such noise. Moreover, HR-based CRFs did not significantly reduce the mean correlation coefficients in clusters, as found in a separate post hoc analysis. This non-influence on the correlation coefficients can be deduced from the top and middle bar plots in Figure 4.16, illustrating the amygdala-insula connectivity.

Significant functional connectivity differences were observed between the right amygdala and other autonomic regions in relation to HR with or without physiological noise correction. This HR-FC association was partially replicated in a sample of 18 subjects after applying physiological noise correction. However, given the small size of this sample, it was not possible to correct the statistical map for multiple comparisons, as clusters did not reach the critical size to pass the cluster-level corrected statistical threshold. Similarly, no comparison between samples, i.e. main sample vs. replication sample, was performed as they had unbalanced sizes, which could have biased the statistical analysis [33]. Another argument is that samples were scanned with different MRI parameters that, among other things, alter the physiological contribution and functional connectivity patterns [99].

The association of HR and FC in CAN regions is in line with previous reports using task-based fMRI. For instance, it has been demonstrated that cardiac changes induced by short sessions of physical effort elicit functional connectivity changes in CAN regions [182, 222]. Norton and colleagues reported that during a simple handgrip task, activation in the medial prefrontal cortex and hippocampus was negatively correlated with changes in HR [182]. The relationship between HR and FC also agrees with the model of neurovisceral integration introduced by Thayer and Lane [237, 238]. The model states that a set of neural structures (emphasizing the role of the amygdala and the medial prefrontal cortex) regulates HR in response to external demands.

Subjects with slow HR exhibited significantly increased FC between the right amygdala and all regions except DVC compared to fast HR. Further post hoc analysis using linear regression revealed a strong significant negative correlation ($r = -0.72$, $p < 0.001$) between the right amygdala-insula connectivity and HR in the slow HR group. Across all subjects, the relation of FC and HR could be described by an exponential decay function, i.e. with increasing HRs, the functional coupling in the CAN became lower. One could have used more complex functions to fit the data, e.g. a higher-order polynomial, but this would be less physiologically plausible than an exponential function. There are several physiological processes involving HR that are governed by an exponential-decay. For example, the relationships between HR variability and HR [170] and HR response to short static breath-holding [52] are all approximated by an exponential decay function. Consequently, further investigations are required to understand the nonlinear relationship between FC and HR in healthy subjects and different psychiatric conditions.

One explanation for the observation of stronger FC with slower HRs could be increased parasympathetic activity. For example, slower HR, stronger functional connectivity in CAN regions, and increased parasympathetic activity have been simultaneously observed during meditation [40, 138, 229, 235]. Hypnosis is a similarly effective method to decrease HR [13, 16], putatively by shifting the sympathovagal balance towards enhanced parasympathetic activity [74]. Hypnosis is additionally accompanied by changes in the FC between CAN structures, such as increased FC of ACC with the prefrontal cortex, insula, and brainstem [82]. Although HR was not explicitly manipulated in this thesis, significant FC changes were observed in regions reported in the above studies, which support the interpretation of an association between changes in FC between CAN regions and changes in HR.

Furthermore, a slower HR is also observed in individuals with regular physical activities and is a sign of healthy cardiovascular regulation [35, 215]. However, since no significant differences in the amount of self-rated physical activities were found among groups (see Table 4.1), physical capacity is not a major influencing factor. In the same line, differences in FC could not be explained by different levels of physiological arousal, because the skin conductance parameters indexing this variable [5, 9] did not significantly differ among the groups.

Several further factors can influence functional connectivity at rest [86]. For instance, content and frequency of spontaneous thoughts [61, 101], mood [115], and the kind of task performed before scanning [14, 244] may cause differences in functional connectivity. However, it seems unlikely that these factors cause such widespread and systematic functional connectivity changes [144] as those detected in the present study. Age is another critical factor that might lead to changes in connectivity [141, 209] and HR [36]. Since participants were all young adults

and groups did not differ significantly in age, it is unlikely that the effect of age can explain the observed differences in FC in this study.

Another potentially relevant factor might be the degree of wakefulness in the resting state condition with closed eyes. In a typical resting-state protocol, about one-third of participants cannot maintain wakefulness and fall asleep [232]. This percentage becomes even higher if subjects are instructed to keep their eyes closed [232], as in the present study. The replication sample was scanned with open-eyes, so the effect of sleep as a confounder causing functional connectivity differences can be discarded. The wakefulness-sleep transition is also associated with fMRI signal changes [55, 145, 233, 232] as well as alterations in cardiovascular parameters like blood pressure and HR [226]. As mentioned above, there were no differences in the level of physiological arousal as assessed by skin conductance indices, which may be an indicator of changes in the degree of wakefulness [210].

Aliasing is another way through which physiological noise undermines estimates of brain connectivity. Aliasing may lead to artificial FC differences or spurious correlations in BOLD data. The present study used a TR of 2.52 s. Hence, the possibility that between-group differences in FC are due to different aliasing effects in the groups with slow and fast HR needs to be considered. It was found that aliasing effects caused by the cardiac signal do not represent a major confound for FC when groups significantly differ in HR. As shown in the simulation (Figure 4.18), the FC exhibits a rather chaotic pattern when physiological cardiac noise dominates and not the exponential course observed in real data (Figure 4.17).

Altogether, these results confirm theoretical models of neurovisceral integration and strengthen the use of resting-state BOLD data for studies of brain-heart interactions. The functional coupling between brain regions involved in autonomic control covaries negatively with HR in a nonlinear fashion. Although the underlying physiological mechanisms remain to be elucidated, this finding is remarkable and relevant when examining FC differences in groups with varying HR. For instance, comparing groups not matched in terms of age might lead to spurious FC differences, considering the well-established age-related alterations in brain and heart functions [141, 209]. The nonlinear coupling between FC and HR also raises the question to what extent FC is suited for investigating brain-heart interactions at elevated HR since FC approximates zero when heartbeats are above 68 bpm. Last but not least, HR-based CRFs enhanced between-group statistical comparisons, suggesting their use as a physiological noise correction method in studies investigating neural substrates of cardiac regulation.

5.6 Limitations

Some limitations of the present study should be mentioned. First, no task was conducted to explicitly manipulate the subject's HR. Handgrip exercise [222] or pharmacological stimulation, e.g. isoproterenol infusion [117], are ways to elicit cardiovascular responses in fMRI. These kind of experiments may better characterize the dependence of the cardiac hemodynamic response function on HR at the subject-level since other factors remain constant, e.g. brain vascular density. However, such experiments may also produce large subject's movements obscuring the specific neuronal response. Even more problematic is when the task elicits more than one process, e.g. simultaneously demanding cognitive/mental effort and motor activity, which makes it challenging to disentangle the cardiovascular adjustments evoked by each process. Pharmacological stimulation might overcome some of these limitations. Nonetheless, it can potentially disrupt the neurovascular coupling making results more difficult to interpret [38]. Besides, studies in healthy subjects relying on pharmacological agents that alter HR require approval by the local ethics committee, which might be hard to obtain.

It would also be interesting to investigate HR-based CRFs and HR-related connectivity changes across the life-span or in different neuropsychiatric disorders. As only a healthy young sample was analyzed, it is not possible to comment on the extent to which HR-based CRFs are also applicable to an aging population. It is well-known that with advancing age, structural, functional, and physiological changes occur in the brain and heart, which likely influence the shape of the CRF and FC. Similarly, patients with neuropsychiatric disorders and concurrent cardiovascular alterations are likely to have different CRFs than healthy subjects. Further analyses are required to address these issues using non-healthy subjects and aging populations in order to gain insights on physiological processes that determine the shape of the CRF.

Furthermore, the simulation performed to examine the influence of different TRs and HRs on functional connectivity has some caveats that should be emphasized. One limitation is that it does not explicitly model HRV. HRV comprises frequencies that contribute to the low-frequency fMRI spectrum and thus influence functional connectivity. However, HRV modeling requires variation of the beat-to-beat distances within a range of physiologically plausible values as well as consideration of a wide variety of physiological factors including, among others, respiration, baroreflex, and the autonomic nervous system. These requirements are challenging to meet by simulation, and therefore HRV was not modeled. One further limitation is the assumption of an equal amount of aliasing in both BOLD signals. In real data, for example, the aliasing of cardiac pulsation varies throughout the brain, being particularly noticeable in the brainstem, near the spinal cord, and around larger blood vessels.

Finally, other technical aspects may potentially impact the current findings. Scanner field strength, as well as temporal and spatial image resolution, affect the contribution of physiological noise to the BOLD signal [50, 243, 242]. For example, physiological noise scales with the field strength and can be the dominant source of noise at high MRI field strengths. Similarly, the temporal resolution, i.e. sampling rate, controls the contribution of physiological aliasing, while the voxel size affects the fraction of physiological noise in the time series. All these factors were kept constant in this study. Thus, additional research is required to confirm and replicate the current findings and to determine their generality under different MRI conditions.

6 Conclusions and Outlook

The main goals of this thesis were to investigate how different HRs influence the BOLD signal and to extend current physiological noise correction methods to reduce HR-induced fluctuations more accurately. Both goals were successfully achieved.

First, this study provides clear evidence of a direct association between HR and BOLD signal spectra. In particular, it was shown that different HRs give rise to different profiles of BOLD signal spectra. HR also influences the shape of the cardiac hemodynamic response function (CRF), which models the way the brain responds to HR variations. Fast heartbeats cause a second maximum in the CRF, whereas the CRF of subjects with slower HR is smooth and exhibits a single well-defined maximum. Such particularities in the shape of the CRF enable the separation of individuals into two groups according to their HR [69].

Second, by taking advantage of the observed dependence of the CRF on HR, this thesis introduces a novel method, called *HR-based* CRFs, to model HR-induced fluctuations more accurately than existing methods. These functions explain more variance in the BOLD signal than previous models using canonical or individual CRFs. One immediate application of HR-based CRFs is the generation of regressors, which allow efficient removal of noise in the BOLD signal. Indeed, their performance for physiological noise correction was assessed in the default mode network connectivity, the most widely studied network in resting-state fMRI. Using HR-based CRFs resulted in a more substantial reduction of cardiac noise than the use of the traditional canonical CRF model, suggesting that overestimation of functional connectivity (FC) can be avoided by employing the new functions.

A necessary condition for the use of HR-based CRFs to reduce physiological artifacts is that they primarily account for noise and not for the variance of interest related to the neural signal. A comparison of HR-based CRFs derived from different tissue signals showed that HR-based CRFs mainly explain cardiac noise, while the neural signal has little influence on their shape. Evidence for a non-negative effect of these functions on the neural signal was found when investigating FC differences in brain areas involved in cardiac autonomic control. In this analysis, HR-based CRFs corrected for non-neuronal cardiac artifacts without sacrificing signal variance attributable

to the neural activity associated with HR changes. This result has important implications for studies investigating brain-heart interactions at rest. Low variations in autonomic activity and high noise sensitivity are well-known drawbacks of resting-state fMRI, which make brain-heart interactions challenging to detect using this technique. Thus, the fact that the correction of physiological noise via HR-based CRFs does not remove meaningful variance components opens new opportunities for the use of resting-state fMRI in the investigation of neural correlates of cardiac regulation. Task-based fMRI can also benefit from the noise reduction offered by the use of HR-based CRFs. Still, caution should be exercised in tasks where HR variations strongly correlate with global activity changes as there is a risk of excessive removal of meaningful variance.

There is a large body of fMRI research showing that activity in central autonomic network (CAN) regions covaries with HR changes. However, the present work represents the first direct evidence of a nonlinear relationship between HR and FC of autonomic brain regions in the resting-state condition [70]. This association confirms the role of CAN regions in cardiac regulation and provides a proof-of-concept for the use of HR as a potential biomarker of CAN functional integration. Moreover, these findings can be interpreted in the context of the Neurovisceral Integration Model (NIM). The identified CAN regions, whose connectivity covary with HR, are the same as those areas postulated by the NIM responsible for the adaptive regulation of emotions, cognitions, behaviors, and HR variability. Therefore, the presented results on brain-heart interaction provide additional evidence supporting the NIM. While speculative, the observation of higher functional connectivity at slower HRs suggests that, beyond strengthening brain network connectivity, slower HR may potentially exert a positive effect on emotion regulation and self-control.

The analysis of HR undertaken here has extended our knowledge of physiological noise in the BOLD signal and emphasizes the need for always considering HR when analyzing BOLD data. To further test the applications of the findings presented in this thesis, the new model for noise correction needs to be tested under different MRI and brain conditions in conjunction with experimental tasks. In particular, it would be interesting to derive HR-based CRFs in elderly subjects as there is accumulating evidence that the hemodynamic response varies with age [2]. This work has also aroused curiosity about the appearance of the nonlinear coupling FC-HR under different brain conditions. For example, patients with psychiatric disorders often exhibit significantly altered HR and FC compared to control subjects [12, 217]. One can expect that these alterations may also affect the coupling between FC and HR. A better understanding of brain-body interactions could help to shed light on the nature of spontaneous brain activity as well as the origin and dynamics of resting-state networks.

Appendix

A.1 Simulation pipeline

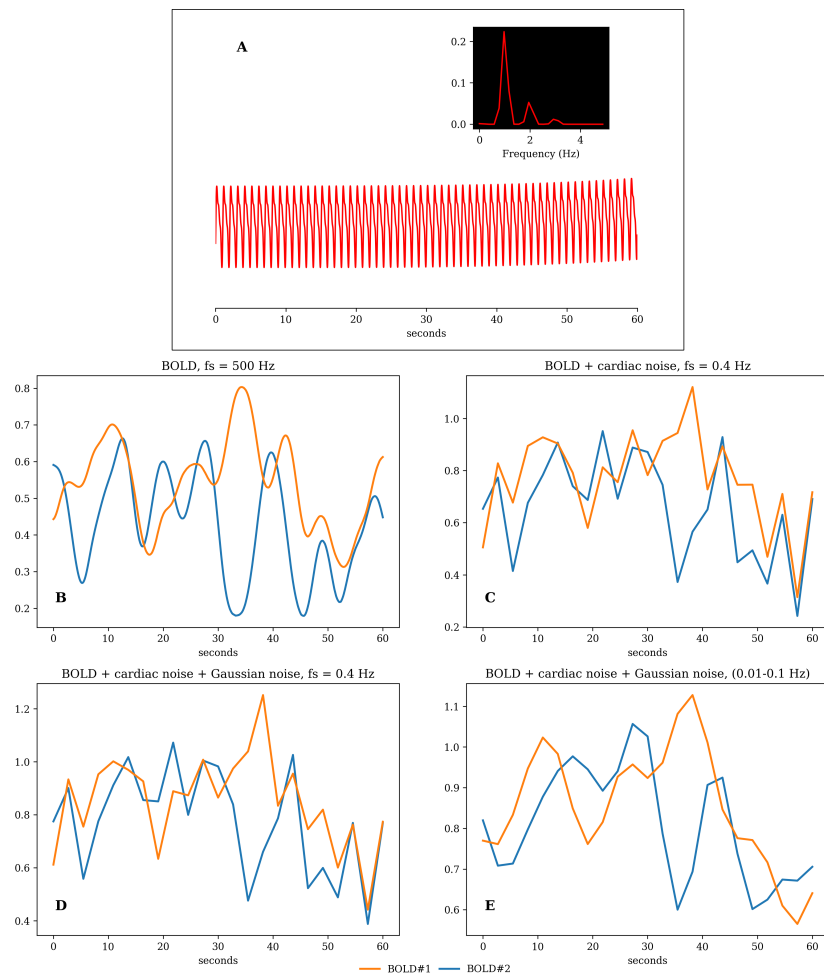


Figure A.1: **A)** 60 s of a non-stationary simulated cardiac signal. The power spectrum shows the fundamental frequency (1 Hz), and 2nd, and 3th harmonics. **B)** 60 s of two BOLD signals simulated using a VAR model, sampled at 500 Hz. **C)** The BOLD signals corrupted by cardiac noise and down-sampled at 0.4 Hz (TR = 2.5 s). **D)** Gaussian noise was further added to represent measurement error and noise in the acquisition. **E)** The BOLD signals corrupted by cardiac and Gaussian noise were pass-band filtered between 0.01-0.1 Hz for functional connectivity.

A.2 Variance explained at the individual level

Table A.1: Variance explained in each subject by the canonical CRF, individualized CRF (CRFi) and group-specific CRF (CRFg). % voxels: indicates percentage of voxels in the brain with significant R^2 ($p < 0.01$, F -test). Mean % R^2 corresponds to % R^2 values averaged over significant voxels, while SD indicates the standard deviation.

	Subject	CRF		CRFi		CRFg	
		% voxels	% R^2 mean \pm SD	% voxels	% R^2 mean \pm SD	% voxels	% R^2 mean \pm SD
SHR	1	4.02	3.86 \pm 0.99	1.67	3.69 \pm 0.89	10.75	4.14 \pm 1.29
	2	40.78	5.64 \pm 2.28	6.76	3.88 \pm 1.00	2.36	4.12 \pm 1.68
	3	17.65	4.66 \pm 1.73	17.12	4.62 \pm 1.68	25.33	4.98 \pm 1.96
	4	6.35	4.09 \pm 1.29	7.05	4.14 \pm 1.33	12.36	4.76 \pm 1.94
	5	4.95	3.79 \pm 0.88	6.52	4.07 \pm 1.18	0.99	3.54 \pm 0.68
	6	0.91	3.42 \pm 0.60	1.39	3.65 \pm 0.80	4.89	3.94 \pm 1.04
	7	0.25	3.24 \pm 0.37	4.37	4.37 \pm 1.38	0.82	3.37 \pm 0.50
	8	37.95	6.89 \pm 3.17	43.95	8.22 \pm 4.37	46.23	8.60 \pm 4.87
	9	0.31	3.39 \pm 0.54	2.03	3.61 \pm 0.76	2.33	3.75 \pm 0.96
	10	3.31	3.82 \pm 0.93	2.20	3.74 \pm 0.94	2.82	3.98 \pm 1.16
	11	0.91	3.47 \pm 0.62	3.23	3.79 \pm 0.96	1.57	3.61 \pm 0.77
	12	1.57	3.77 \pm 0.91	2.85	3.68 \pm 0.87	2.54	3.84 \pm 1.07
	13	5.54	4.02 \pm 1.17	1.50	3.76 \pm 0.93	7.01	3.96 \pm 1.10
	14	3.40	3.94 \pm 1.17	3.07	3.80 \pm 0.98	26.57	5.12 \pm 2.22
	15	10.45	4.08 \pm 1.18	9.52	4.30 \pm 1.41	9.60	4.64 \pm 1.77
	16	3.22	3.87 \pm 1.01	3.54	3.92 \pm 1.09	1.76	3.61 \pm 0.80
	17	25.30	4.26 \pm 1.06	1.43	3.25 \pm 0.40	34.73	4.51 \pm 1.35
	18	33.71	4.86 \pm 1.73	40.68	4.93 \pm 1.82	23.20	5.36 \pm 2.34
	19	8.21	4.61 \pm 1.86	21.28	5.81 \pm 3.07	17.42	4.77 \pm 1.75
	20	6.08	4.17 \pm 1.34	5.63	3.87 \pm 0.99	2.25	3.69 \pm 0.86
	21	7.70	4.22 \pm 1.32	0.59	3.64 \pm 0.85	11.99	3.94 \pm 0.94
	22	11.78	4.18 \pm 1.28	2.26	3.63 \pm 0.77	12.15	4.18 \pm 1.34
	23	2.70	3.70 \pm 0.87	4.76	3.81 \pm 0.92	20.79	4.43 \pm 1.50
	24	9.54	4.64 \pm 1.60	1.22	3.69 \pm 0.89	10.63	4.85 \pm 2.01
	25	5.61	4.02 \pm 1.08	10.39	4.17 \pm 1.39	14.40	4.20 \pm 1.33
	26	34.37	7.72 \pm 4.12	7.81	4.91 \pm 2.20	15.88	5.00 \pm 2.09
	27	2.26	3.58 \pm 0.71	1.77	3.59 \pm 0.82	2.91	3.72 \pm 0.98
	28	0.18	3.54 \pm 0.83	5.38	4.06 \pm 1.25	4.03	3.97 \pm 1.19
	Ave.	10.32	4.27 \pm 1.31	7.86	4.16 \pm 1.28	11.73	4.38 \pm 1.48
MHR	1	5.23	3.89 \pm 1.03	7.37	4.38 \pm 1.36	4.96	4.06 \pm 1.31

Continued on next page

A.2 Variance explained at the individual level

Table A.1 – *Continued from previous page*

Subject	CRF		CRFi		CRFg	
	%	% R^2	%	% R^2	%	% R^2
	voxels	mean \pm SD	voxels	mean \pm SD	voxels	mean \pm SD
2	5.87	4.43 \pm 1.63	0.72	3.45 \pm 0.62	0.62	3.39 \pm 0.54
3	2.58	3.78 \pm 0.93	24.44	5.28 \pm 2.18	3.36	3.81 \pm 1.01
4	6.90	3.61 \pm 0.75	4.62	3.97 \pm 1.13	2.31	3.66 \pm 0.78
5	8.36	4.20 \pm 1.25	4.17	4.05 \pm 1.33	1.29	3.70 \pm 0.94
6	0.91	3.54 \pm 0.69	10.45	4.23 \pm 1.21	1.85	3.66 \pm 0.77
7	4.97	3.90 \pm 1.10	23.81	4.74 \pm 1.55	7.68	3.79 \pm 0.92
8	4.40	3.87 \pm 1.02	1.54	3.54 \pm 0.70	1.22	3.76 \pm 0.95
9	15.77	4.79 \pm 1.82	17.08	4.69 \pm 1.79	21.74	4.83 \pm 1.91
10	2.89	3.72 \pm 0.84	9.58	4.31 \pm 1.46	5.77	4.05 \pm 1.24
11	7.95	4.20 \pm 1.37	13.38	5.45 \pm 3.11	14.46	3.91 \pm 0.92
12	6.03	4.54 \pm 2.16	4.05	4.00 \pm 1.20	7.57	4.12 \pm 1.19
13	4.55	3.79 \pm 0.97	1.45	3.50 \pm 0.64	3.67	3.90 \pm 1.07
14	10.28	4.38 \pm 1.69	3.38	3.87 \pm 1.08	11.72	4.71 \pm 1.72
15	5.81	4.10 \pm 1.34	1.80	3.63 \pm 0.79	0.46	3.47 \pm 0.68
16	1.27	3.55 \pm 0.71	4.28	3.79 \pm 0.91	0.65	3.49 \pm 0.79
17	3.88	3.85 \pm 0.96	2.98	3.83 \pm 1.01	15.09	5.22 \pm 2.51
18	4.44	3.70 \pm 0.82	22.85	4.78 \pm 1.79	7.81	4.17 \pm 1.26
19	0.91	3.62 \pm 0.83	2.12	3.82 \pm 1.01	1.59	3.50 \pm 0.66
20	11.65	4.46 \pm 1.59	36.76	5.80 \pm 2.71	26.26	5.33 \pm 2.47
21	3.01	3.86 \pm 1.08	8.23	3.98 \pm 1.06	28.47	6.53 \pm 3.45
22	4.34	3.96 \pm 1.09	4.51	3.93 \pm 1.08	11.04	4.81 \pm 1.93
23	27.64	5.15 \pm 1.98	4.97	4.36 \pm 1.63	29.79	5.59 \pm 2.48
24	7.47	3.81 \pm 0.92	20.29	5.07 \pm 2.13	12.32	5.13 \pm 2.12
25	5.83	4.28 \pm 1.44	9.48	4.00 \pm 1.14	9.50	3.91 \pm 1.03
26	2.41	3.71 \pm 0.86	2.59	3.73 \pm 0.90	5.87	4.06 \pm 1.24
27	3.21	3.95 \pm 1.30	17.40	5.52 \pm 3.07	4.40	4.26 \pm 1.56
28	2.10	3.38 \pm 0.53	0.51	3.41 \pm 0.61	15.97	4.26 \pm 1.24
Ave.	6.10	4.00 \pm 1.17	9.46	4.25 \pm 1.40	9.19	4.25 \pm 1.38
FHR						
1	8.14	4.10 \pm 1.21	2.40	3.83 \pm 1.01	3.20	3.79 \pm 0.99
2	5.83	3.94 \pm 1.08	18.97	4.86 \pm 1.90	19.44	4.61 \pm 1.67
3	12.01	4.25 \pm 1.27	0.69	3.46 \pm 0.71	7.15	4.59 \pm 1.84
4	0.21	3.29 \pm 0.53	10.45	4.30 \pm 1.42	3.51	3.64 \pm 0.76
5	31.76	5.75 \pm 2.76	28.32	5.55 \pm 2.41	14.40	4.56 \pm 1.60
6	2.74	3.87 \pm 1.06	1.12	3.50 \pm 0.69	0.66	3.44 \pm 0.63
7	20.07	4.90 \pm 1.87	4.51	3.86 \pm 1.04	5.75	3.96 \pm 1.10

Continued on next page

A.2 Variance explained at the individual level

Table A.1 – *Continued from previous page*

Subject	CRF		CRFi		CRFg	
	%	% R^2	%	% R^2	%	% R^2
	voxels	mean \pm SD	voxels	mean \pm SD	voxels	mean \pm SD
8	1.10	3.48 \pm 0.59	0.89	3.45 \pm 0.62	3.18	3.74 \pm 0.89
9	0.18	3.31 \pm 0.45	4.19	4.08 \pm 1.21	8.04	3.86 \pm 0.98
10	7.01	3.98 \pm 1.11	1.01	3.39 \pm 0.58	6.11	4.25 \pm 1.36
11	2.81	3.77 \pm 0.95	6.58	3.97 \pm 1.09	24.86	4.97 \pm 2.01
12	2.49	3.71 \pm 0.89	2.48	3.82 \pm 1.00	10.44	4.20 \pm 1.33
13	1.50	3.73 \pm 0.88	2.39	3.60 \pm 0.72	0.80	3.45 \pm 0.61
14	5.16	4.09 \pm 1.34	8.11	4.77 \pm 1.89	5.20	4.08 \pm 1.26
15	14.61	4.48 \pm 1.50	4.05	4.30 \pm 1.46	19.73	4.41 \pm 1.34
16	7.96	3.99 \pm 1.08	10.64	4.09 \pm 1.15	23.12	4.58 \pm 1.55
17	4.09	3.86 \pm 0.94	4.17	4.00 \pm 1.13	13.25	4.30 \pm 1.43
18	13.38	4.42 \pm 1.50	29.20	6.63 \pm 3.83	2.46	3.72 \pm 0.89
19	6.87	4.22 \pm 1.34	4.82	4.17 \pm 1.09	14.48	4.56 \pm 1.68
20	2.41	3.67 \pm 0.82	13.69	4.85 \pm 2.19	5.24	4.23 \pm 1.51
21	1.24	3.61 \pm 0.78	5.79	4.13 \pm 1.25	1.66	3.51 \pm 0.70
22	2.40	3.67 \pm 0.87	2.39	3.71 \pm 0.90	4.25	3.74 \pm 0.88
23	1.08	3.49 \pm 0.68	0.63	3.48 \pm 0.65	1.13	3.52 \pm 0.74
24	2.37	3.85 \pm 1.01	6.24	3.80 \pm 0.90	2.66	3.61 \pm 0.76
25	1.21	3.48 \pm 0.61	13.72	4.35 \pm 1.41	11.83	4.40 \pm 1.50
26	3.27	3.74 \pm 0.83	0.67	3.41 \pm 0.53	0.53	3.40 \pm 0.53
27	1.84	3.78 \pm 0.93	2.20	3.81 \pm 1.00	2.03	3.67 \pm 0.85
28	12.39	5.19 \pm 2.43	26.78	4.99 \pm 1.91	30.35	5.03 \pm 2.01
Ave.	6.29	3.99 \pm 1.12	7.75	4.15 \pm 1.27	8.77	4.07 \pm 1.19

References

- [1] Ainslie, P. N., Ashmead, J. C., Ide, K., Morgan, B. J., and Poulin, M. J. (2005). Differential responses to CO₂ and sympathetic stimulation in the cerebral and femoral circulations in humans. *The Journal of Physiology*, 566(2):613–624.
- [2] Aizenstein, H. J., Clark, K. A., Butters, M. A., Cochran, J., Stenger, V. A., Meltzer, C. C., Reynolds, C. F., and Carter, C. S. (2004). The bold hemodynamic response in healthy aging. *Journal of Cognitive Neuroscience*, 16(5):786–793.
- [3] Akselrod, S., Gordon, D., Ubel, F. A., Shannon, D. C., Berger, A. C., and Cohen, R. J. (1981). Power spectrum analysis of heart rate fluctuation: a quantitative probe of beat-to-beat cardiovascular control. *Science (New York, N.Y.)*, 213(4504):220–2.
- [4] Alsop, D. C., Dai, W., Grossman, M., and Detre, J. A. (2010). Arterial Spin Labeling Blood Flow MRI: Its Role in the Early Characterization of Alzheimer’s Disease. *Journal of Alzheimer’s Disease*, 20:871–880.
- [5] Armel, K. C. and Ramachandran, V. S. (2003). Projecting sensations to external objects: evidence from skin conductance response. *Proceedings of the Royal Society B: Biological Sciences*, 270(1523):1499–1506.
- [6] Ashburner, J. and Friston, K. J. (2005). Unified segmentation. *Neuroimage*, 26(3):839–851.
- [7] Azzalini, D., Rebollo, I., and Tallon-Baudry, C. (2019). Visceral Signals Shape Brain Dynamics and Cognition. *Trends in Cognitive Sciences*, 23(6):488–509.
- [8] Bach, D. R. (2014). Sympathetic nerve activity can be estimated from skin conductance responses — a comment on henderson et al. (2012). *NeuroImage*, 84:122 – 123.
- [9] Bach, D. R., Friston, K. J., and Dolan, R. J. (2010). Analytic measures for quantification of arousal from spontaneous skin conductance fluctuations. *International Journal of Psychophysiology*, 76(1):52–55.
- [10] Bandettini, P. A., Jesmanowicz, A., Wong, E. C., and Hyde, J. S. (1993). Processing strategies for time-course data sets in functional MRI of the human brain. *Magnetic resonance in medicine*, 30(2):161–73.
- [11] Bandettini, P. A., Wong, E. C., Hinks, R. S., Tikofsky, R. S., and Hyde, J. S. (1992). Time course EPI of human brain function during task activation. *Magn Reson Med*, 25(2):390–397.
- [12] Bär, K.-J., De la Cruz, F., Berger, S., Schultz, C. C., and Wagner, G. (2015). Structural and functional differences in the cingulate cortex relate to disease severity in anorexia nervosa. *Journal of psychiatry & neuroscience*, 40 4:269–79.

- [13] Barber, T. X. and Hahn, K. W. (1963). Hypnotic Induction and "Relaxation". *Archives of General Psychiatry*, 8(3):295.
- [14] Barnes, A., Bullmore, E. T., and Suckling, J. (2009). Endogenous Human Brain Dynamics Recover Slowly Following Cognitive Effort. *PLoS ONE*, 4(8):e6626.
- [15] Bates, S., Yetkin, Z., Jesmanowicz, A., Hyde, J. S., Bandettini, P. A., Estkowski, L., and Haughton, V. M. (1995). Artifacts in functional magnetic resonance imaging from gaseous oxygen. *Journal of Magnetic Resonance Imaging*, 5(4):443–445.
- [16] Bauer, K. E. and McCanne, T. R. (1980). Autonomic and central nervous system responding: During hypnosis and simulation of hypnosis. *International Journal of Clinical and Experimental Hypnosis*, 28(2):148–163.
- [17] Beall, E. B. (2010). Adaptive cyclic physiologic noise modeling and correction in functional MRI. *J Neurosci Methods*, 187(2):216–228.
- [18] Beissner, F., Meissner, K., Bär, K.-J., and Napadow, V. (2013). The Autonomic Brain: An Activation Likelihood Estimation Meta-Analysis for Central Processing of Autonomic Function. *Journal of Neuroscience*, 33(25):10503–10511.
- [19] Bell, A. J. and Sejnowski, T. J. (1995). An Information-Maximization Approach to Blind Separation and Blind Deconvolution. *Neural Computation*, 7(6):1129–1159.
- [20] Benarroch, E. E. (1993). The central autonomic network: functional organization, dysfunction, and perspective. *Mayo Clin Proc*, 68(10):988–1001.
- [21] Benarroch, E. E. (1997). The Central Autonomic Network. *In: Low PA, editor. Clinical Autonomic Disorders. 2 ed. Philadelphia: Lippincott-Raven Publishers*, pages 17–23.
- [22] Bhattacharyya, P. K. and Lowe, M. J. (2004). Cardiac-induced physiologic noise in tissue is a direct observation of cardiac-induced fluctuations. *Magnetic Resonance Imaging*, 22(1):9–13.
- [23] Bianciardi, M., Fukunaga, M., van Gelderen, P., Horovitz, S. G., de Zwart, J. A., Shmueli, K., and Duyn, J. H. (2009). Sources of functional magnetic resonance imaging signal fluctuations in the human brain at rest: a 7 T study. *Magnetic Resonance Imaging*, 27(8):1019–1029.
- [24] Birkholz, T., Schmid, M., Nimsky, C., Schüttler, J., and Schmitz, B. (2004). ECG artifacts during intraoperative high-field MRI scanning. *Journal of neurosurgical anesthesiology*, 16(4):271–6.
- [25] Birn, R. M. (2012). The role of physiological noise in resting-state functional connectivity. *Neuroimage*, 62(2):864–870.
- [26] Birn, R. M., Diamond, J. B., Smith, M. A., and Bandettini, P. A. (2006). Separating respiratory-variation-related fluctuations from neuronal-activity-related fluctuations in fMRI. *Neuroimage*, 31(4):1536–1548.
- [27] Birn, R. M., Molloy, E. K., Patriat, R., Parker, T., Meier, T. B., Kirk, G. R., Nair, V. A., Meyerand, M. E., and Prabhakaran, V. (2013). The effect of scan length on the reliability of resting-state fMRI connectivity estimates. *NeuroImage*, 83(Supplement C):550–558.
- [28] Birn, R. M., Murphy, K., Handwerker, D. A., and Bandettini, P. A. (2009). fMRI in the presence of task-correlated breathing variations. *NeuroImage*, 47(3):1092–1104.

- [29] Birn, R. M., Smith, M. A., Jones, T. B., and Bandettini, P. A. (2008). The respiration response function: the temporal dynamics of fMRI signal fluctuations related to changes in respiration. *Neuroimage*, 40(2):644–654.
- [30] Bisdas, S., Al-Busaidi, A., Mancini, L., Papadaki, A., Siakallis, L., and Yamamoto, A. K. (2019). Functional MRI in Epilepsy. In *Epilepsy Surgery and Intrinsic Brain Tumor Surgery*, pages 25–44. Springer International Publishing, Cham.
- [31] Biswal, B., DeYoe, E. A., and Hyde, J. S. (1996). Reduction of physiological fluctuations in fMRI using digital filters. *Magnetic Resonance in Medicine*, 35(1):107–113.
- [32] Biswal, B., Yetkin, F. Z., Haughton, V. M., and Hyde, J. S. (1995). Functional connectivity in the motor cortex of resting human brain using echo-planar MRI. *Magnetic resonance in medicine*, 34(4):537–41.
- [33] Bland, J. M. and Altman, D. G. (2009). Analysis of continuous data from small samples. *BMJ*, 338.
- [34] Bloch, F. (1946). Nuclear induction. *Phys. Rev.*, 70:460–474.
- [35] Blomqvist, C. G. and Saltin, B. (1983). Cardiovascular Adaptations to Physical Training. *Annual Review of Physiology*, 45(1):169–189.
- [36] Boettger, M. K., Schulz, S., Berger, S., Tancer, M., Yeragani, V. K., Voss, A., and Bär, K.-J. (2010). Influence of Age on Linear and Nonlinear Measures of Autonomic Cardiovascular Modulation. *Annals of Noninvasive Electrocardiology*, 15(2):165–174.
- [37] Boucsein, W. (2012). *Electrodermal Activity*. The Springer series in behavioral psychophysiology and medicine. Springer US.
- [38] Bourke, J. H. and Wall, M. B. (2015). phMRI: methodological considerations for mitigating potential confounding factors. *Frontiers in neuroscience*, 9:167.
- [39] Boxerman, J. L., Bandettini, P. A., Kwong, K. K., Baker, J. R., Davis, T. L., Rosen, B. R., and Weisskoff, R. M. (1995). The intravascular contribution to fmri signal change: monte carlo modeling and diffusion-weighted studies in vivo. *Magnetic Resonance in Medicine*, 34(1):4–10.
- [40] Brewer, J. A., Worhunsky, P. D., Gray, J. R., Tang, Y.-Y., Weber, J., and Kober, H. (2011). Meditation experience is associated with differences in default mode network activity and connectivity. *Proceedings of the National Academy of Sciences*, 108(50):20254–20259.
- [41] Briggs, G. G. and Nebes, R. D. (1975). Patterns of hand preference in a student population. *Cortex*, 11(3):230–238.
- [42] Bright, M. G. and Murphy, K. (2013). Removing motion and physiological artifacts from intrinsic BOLD fluctuations using short echo data. *Neuroimage*, 64:526–537.
- [43] Britt, R. and Rossi, G. (1982). Quantitative analysis of methods for reducing physiological brain pulsations. *Journal of Neuroscience Methods*, 6(3):219 – 229.
- [44] Brooks, J. C., Beckmann, C. F., Miller, K. L., Wise, R. G., Porro, C. A., Tracey, I., and Jenkinson, M. (2008). Physiological noise modelling for spinal functional magnetic resonance imaging studies. *NeuroImage*, 39(2):680 – 692.
- [45] Brooks, J. C. W., Faull, O. K., Pattinson, K. T. S., and Jenkinson, M. (2013). Physiological Noise in Brainstem fMRI. *Frontiers in Human Neuroscience*, 7:1–13.

- [46] Brosch, J. R., Talavage, T. M., Ulmer, J. L., and Nyenhuis, J. A. (2002). Simulation of human respiration in fMRI with a mechanical model. *IEEE Trans Biomed Eng*, 49(7):700–707.
- [47] Buckner, R. L., Andrews-Hanna, J. R., and Schacter, D. L. (2008). The Brain’s Default Network. *Annals of the New York Academy of Sciences*, 1124(1):1–38.
- [48] Buxton, R. B. and Frank, L. R. (1997). A Model for the Coupling between Cerebral Blood Flow and Oxygen Metabolism during Neural Stimulation. *Journal of Cerebral Blood Flow & Metabolism*, 17(1):64–72.
- [49] Buxton, R. B., Wong, E. C., and Frank, L. R. (1998). Dynamics of blood flow and oxygenation changes during brain activation: the balloon model. *Magn Reson Med*, 39(17):855–864.
- [50] Caballero-Gaudes, C. and Reynolds, R. C. (2017). Methods for cleaning the BOLD fMRI signal. *NeuroImage*, 154:128–149.
- [51] Casanova, R., Ryali, S., Serences, J., Yang, L., Kraft, R., Laurienti, P. J., and Maldjian, J. A. (2008). The impact of temporal regularization on estimates of the BOLD hemodynamic response function: a comparative analysis. *NeuroImage*, 40(4):1606–1618.
- [52] Caspers, C., Cleveland, S., and Schipke, J. D. (2011). Diving reflex: can the time course of heart rate reduction be quantified?. *Scandinavian journal of medicine & science in sports*, 21(1):18–31.
- [53] Chang, C., Cunningham, J. P., and Glover, G. H. (2009). Influence of heart rate on the BOLD signal: the cardiac response function. *Neuroimage*, 44(3):857–869.
- [54] Chang, C. and Glover, G. H. (2009). Relationship between respiration, end-tidal CO₂, and BOLD signals in resting-state fMRI. *NeuroImage*, 47(4):1381–1393.
- [55] Chang, C., Leopold, D. A., Schölvinck, M. L., Mandelkow, H., Picchioni, D., Liu, X., Ye, F. Q., Turchi, J. N., and Duyn, J. H. (2016a). Tracking brain arousal fluctuations with fmri. *Proceedings of the National Academy of Sciences*, 113(16):4518–4523.
- [56] Chang, C., Metzger, C. D., Glover, G. H., Duyn, J. H., Heinze, H.-J., and Walter, M. (2013). Association between heart rate variability and fluctuations in resting-state functional connectivity. *Neuroimage*, 68:93–104.
- [57] Chang, C., Raven, E. P., and Duyn, J. H. (2016b). Brain-heart interactions: challenges and opportunities with functional magnetic resonance imaging at ultra-high field. *Philos Trans A Math Phys Eng Sci*, 374(2067).
- [58] Chen, G., Chen, G., Xie, C., Ward, B. D., Li, W., Antuono, P., and Li, S.-J. (2012). A method to determine the necessity for global signal regression in resting-state fmri studies. *Magnetic Resonance in Medicine*, 68(6):1828–1835.
- [59] Chen, J. E. and Glover, G. H. (2015). BOLD fractional contribution to resting-state functional connectivity above 0.1 Hz. *NeuroImage*, 107:207–218.
- [60] Chen, L., Vu, A. T., Xu, J., Moeller, S., Ugurbil, K., Yacoub, E., and Feinberg, D. A. (2015). Evaluation of highly accelerated simultaneous multi-slice EPI for fMRI. *NeuroImage*, 104:452–459.

- [61] Christoff, K., Gordon, A. M., Smallwood, J., Smith, R., and Schooler, J. W. (2009). Experience sampling during fMRI reveals default network and executive system contributions to mind wandering. *Proceedings of the National Academy of Sciences of the United States of America*, 106(21):8719–24.
- [62] Cohen, M. A. and Taylor, J. A. (2002). Short-term cardiovascular oscillations in man: measuring and modelling the physiologies. *The Journal of Physiology*, 542(3):669–683.
- [63] Cordes, D., Haughton, V. M., Arfanakis, K., Carew, J. D., Turski, P. A., Moritz, C. H., Quigley, M. A., and Meyerand, M. E. (2001). Frequencies contributing to functional connectivity in the cerebral cortex in “resting-state” data. *American Journal of Neuroradiology*, 22(7):1326–1333.
- [64] Cordes, D., Nandy, R. R., Schafer, S., and Wager, T. D. (2014). Characterization and reduction of cardiac- and respiratory-induced noise as a function of the sampling rate (TR) in fMRI. *Neuroimage*, 89:314–330.
- [65] Cox, R. W., Chen, G., Glen, D. R., Reynolds, R. C., and Taylor, P. A. (2017). FMRI Clustering in AFNI: False-Positive Rates Redux. *Brain Connectivity*, 7(3):152–171.
- [66] Cox, R. W. and Jesmanowicz, A. (1999). Real-time 3d image registration for functional mri. *Magnetic Resonance in Medicine*, 42(6):1014–1018.
- [67] Critchley, H. D., Corfield, D. R., Chandler, M. P., Mathias, C. J., and Dolan, R. J. (2000). Cerebral correlates of autonomic cardiovascular arousal: a functional neuroimaging investigation in humans. *J Physiol*, 523 Pt 1:259–270.
- [68] Dagli, M. S., Ingeholm, J. E., and Haxby, J. V. (1999). Localization of cardiac-induced signal change in fMRI. *Neuroimage*, 9(4):407–415.
- [69] de la Cruz, F., Schumann, A., Köhler, S., Bär, K.-J., and Wagner, G. (2017). Impact of the heart rate on the shape of the cardiac response function. *NeuroImage*, 162:214–225.
- [70] de la Cruz, F., Schumann, A., Köhler, S., Reichenbach, J. R., Wagner, G., and Bär, K. J. (2019). The relationship between heart rate and functional connectivity of brain regions involved in autonomic control. *NeuroImage*, 196:318–328.
- [71] de Munck, J. C., Gonçalves, S. I., Faes, T. J. C., Kuijter, J. P. A., Pouwels, P. J. W., Heethaar, R. M., and Lopes da Silva, F. H. (2008). A study of the brain’s resting state based on alpha band power, heart rate and fMRI. *NeuroImage*, 42(1):112–121.
- [72] De Munck, J. C., Goncalves, S. I., Faes, T. J. C., Pouwels, P. J. W., Kuijter, J. P. A., Heethaar, R. M., and Lopes Da Silva, F. H. (2007). The relation between alpha band power, heart rate and fMRI. *2007 4th IEEE International Symposium on Biomedical Imaging: From Nano to Macro - Proceedings*, (1):436–439.
- [73] De Zanche, N., Barmet, C., Nordmeyer-Massner, J. A., and Pruessmann, K. P. (2008). Nmr probes for measuring magnetic fields and field dynamics in mr systems. *Magnetic Resonance in Medicine*, 60(1):176–186.
- [74] Debenedittis, G., Cigada, M., Bianchi, A., Signorini, M. G., and Cerutti, S. (1994). Autonomic changes during hypnosis: A heart rate variability power spectrum analysis as a marker of sympatho-vagal balance. *International Journal of Clinical and Experimental Hypnosis*, 42(2):140–152.

- [75] Deco, G., Hagmann, P., Hudetz, A. G., and Tononi, G. (2014). Modeling Resting-State Functional Networks When the Cortex Falls Asleep: Local and Global Changes. *Cerebral Cortex*, 24(12):3180–3194.
- [76] Dickey, D. A. and Fuller, W. A. (1979). Distribution of the estimators for autoregressive time series with a unit root. *Journal of the American Statistical Association*, 74(366):427–431.
- [77] Elster, A. D. (1993). Gradient-echo MR imaging: techniques and acronyms. *Radiology*, 186(1):1–8.
- [78] Enzmann, D. R. and Pelc, N. J. (1992). Brain motion: measurement with phase-contrast MR imaging. *Radiology*, 185(3):653–660.
- [79] Ernst, T. and Hennig, J. (1994). Observation of a fast response in functional MR. *Magnetic resonance in medicine*, 32(1):146–9.
- [80] Evans, A. C., Collins, D. L., Mills, S. R., Brown, E. D., Kelly, R. L., and Peters, T. M. (1993). 3d statistical neuroanatomical models from 305 mri volumes. In *1993 IEEE Conference Record Nuclear Science Symposium and Medical Imaging Conference*, pages 1813–1817 vol.3.
- [81] Falahpour, M., Refai, H., and Bodurka, J. (2013). Subject specific BOLD fMRI respiratory and cardiac response functions obtained from global signal. *Neuroimage*, 72:252–264.
- [82] Faymonville, M.-E., Roediger, L., Del Fiore, G., Delguedre, C., Phillips, C., Lamy, M., Luxen, A., Maquet, P., and Laureys, S. (2003). Increased cerebral functional connectivity underlying the antinociceptive effects of hypnosis. *Cognitive Brain Research*, 17(2):255–262.
- [83] Feinberg, D. A. and Mark, A. S. (1987). Human brain motion and cerebrospinal fluid circulation demonstrated with MR velocity imaging. *Radiology*, 163(3):793–799.
- [84] Feinberg, D. A., Moeller, S., Smith, S. M., Auerbach, E., Ramanna, S., Glasser, M. F., Miller, K. L., Ugurbil, K., and Yacoub, E. (2010). Multiplexed echo planar imaging for sub-second whole brain fmri and fast diffusion imaging. *PLoS ONE*, 5(12).
- [85] Feldt, S., Bonifazi, P., and Cossart, R. (2011). Dissecting functional connectivity of neuronal microcircuits: experimental and theoretical insights. *Trends in Neurosciences*, 34(5):225–236.
- [86] Finn, E. S., Scheinost, D., Finn, D. M., Shen, X., Papademetris, X., and Constable, R. T. (2017). Can brain state be manipulated to emphasize individual differences in functional connectivity?. *NeuroImage*, 160:140 – 151.
- [87] Fox, M. D. and Greicius, M. (2010). Clinical applications of resting state functional connectivity. *Frontiers in Systems Neuroscience*, 4(June).
- [88] Friston, K., Moran, R., and Seth, A. K. (2013). Analysing connectivity with granger causality and dynamic causal modelling. *Current Opinion in Neurobiology*, 23(2):172 – 178.
- [89] Friston, K. J., Frith, C. D., Liddle, P. F., and Frackowiak, R. S. J. (1993). Functional Connectivity: The Principal-Component Analysis of Large (PET) Data Sets. *Journal of Cerebral Blood Flow & Metabolism*, 13(1):5–14.
- [90] Friston, K. J., Jezzard, P., and Turner, R. (1994). Analysis of functional mri time-series. *Human Brain Mapping*, 1(2):153–171.

- [91] Friston, K. J., Williams, S., Howard, R., Frackowiak, R. S., and Turner, R. (1996). Movement-related effects in fMRI time-series. *Magnetic Resonance in Medicine*, 35(3):346–355.
- [92] Füchtemeier, M., Leithner, C., Offenhauser, N., Foddis, M., Kohl-Bareis, M., Dirnagl, U., Lindauer, U., and Roysl, G. (2010). Elevating intracranial pressure reverses the decrease in deoxygenated hemoglobin and abolishes the post-stimulus overshoot upon somatosensory activation in rats. *NeuroImage*, 52(2):445–454.
- [93] Fujii, K., Heistad, D. D., and Faraci, F. M. (1990). Vasomotion of basilar arteries in vivo. *American Journal of Physiology-Heart and Circulatory Physiology*, 258(6):H1829–H1834. PMID: 2360673.
- [94] Furlan, R., Porta, A., Costa, F., Tank, J., Baker, L., Schiavi, R., Robertson, D., Malliani, A., and Mosqueda-Garcia, R. (2000). Oscillatory patterns in sympathetic neural discharge and cardiovascular variables during orthostatic stimulus. *Circulation*, 101(8):886–92.
- [95] Galletly, D. C. and Larsen, P. D. (1998). Relationship between cardioventilatory coupling and respiratory sinus arrhythmia. *British Journal of Anaesthesia*, 80(2):164–168.
- [96] Glover, G. H. (1999). Deconvolution of impulse response in event-related BOLD fMRI. *NeuroImage*, 9(4):416–429.
- [97] Glover, G. H., Li, T. Q., and Ress, D. (2000). Image-based method for retrospective correction of physiological motion effects in fMRI: RETROICOR. *Magn Reson Med*, 44(1):162–167.
- [98] Golestani, A. M., Chang, C., Kwinta, J. B., Khatamian, Y. B., and Jean Chen, J. (2015). Mapping the end-tidal CO₂ response function in the resting-state BOLD fMRI signal: spatial specificity, test-retest reliability and effect of fMRI sampling rate. *Neuroimage*, 104:266–277.
- [99] Golestani, A. M., Faraji-Dana, Z., Kayvanrad, M. A., Setsompop, K., Graham, S., and Chen, J. J. (2017). Simultaneous Multi-slice Resting-state fMRI at 3 Tesla: Slice-Acceleration Related Biases in Physiological Effects. *Brain Connectivity*, page brain.2017.0491.
- [100] Good, C. D., Johnsrude, I. S., Ashburner, J., Henson, R. N., Friston, K. J., and Frackowiak, R. S. (2001). A voxel-based morphometric study of ageing in 465 normal adult human brains. *NeuroImage*, 14(1 Pt 1):21–36.
- [101] Gorgolewski, K. J., Lurie, D., Urchs, S., Kipping, J. A., Craddock, R. C., Milham, M. P., Margulies, D. S., and Smallwood, J. (2014). A Correspondence between Individual Differences in the Brain’s Intrinsic Functional Architecture and the Content and Form of Self-Generated Thoughts. *PLoS ONE*, 9(5):e97176.
- [102] Goutte, C., Nielsen, F., and Hansen, K. (2000). Modeling the hemodynamic response in fMRI using smooth FIR filters. *IEEE Transactions on Medical Imaging*, 19(12):1188–1201.
- [103] Gray, M. A., Beacher, F. D., Minati, L., Nagai, Y., Kemp, A. H., Harrison, N. A., and Critchley, H. D. (2012). Emotional appraisal is influenced by cardiac afferent information. *Emotion*, 12(1):180–191.
- [104] Gray, R. M. (2006). Toeplitz and circulant matrices: A review. *Foundations and Trends[®] in Communications and Information Theory*, 2(3):155–239.
- [105] Greicius, M. D., Krasnow, B., Reiss, A. L., and Menon, V. (2003). Functional connectivity in the resting brain: a network analysis of the default mode hypothesis. *Proceedings of the National Academy of Sciences of the United States of America*, 100(1):253–8.

- [106] Greitz, D., Wirestam, R., Franck, A., Nordell, B., Thomsen, C., and Ståhlberg, F. (1992). Pulsatile brain movement and associated hydrodynamics studied by magnetic resonance phase imaging. *Neuroradiology*, 34(5):370–380.
- [107] Griswold, M. A., Jakob, P. M., Heidemann, R. M., Nittka, M., Jellus, V., Wang, J., Kiefer, B., and Haase, A. (2002). Generalized autocalibrating partially parallel acquisitions (GRAPPA). *Magnetic resonance in medicine*, 47(6):1202–1210.
- [108] Gross, S., Barmet, C., Dietrich, B. E., Brunner, D. O., Schmid, T., and Pruessmann, K. P. (2016). Dynamic nuclear magnetic resonance field sensing with part-per-trillion resolution. *Nature Communications*, 7(1):13702.
- [109] Grossman, P. (1992). Respiratory and cardiac rhythms as windows to central and autonomic biobehavioral regulation: Selection of window frames, keeping the panes clean and viewing the neural topography. *Biological Psychology*, 34(2):131 – 161.
- [110] Haacke, E. M., Brown, R. W., Thompson, M. R., and Venkatesan, R. (1999). *Magnetic Resonance Imaging: Physical Principles and Sequence Design*. Wiley.
- [111] Hagberg, G. E., Bianciardi, M., Brainovich, V., Cassarà, A. M., and Maraviglia, B. (2008). The effect of physiological noise in phase functional magnetic resonance imaging: from blood oxygen level-dependent effects to direct detection of neuronal currents. *Magnetic Resonance Imaging*, 26(7):1026–1040.
- [112] Hagberg, G. E., Bianciardi, M., Brainovich, V., Cassara, A. M., and Maraviglia, B. (2012). Phase stability in fMRI time series: Effect of noise regression, off-resonance correction and spatial filtering techniques. *NeuroImage*, 59(4):3748–3761.
- [113] Hahn, E. L. (1950). Spin echoes. *Phys. Rev.*, 80:580–594.
- [114] Harris, A. D., Ide, K., Poulin, M. J., and Frayne, R. (2006). Control of end-tidal PCO₂ reduces middle cerebral artery blood velocity variability: Implications for physiological neuroimaging. *NeuroImage*, 29(4):1272–1277.
- [115] Harrison, B. J., Pujol, J., Ortiz, H., Fornito, A., Pantelis, C., and Yücel, M. (2008). Modulation of Brain Resting-State Networks by Sad Mood Induction. *PLoS ONE*, 3(3):e1794.
- [116] Harvey, A. K., Pattinson, K. T., Brooks, J. C., Mayhew, S. D., Jenkinson, M., and Wise, R. G. (2008). Brainstem functional magnetic resonance imaging: Disentangling signal from physiological noise. *Journal of Magnetic Resonance Imaging*, 28(6):1337–1344.
- [117] Hassanpour, M. S., Yan, L., Wang, D. J., Lapidus, R. C., Arevian, A. C., Kyle Simmons, W., Feusner, J. D., and Khalsa, S. S. (2016). How the heart speaks to the brain: Neural activity during cardiorespiratory interoceptive stimulation. *Philosophical Transactions of the Royal Society B: Biological Sciences*, 371(1708).
- [118] Hegde, V., Deekshit, R., and P.S, S. (2013). Heart rate variability analysis for abnormality detection using time frequency distribution - smoothed pseudo winger ville method. pages 23–32.
- [119] Henry, P.-G., van de Moortele, P.-F., Giacomini, E., Nauerth, A., and Bloch, G. (1999). Field-frequency locked in vivo proton MRS on a whole-body spectrometer. *Magnetic Resonance in Medicine*, 42(4):636–642.
- [120] Holodny, A. I., Hou, B. L., and Hou, B. L. (2019). Physical Principles of BOLD fMRI- What Is Important for the Clinician. In *Functional Neuroimaging*, pages 1–11. CRC Press.

- [121] Hu, X. and Kim, S. G. G. (1994). Reduction of signal fluctuation in functional MRI using navigator echoes. *Magnetic Resonance in Medicine*, 31(5):495–503.
- [122] Hu, X., Le, T. H., Parrish, T., and Erhard, P. (1995). Retrospective estimation and correction of physiological fluctuation in functional MRI. *Magn Reson Med*, 34(2):201–212.
- [123] Huettel, S. A., Song, A. W., and McCarthy, G. (2009). *Functional Magnetic Resonance Imaging*.
- [124] Huettel, S. A., Song, A. W., and McCarthy, G. (2014). *Functional Magnetic Resonance Imaging, Third Edition*.
- [125] Hutchison, R. M., Womelsdorf, T., Allen, E. A., Bandettini, P. A., Calhoun, V. D., Corbetta, M., Della Penna, S., Duyn, J. H., Glover, G. H., Gonzalez-Castillo, J., Handwerker, D. A., Keilholz, S., Kiviniemi, V., Leopold, D. A., de Pasquale, F., Sporns, O., Walter, M., and Chang, C. (2013). Dynamic functional connectivity: Promise, issues, and interpretations. *NeuroImage*, 80:360–378.
- [126] Hyvärinen, A. and Oja, E. (2000). Independent component analysis: algorithms and applications. *Neural networks : the official journal of the International Neural Network Society*, 13(4-5):411–430.
- [127] Iacovella, V. and Hasson, U. (2011). The relationship between BOLD signal and autonomic nervous system functions: implications for processing of "physiological noise". *Magn Reson Imaging*, 29(10):1338–1345.
- [128] Jennings, J. R., Sheu, L. K., Kuan, D. C.-H., Manuck, S. B., and Gianaros, P. J. (2016). Resting state connectivity of the medial prefrontal cortex covaries with individual differences in high-frequency heart rate variability. *Psychophysiology*, 53(4):444–54.
- [129] Jerath, R. and Crawford, M. W. (2015). Layers of human brain activity: a functional model based on the default mode network and slow oscillations. *Frontiers in Human Neuroscience*, 9:248.
- [130] Jezzard, P. (1999). Physiological noise: strategies for correction. *Functional MRI*. New York: Springer, pages 173–182.
- [131] Jo, H. J., Saad, Z. S., Simmons, W. K., Milbury, L. A., and Cox, R. W. (2010). Mapping sources of correlation in resting state fMRI, with artifact detection and removal. *Neuroimage*, 52(2):571–582.
- [132] Julius, S. (1988). Transition from high cardiac output to elevated vascular resistance in hypertension. *American heart journal*, 116(2 Pt 2):600–606.
- [133] Kalisch, R., Elbel, G.-K., Gössl, C., Czisch, M., and Auer, D. P. (2001). Blood Pressure Changes Induced by Arterial Blood Withdrawal Influence Bold Signal in Anesthetized Rats at 7 Tesla: Implications for Pharmacologic MRI. *NeuroImage*, 14(4):891–898.
- [134] Kasper, L., Bollmann, S., Diaconescu, A. O., Hutton, C., Heinzle, J., Iglesias, S., Hauser, T. U., Sebold, M., Manjaly, Z. M., Pruessmann, K. P., and Stephan, K. E. (2017). The PhysIO Toolbox for Modeling Physiological Noise in fMRI Data. *Journal of Neuroscience Methods*, 276:56–72.
- [135] Katura, T., Tanaka, N., Obata, A., Sato, H., and Maki, A. (2006). Quantitative evaluation of interrelations between spontaneous low-frequency oscillations in cerebral hemodynamics and systemic cardiovascular dynamics. *NeuroImage*, 31(4):1592–1600.

- [136] Kay, K., Jamison, K. W., Vizioli, L., Zhang, R., Margalit, E., and Ugurbil, K. (2019). A critical assessment of data quality and venous effects in sub-millimeter fmri. *NeuroImage*, 189:847 – 869.
- [137] Khalili-Mahani, N., Chang, C., van Osch, M. J., Veer, I. M., van Buchem, M. A., Dahan, A., Beckmann, C. F., van Gerven, J. M., and Rombouts, S. A. (2013). The impact of "physiological correction" on functional connectivity analysis of pharmacological resting state fMRI. *NeuroImage*, 65:499–510.
- [138] Kilpatrick, L. A., Suyenobu, B. Y., Smith, S. R., Bueller, J. A., Goodman, T., Creswell, J. D., Tillisch, K., Mayer, E. A., and Naliboff, B. D. (2011). Impact of Mindfulness-Based Stress Reduction training on intrinsic brain connectivity. *NeuroImage*, 56(1):290–8.
- [139] Koh, J., Brown, T. E., Beightol, L. A., Ha, C. Y., and Eckberg, D. L. (1994). Human autonomic rhythms: vagal cardiac mechanisms in tetraplegic subjects. *The Journal of physiology*, 474(3):483–95.
- [140] Kong, Y., Jenkinson, M., Andersson, J., Tracey, I., and Brooks, J. C. W. (2012). Assessment of physiological noise modelling methods for functional imaging of the spinal cord. *Neuroimage*, 60(2):1538–1549.
- [141] Kumral, D., Schaare, H., Beyer, F., Reinelt, J., Uhlig, M., Liem, F., Lampe, L., Babayan, A., Reiter, A., Erbey, M., Roebbig, J., Loeffler, M., Schroeter, M., Husser, D., Witte, A., Villringer, A., and Gaebler, M. (2019). The age-dependent relationship between resting heart rate variability and functional brain connectivity. *NeuroImage*, 185:521 – 533.
- [142] Kwong, K. K., Belliveau, J. W., Chesler, D. A., Goldberg, I. E., Weisskoff, R. M., Poncelet, B. P., Kennedy, D. N., Hoppel, B. E., Cohen, M. S., and Turner, R. (1992). Dynamic magnetic resonance imaging of human brain activity during primary sensory stimulation. *Proc Natl Acad Sci USA*, 89(12):5675–5679.
- [143] Larkman, D. J., Hajnal, J. V., Herlihy, A. H., Coutts, G. A., Young, I. R., and Ehnholm, G. (2001). Use of multicoil arrays for separation of signal from multiple slices simultaneously excited. *Journal of Magnetic Resonance Imaging*, 13(2):313–317.
- [144] Laumann, T., Gordon, E., Adeyemo, B., Snyder, A., Joo, S., Chen, M.-Y., Gilmore, A., McDermott, K., Nelson, S., Dosenbach, N., Schlaggar, B., Mumford, J., Poldrack, R., and Petersen, S. (2015). Functional system and areal organization of a highly sampled individual human brain. *Neuron*, 87(3):657 – 670.
- [145] Laumann, T. O., Snyder, A. Z., Mitra, A., Gordon, E. M., Gratton, C., Adeyemo, B., Gilmore, A. W., Nelson, S. M., Berg, J. J., Greene, D. J., McCarthy, J. E., Tagliazucchi, E., Laufs, H., Schlaggar, B. L., Dosenbach, N. U. F., and Petersen, S. E. (2017). On the Stability of BOLD fMRI Correlations. *Cerebral Cortex*, 27(10):4719–4732.
- [146] Lauterbur, P. C. (1973). Image Formation by Induced Local Interactions: Examples Employing Nuclear Magnetic Resonance. *Nature*, 242(5394):190–191.
- [147] Lee, A. T., Glover, G. H., and Meyer, C. H. (1995). Discrimination of Large Venous Vessels in Time-Course Spiral Blood-Oxygen-Level-Dependent Magnetic-Resonance Functional Neuroimaging. *Magnetic Resonance in Medicine*, 33(6):745–754.
- [148] Lehrer, P., Vaschillo, B., Zucker, T., Graves, J., Katsamanis, M., Aviles, M., and Wamboldt, F. (2013). Protocol for heart rate variability biofeedback training. *Biofeedback*, 41(3):98–109.

- [149] Lewis, L. D., Setsompop, K., Rosen, B. R., and Polimeni, J. R. (2016). Fast fmri can detect oscillatory neural activity in humans. *Proceedings of the National Academy of Sciences*, 113(43):E6679–E6685.
- [150] Lim, C. L., Rennie, C., Barry, R. J., Bahramali, H., Lazzaro, I., Manor, B., and Gordon, E. (1997). Decomposing skin conductance into tonic and phasic components. *International journal of psychophysiology : official journal of the International Organization of Psychophysiology*, 25(2):97–109.
- [151] Lin, A., Liu, K. K. L., Bartsch, R. P., and Ivanov, P. C. (2016). Delay-correlation landscape reveals characteristic time delays of brain rhythms and heart interactions. *Philosophical Transactions of the Royal Society of London A: Mathematical, Physical and Engineering Sciences*, 374(2067).
- [152] Lin, F.-H., Chu, Y.-H., Hsu, Y.-C., Lin, J.-F. L., Tsai, K. W.-K., Tsai, S.-Y., and Kuo, W.-J. (2015). Significant feed-forward connectivity revealed by high frequency components of bold fmri signals. *NeuroImage*, 121:69 – 77.
- [153] Logothetis, N. K. (2008). What we can do and what we cannot do with fMRI. *Nature*, 453:869.
- [154] Logothetis, N. K., Pauls, J., Augath, M., Trinath, T., and Oeltermann, A. (2001). Neurophysiological investigation of the basis of the fMRI signal. *Nature*, 412(6843):150–157.
- [155] Lowe, M. J., Mock, B. J., and Sorenson, J. A. (1998). Functional connectivity in single and multislice echoplanar imaging using resting-state fluctuations. *NeuroImage*, 7(2):119–132.
- [156] Lund, T. E. (2001). fcmri—mapping functional connectivity or correlating cardiac-induced noise?. *Magnetic Resonance in Medicine*, 46(3):628–628.
- [157] Lund, T. E., Madsen, K. H., Sidaros, K., Luo, W.-L., and Nichols, T. E. (2006). Non-white noise in fMRI: does modelling have an impact?. *Neuroimage*, 29(1):54–66.
- [158] Maldjian, J. A., Laurienti, P. J., and Burdette, J. H. (2004). Precentral gyrus discrepancy in electronic versions of the Talairach atlas. *NeuroImage*, 21(1):450–5.
- [159] Maldjian, J. A., Laurienti, P. J., Kraft, R. A., and Burdette, J. H. (2003). An automated method for neuroanatomic and cytoarchitectonic atlas-based interrogation of fMRI data sets. *NeuroImage*, 19(3):1233–9.
- [160] Malik, M., Bigger, J. T., Camm, A. J., Kleiger, R. E., Malliani, A., Moss, A. J., and Schwartz, P. J. (1996). Heart rate variability: Standards of measurement, physiological interpretation, and clinical use. *European Heart Journal*, 17(3):354–381.
- [161] Mandeville, J. B., Marota, J. J., Ayata, C., Zaharchuk, G., Moskowitz, M. A., Rosen, B. R., and Weisskoff, R. M. (1999). Evidence of a cerebrovascular postarteriole windkessel with delayed compliance. *Journal of cerebral blood flow and metabolism : official journal of the International Society of Cerebral Blood Flow and Metabolism*, 19(6):679–689.
- [162] Mansfield, P. and Grannell, P. K. (1973). NMR diffraction in solids?. *Journal of Physics C: Solid State Physics*, 6(22):L422–L426.
- [163] Mansfield, P. and Maudsley, A. A. (1976). Line scan proton spin imaging in biological structures by NMR. *Physics in medicine and biology*, 21(5):847–852.
- [164] Mather, M. and Thayer, J. F. (2018). How heart rate variability affects emotion regulation brain networks. *Current Opinion in Behavioral Sciences*, 19:98–104.

- [165] Mayer, S. (1876). Studien zur Physiologie des Herzens und der Blutgefäße: 5. Abhandlung: Über spontane Blutdruckschwankungen. *Sber Akad Wiss Wien*, 74:281–307.
- [166] Menon, R. S., Ogawa, S., Hu, X., Strupp, J. P., Anderson, P., and Uğurbil, K. (1995). BOLD based functional MRI at 4 Tesla includes a capillary bed contribution: echo-planar imaging correlates with previous optical imaging using intrinsic signals. *Magnetic resonance in medicine*, 33(3):453–9.
- [167] Millar-Craig, M., Bishop, C., and Raftery, E. (1978). Circadian variation of blood pressure. *The Lancet*, 311(8068):795 – 797. Originally published as Volume 1, Issue 8068.
- [168] Milun, D. and Sher, D. (1993). Improving sampled probability distributions for Markov random fields. *Pattern Recognition Letters*, 14(10):781–788.
- [169] Mitra, P. and Pesaran, B. (1999). Analysis of dynamic brain imaging data. *Biophysical Journal*, 76(2):691 – 708.
- [170] Monfredi, O., Lyashkov, A. E., Johnsen, A.-B., Inada, S., Schneider, H., Wang, R., Nirmalan, M., Wisloff, U., Maltsev, V. A., Lakatta, E. G., Zhang, H., and Boyett, M. R. (2014). Biophysical Characterization of the Underappreciated and Important Relationship Between Heart Rate Variability and Heart Rate Novelty and Significance. *Hypertension*, 64(6):1334–1343.
- [171] Mulcahy, J. S., Larsson, D. E., Garfinkel, S. N., and Critchley, H. D. (2019). Heart rate variability as a biomarker in health and affective disorders: A perspective on neuroimaging studies. *NeuroImage*, 202:116072.
- [172] Mullinger, K. J., Cherukara, M. T., Buxton, R. B., Francis, S. T., and Mayhew, S. D. (2017). Post-stimulus fMRI and EEG responses: Evidence for a neuronal origin hypothesised to be inhibitory. *NeuroImage*, 157:388–399.
- [173] Murphy, K., Birn, R. M., and Bandettini, P. A. (2013). Resting-state fMRI confounds and cleanup. *Neuroimage*, 80:349–359.
- [174] Myers, C. W., Cohen, M. A., Eckberg, D. L., and Taylor, J. A. (2001). A model for the genesis of arterial pressure Mayer waves from heart rate and sympathetic activity. *Autonomic Neuroscience: Basic and Clinical*, 91(1-2):62–75.
- [175] Nakai, T., Matsuo, K., Kato, C., Takehara, Y., Isoda, H., Moriya, T., Okada, T., and Sakahara, H. (2000). Post-stimulus response in hemodynamics observed by functional magnetic resonance imaging—difference between the primary sensorimotor area and the supplementary motor area. *Magnetic Resonance Imaging*, 18(10):1215–1219.
- [176] Napadow, V., Dhond, R., Conti, G., Makris, N., Brown, E. N., and Barbieri, R. (2008). Brain correlates of autonomic modulation: combining heart rate variability with fMRI. *NeuroImage*, 42(1):169–177.
- [177] Nikolaou, F., Orphanidou, C., Papakyriakou, P., Murphy, K., Wise, R. G., and Mitsis, G. D. (2016). Spontaneous physiological variability modulates dynamic functional connectivity in resting-state functional magnetic resonance imaging. *Philosophical Transactions of the Royal Society A: Mathematical, Physical and Engineering Sciences*, 374(2067):20150183.
- [178] Nitzan, M., Babchenko, A., Khanokh, B., and Landau, D. (1998). The variability of the photoplethysmographic signal - A potential method for the evaluation of the autonomic nervous system. *Physiological Measurement*, 19(1):93–102.

- [179] Nitzan, M., de Boer, H., Turivnenko, S., Babchenko, A., and Sapoznikov, D. (1994). Power spectrum analysis of spontaneous fluctuations in the photoplethysmographic signal. *Journal of Basic and Clinical Physiology and Pharmacology*, 5(3-4):269–276.
- [180] Nocedal, J. and Wright, S. J. (2006). *Quadratic Programming*, pages 448–492. Springer New York, New York, NY.
- [181] Noll, D. and Schneider, W. (1994). Respiration Artifacts in functional Brain Imaging : Sources of Signal Variation and Compensation Strategies. *Proceedings, 2nd Society of Magnetic Resonance*, 647.
- [182] Norton, K. N., Luchyshyn, T. A., and Kevin Shoemaker, J. (2013). Evidence for a medial prefrontal cortex–hippocampal axis associated with heart rate control in conscious humans. *Brain Research*, 1538:104–115.
- [183] Nunes, R. G., Hajnal, J. V., Golay, X., and Larkman, D. J. (2006). Simultaneous slice excitation and reconstruction for single shot EPI. *Proceedings of the 14th Annual Meeting of ISMRM*.
- [184] Ogawa, S., Lee, T. M., Kay, A. R., and Tank, D. W. (1990a). Brain magnetic resonance imaging with contrast dependent on blood oxygenation. *Biophysics*, 87:9868–9872.
- [185] Ogawa, S., Lee, T.-M., Nayak, A. S., and Glynn, P. (1990b). Oxygenation-sensitive contrast in magnetic resonance image of rodent brain at high magnetic fields. *Magnetic Resonance in Medicine*, 14(1):68–78.
- [186] Ogawa, S., Tank, D. W., Menon, R., Ellermann, J. M., Kim, S. G., Merkle, H., and Ugurbil, K. (1992). Intrinsic signal changes accompanying sensory stimulation: functional brain mapping with magnetic resonance imaging. *Proc Natl Acad Sci USA*, 89(13):5951–5955.
- [187] Otzenberger, H., Gronfier, C., Simon, C., Charloux, A., Ehrhart, J., Piquard, F., and Brandenberger, G. (1998). Dynamic heart rate variability: a tool for exploring sympathovagal balance continuously during sleep in men. *American Journal of Physiology-Heart and Circulatory Physiology*, 275(3):H946–H950.
- [188] Palatini, P. (2005). Treatment of tachycardia in hypertension: Where do we stand now?. *Current Hypertension Reviews*, 1(2):129–140.
- [189] Palatini, P. and Julius, S. (1997). Heart rate and the cardiovascular risk. *Journal of hypertension*, 15(1):3–17.
- [190] Parrish, T. B., Gitelman, D. R., LaBar, K. S., and Mesulam, M.-M. (2000). Impact of signal-to-noise on functional mri. *Magnetic Resonance in Medicine*, 44(6):925–932.
- [191] Patterson, J. C., Ungerleider, L. G., and Bandettini, P. A. (2002). Task-Independent Functional Brain Activity Correlation with Skin Conductance Changes: An fMRI Study. *NeuroImage*, 17(4):1797–1806.
- [192] Peebles, K., Celi, L., McGrattan, K., Murrell, C., Thomas, K., and Ainslie, P. N. (2007). Human cerebrovascular and ventilatory CO₂ reactivity to end-tidal, arterial and internal jugular vein P_{CO₂}. *The Journal of Physiology*, 584(1):347–357.
- [193] Penny, W., Kiebel, S., and Friston, K. (2003). Variational bayesian inference for fmri time series. *NeuroImage*, 19(3):727 – 741.

- [194] Pfurtscheller, G., Klobassa, D. S., Altstatter, C., Bauernfeind, G., and Neuper, C. (2011). About the stability of phase shifts between slow oscillations around 0.1 Hz in cardiovascular and cerebral systems. *IEEE transactions on bio-medical engineering*, 58(7):2064–2071.
- [195] Pfurtscheller, G., Schwerdtfeger, A. R., Seither-Preisler, A., Brunner, C., Stefan Aigner, C., Brito, J., Carmo, M. P., and Andrade, A. (2017). Brain–heart communication: Evidence for “central pacemaker” oscillations with a dominant frequency at 0.1 Hz in the cingulum. *Clinical Neurophysiology*, 128(1):183–193.
- [196] Poldrack, R. A., Mumford, J. A., and Nichols, T. E. (2011). *Handbook of Functional MRI Data Analysis*. Cambridge University Press.
- [197] Pollatos, O., Schandry, R., Auer, D. P., and Kaufmann, C. (2007). Brain structures mediating cardiovascular arousal and interoceptive awareness. *Brain Research*, 1141(1):178–187.
- [198] Poser, B. A. and Setsompop, K. (2018). Pulse sequences and parallel imaging for high spatiotemporal resolution mri at ultra-high field. *NeuroImage*, 168:101 – 118. Neuroimaging with Ultra-high Field MRI: Present and Future.
- [199] Power, J. D., Plitt, M., Laumann, T. O., and Martin, A. (2017). Sources and implications of whole-brain fMRI signals in humans. *NeuroImage*, 146:609–625.
- [200] Purcell, E. M., Torrey, H. C., and Pound, R. V. (1946). Resonance absorption by nuclear magnetic moments in a solid. *Phys. Rev.*, 69:37–38.
- [201] Raichle, M. E. (1994). Visualizing the Mind: strategies of cognitive science and techniques of modern brain imaging open a window to the neural systems responsible for thought. *Scientific American*, 48(April):35–39.
- [202] Raichle, M. E., MacLeod, A. M., Snyder, A. Z., Powers, W. J., Gusnard, D. A., and Shulman, G. L. (2001). A default mode of brain function. *Proceedings of the National Academy of Sciences*, 98(2):676–682.
- [203] Raj, D., Anderson, A. W., and Gore, J. C. (2001). Respiratory effects in human functional magnetic resonance imaging due to bulk susceptibility changes. *Phys Med Biol*, 46(12):3331–3340.
- [204] Rayshubskiy, A., Wojtasiewicz, T. J., Mikell, C. B., Bouchard, M. B., Timerman, D., Youngerman, B. E., McGovern, R. A., Otten, M. L., Canoll, P., McKhann, G. M., and Hillman, E. M. (2014). Direct, intraoperative observation of ~ 0.1 Hz hemodynamic oscillations in awake human cortex: Implications for fMRI. *NeuroImage*, 87:323–331.
- [205] Reyes del Paso, G. A., Langewitz, W., Mulder, L. J. M., van Roon, A., and Duschek, S. (2013). The utility of low frequency heart rate variability as an index of sympathetic cardiac tone: A review with emphasis on a reanalysis of previous studies. *Psychophysiology*, 50(5):477–487.
- [206] Robbins, P. A., Conway, J., Cunningham, D. A., Khamnei, S., and Paterson, D. J. (1990). A comparison of indirect methods for continuous estimation of arterial PCO₂ in men. *Journal of Applied Physiology*, 68(4):1727–1731.
- [207] Roebroeck, A., Formisano, E., and Goebel, R. (2005). Mapping directed influence over the brain using Granger causality and fMRI. *NeuroImage*, 25(1):230–242.

- [208] Sacha, J., Barabach, S., Statkiewicz-Barabach, G., Sacha, K., Müller, A., Piskorski, J., Barthel, P., and Schmidt, G. (2014). Gender differences in the interaction between heart rate and its variability - How to use it to improve the prognostic power of heart rate variability. *International Journal of Cardiology*, 171(2):e42–e45.
- [209] Sakaki, M., Yoo, H. J., Nga, L., Lee, T. H., Thayer, J. F., and Mather, M. (2016). Heart rate variability is associated with amygdala functional connectivity with MPFC across younger and older adults. *NeuroImage*, 139:44–52.
- [210] Sano, A., Picard, R. W., and Stickgold, R. (2014). Quantitative analysis of wrist electrodermal activity during sleep. *International journal of psychophysiology : official journal of the International Organization of Psychophysiology*, 94(3):382–9.
- [211] Särkkä, S., Solin, A., Nummenmaa, A., Vehtari, A., Auranen, T., Vanni, S., and Lin, F.-H. (2012). Dynamic retrospective filtering of physiological noise in BOLD fMRI: DRIFTER. *NeuroImage*, 60(2):1517–1527.
- [212] Sasai, S., Homae, F., Watanabe, H., and Taga, G. (2011). Frequency-specific functional connectivity in the brain during resting state revealed by NIRS. *NeuroImage*, 56(1):252–257.
- [213] Saul, J. P. (1990). Beat-To-Beat Variations of Heart Rate Reflect Modulation of Cardiac Autonomic Outflow. *Physiology*, 5(1):32–37.
- [214] Saul, J. P., Berger, R. D., Albrecht, P., Stein, S. P., Chen, M. H., and Cohen, R. J. (1991). Transfer function analysis of the circulation: unique insights into cardiovascular regulation. *American Journal of Physiology-Heart and Circulatory Physiology*, 261(4):H1231–H1245.
- [215] Scheuer, J. and Tipton, C. M. (1977). Cardiovascular Adaptations to Physical Training. *Annual Review of Physiology*, 39(1):221–251.
- [216] Schölvinck, M. L., Maier, A., Ye, F. Q., Duyn, J. H., and Leopold, D. A. (2010). Neural basis of global resting-state fMRI activity. *Proc Natl Acad Sci USA*, 107(22):10238–10243.
- [217] Schumann, A., Andrack, C., and Bär, K.-J. (2017). Differences of sympathetic and parasympathetic modulation in major depression. *Progress in Neuro-Psychopharmacology and Biological Psychiatry*, 79:324 – 331.
- [218] Seth, A. K., Chorley, P., and Barnett, L. C. (2013). Granger causality analysis of fMRI BOLD signals is invariant to hemodynamic convolution but not downsampling. *NeuroImage*, 65:540–555.
- [219] Sheehan, D. V., Lecrubier, Y., Sheehan, K. H., Amorim, P., Janavs, J., Weiller, E., Hergueta, T., Baker, R., and Dunbar, G. C. (1998). The Mini-International Neuropsychiatric Interview (M.I.N.I.): the development and validation of a structured diagnostic psychiatric interview for DSM-IV and ICD-10. *J Clin Psychiatry*, 59 Suppl 2:22–57.
- [220] Shine, J. M., Koyejo, O., Bell, P. T., Gorgolewski, K. J., Gilat, M., and Poldrack, R. A. (2015). Estimation of dynamic functional connectivity using Multiplication of Temporal Derivatives. *NeuroImage*, 122:399–407.
- [221] Shmueli, K., van Gelderen, P., de Zwart, J. A., Horovitz, S. G., Fukunaga, M., Jansma, J. M., and Duyn, J. H. (2007). Low-frequency fluctuations in the cardiac rate as a source of variance in the resting-state fMRI BOLD signal. *Neuroimage*, 38(2):306–320.
- [222] Shoemaker, J. K., Norton, K. N., Baker, J., and Luchyshyn, T. (2015). Forebrain organization for autonomic cardiovascular control. *Autonomic Neuroscience: Basic and Clinical*, 188:5–9.

- [223] Sin, P. Y. W., Webber, M. R., Galletly, D. C., and Tzeng, Y. C. (2012). Relationship between cardioventilatory coupling and pulmonary gas exchange. *Clinical Physiology and Functional Imaging*, 32(6):476–480.
- [224] Sladky, R., Friston, K. J., Tröstl, J., Cunnington, R., Moser, E., and Windischberger, C. (2011). Slice-timing effects and their correction in functional mri. *NeuroImage*, 58(2):588 – 594.
- [225] Smith, A. M., Lewis, B. K., Ruttimann, U. E., Ye, F. Q., Sinnwell, T. M., Yang, Y., Duyn, J. H., Frank, J. A., Frank, Q. Y., Sinnwell, T. M., Yang, Y., Duyn, J. H., Frank, J. A., Ye, F. Q., Sinnwell, T. M., Yang, Y., Duyn, J. H., and Frank, J. A. (1999). Investigation of low frequency drift in fMRI signal. *NeuroImage*, 9(5):526–533.
- [226] Smith, R. P., Veale, D., Pépin, J.-L., and Lévy, P. A. (1998). Obstructive sleep apnoea and the autonomic nervous system. *Sleep Medicine Reviews*, 2(2):69–92.
- [227] Spodick, D. H., Raju, P., Bishop, R. L., and Rifkin, R. D. (1992). Operational definition of normal sinus heart rate. *The American journal of cardiology*, 69(14):1245–1246.
- [228] Starck, T., Remes, J., Nikkinen, J., Tervonen, O., and Kiviniemi, V. (2010). Correction of low-frequency physiological noise from the resting state BOLD fMRI-Effect on ICA default mode analysis at 1.5 T. *Journal of Neuroscience Methods*, 186(2):179–185.
- [229] Streeter, C., Gerbarg, P., Saper, R., Ciraulo, D., and Brown, R. (2012). Effects of yoga on the autonomic nervous system, gamma-aminobutyric-acid, and allostasis in epilepsy, depression, and post-traumatic stress disorder. *Medical Hypotheses*, 78(5):571–579.
- [230] Subasi, A. (2019). Chapter 2 - biomedical signals. In Subasi, A., editor, *Practical Guide for Biomedical Signals Analysis Using Machine Learning Techniques*, pages 27 – 87. Academic Press.
- [231] Sun, F. T., Miller, L. M., and D’Esposito, M. (2004). Measuring interregional functional connectivity using coherence and partial coherence analyses of fMRI data. *NeuroImage*, 21(2):647–658.
- [232] Tagliazucchi, E. and Laufs, H. (2014). Decoding Wakefulness Levels from Typical fMRI Resting-State Data Reveals Reliable Drifts between Wakefulness and Sleep. *Neuron*, 82(3):695–708.
- [233] Tagliazucchi, E., von Wegner, F., Morzelewski, A., Borisov, S., Jahnke, K., and Laufs, H. (2012). Automatic sleep staging using fMRI functional connectivity data. *NeuroImage*, 63(1):63–72.
- [234] Talairach, J. and Tournoux, P. (1988). *Co-planar Stereotaxic Atlas of the Human Brain: 3-dimensional Proportional System : an Approach to Cerebral Imaging*. Thieme classics. G. Thieme.
- [235] Tang, Y. Y., Rothbart, M. K., and Posner, M. I. (2012). Neural correlates of establishing, maintaining, and switching brain states. *Trends in Cognitive Sciences*, 16(6):330–337.
- [236] Thayer, J. F., Åhs, F., Fredrikson, M., Sollers, J. J., and Wager, T. D. (2012). A meta-analysis of heart rate variability and neuroimaging studies: Implications for heart rate variability as a marker of stress and health. *Neuroscience & Biobehavioral Reviews*, 36(2):747–756.
- [237] Thayer, J. F. and Lane, R. D. (2000). A model of neurovisceral integration in emotion regulation and dysregulation. *Journal of Affective Disorders*, 61(3):201–216.

- [238] Thayer, J. F. and Lane, R. D. (2009). Claude bernard and the heart–brain connection: Further elaboration of a model of neurovisceral integration. *Neuroscience & Biobehavioral Reviews*, 33(2):81 – 88.
- [239] Thomson, D. (1982). Spectrum estimation and harmonic analysis. *Proceedings of the IEEE*, 70(9):1055–1096.
- [240] Toma, K., Honda, M., Hanakawa, T., Okada, T., Fukuyama, H., Ikeda, A., Nishizawa, S., Konishi, J., and Shibasaki, H. (1999). Activities of the primary and supplementary motor areas increase in preparation and execution of voluntary muscle relaxation: an event-related fMRI study. *The Journal of neuroscience : the official journal of the Society for Neuroscience*, 19(9):3527–3534.
- [241] Tong, Y., Hocke, L. M., Fan, X., Janes, A. C., and deB Frederick, B. (2015). Can apparent resting state connectivity arise from systemic fluctuations?. *Frontiers in Human Neuroscience*.
- [242] Triantafyllou, C., Hoge, R., Krueger, G., Wiggins, C., Potthast, A., Wiggins, G., and Wald, L. (2005). Comparison of physiological noise at 1.5 t, 3 t and 7 t and optimization of fmri acquisition parameters. *NeuroImage*, 26(1):243 – 250.
- [243] Triantafyllou, C., Polimeni, J. R., and Wald, L. L. (2011). Physiological noise and signal-to-noise ratio in fMRI with multi-channel array coils. *NeuroImage*, 55(2):597–606.
- [244] Tung, K.-C., Uh, J., Mao, D., Xu, F., Xiao, G., and Lu, H. (2013). Alterations in resting functional connectivity due to recent motor task. *NeuroImage*, 78:316–324.
- [245] Van Buuren, M., Gladwin, T. E., Zandbelt, B. B., Van Den Heuvel, M., Ramsey, N. F., Kahn, R. S., and Vink, M. (2009). Cardiorespiratory effects on default-mode network activity as measured with fMRI. *Human Brain Mapping*, 30(9):3031–3042.
- [246] Van den Aardweg, J. G. and Karemaker, J. M. (2002). Influence of chemoreflexes on respiratory variability in healthy subjects. *Am J Respir Crit Care Med*, 165(8):1041–1047.
- [247] Van Essen, D. C., Smith, S. M., Barch, D. M., Behrens, T. E., Yacoub, E., and Ugurbil, K. (2013). The WU-Minn Human Connectome Project: An overview. *NeuroImage*, 80:62–79.
- [248] van Zijl, P. C. M., Hua, J., and Lu, H. (2012). The BOLD post-stimulus undershoot, one of the most debated issues in fMRI. *NeuroImage*, 62(2):1092–1102.
- [249] Vanhatalo, S., Palva, J. M., Holmes, M. D., Miller, J. W., Voipio, J., and Kaila, K. (2004). Infralow oscillations modulate excitability and interictal epileptic activity in the human cortex during sleep. *Proceedings of the National Academy of Sciences*, 101(14):5053–5057.
- [250] Vannesjo, S. J., Wilm, B. J., Duerst, Y., Gross, S., Brunner, D. O., Dietrich, B. E., Schmid, T., Barmet, C., and Pruessmann, K. P. (2015). Retrospective correction of physiological field fluctuations in high-field brain mri using concurrent field monitoring. *Magnetic Resonance in Medicine*, 73(5):1833–1843.
- [251] Verstynen, T. D. and Deshpande, V. (2011). Using pulse oximetry to account for high and low frequency physiological artifacts in the BOLD signal. *Neuroimage*, 55(4):1633–1644.
- [252] Windischberger, C., Langenberger, H., Sycha, T., Tschernko, E. M., Fuchsjäger-Mayerl, G., Schmetterer, L., and Moser, E. (2002). On the origin of respiratory artifacts in BOLD-EPI of the human brain. *Magnetic Resonance Imaging*, 20(8):575–582.

-
- [253] Wise, R. G., Ide, K., Poulin, M. J., and Tracey, I. (2004). Resting fluctuations in arterial carbon dioxide induce significant low frequency variations in BOLD signal. *Neuroimage*, 21(4):1652–1664.
- [254] Woolrich, M. W., Behrens, T. E., and Smith, S. M. (2004). Constrained linear basis sets for hrf modelling using variational bayes. *NeuroImage*, 21(4):1748 – 1761.
- [255] Wowk, B., McIntyre, M. C., and Saunders, J. K. (1997). k-Space detection and correction of physiological artifacts in fMRI. *Magnetic Resonance in Medicine*, 38(6):1029–1034.
- [256] Yuan, H., Zotev, V., Phillips, R., and Bodurka, J. (2013a). Correlated slow fluctuations in respiration, EEG, and BOLD fMRI. *NeuroImage*, 79:81–93.
- [257] Yuan, H., Zotev, V., Phillips, R., and Bodurka, J. (2013b). Correlated slow fluctuations in respiration, EEG, and BOLD fMRI. *NeuroImage*, 79:81–93.
- [258] Zar, J. H. (1996). *Biostatistical Analysis*. Prentice-Hall international editions. Prentice Hall.
- [259] Zhang, Z., Xu, Q., Liao, W., Wang, Z., Li, Q., Yang, F., Zhang, Z., Liu, Y., and Lu, G. (2015). Pathological uncoupling between amplitude and connectivity of brain fluctuations in epilepsy. *Human Brain Mapping*, 36(7):2756–2766.
- [260] Zile, M. R. (1992). Hemodynamic Determinants of Echocardiographically-Derived Indices of Left Ventricular Filling. *Echocardiography*, 9(3):289–300.

Index of Figures

2.1	Net magnetization and Zeeman effect	11
2.2	Schematic illustration of the magnetic field gradients	13
2.3	Pulse diagram of the spin-echo and gradient-echo sequences	14
2.4	GE-EPI pulse sequence and its k -space trajectory	15
2.5	The BOLD fMRI mechanism	16
2.6	Main sources of noise affecting the BOLD signal	21
2.7	Brain areas affected by cyclic respiratory and cardiac noise	22
2.8	Schematic illustration of popular physiological noise correction methods	27
2.9	Illustration of the definition of RVT/RV	30
2.10	Canonical cardiac response function proposed by Chang <i>et al.</i> [53]	33
3.1	Processing of physiological signals	38
3.2	Extraction of the HR regressor	40
3.3	Processing steps for analyzing HR and BOLD spectral powers	42
3.4	Location of posterior cingulate cortex seed region	47
3.5	Location of right amygdala seed region	48
4.1	Boxplot showing the heart rate groups	51

4.2	Group average PSDs of HRV and BOLD signal	53
4.3	Group-specific averaged CRFs	55
4.4	Group average R^2 maps after convolution with the canonical CRF	56
4.5	R^2 maps for three subjects after convolution with the canonical CRF	57
4.6	Group average R^2 maps after convolution with CRF_i	58
4.7	Group average R^2 maps after convolution with the CRF_g	59
4.8	R^2 maps for three subjects after convolution with the CRF_g	60
4.9	Group-specific CRF estimated from different brain regions	61
4.10	Comparison of CRF_g using different physiological noise correction methods . .	62
4.11	Group average R^2 maps obtained by using a “wrong” CRF_g	63
4.12	RMSD between individual CRFs and CRF_g	64
4.13	Individual CRF across subjects with different heart rates	65
4.14	Illustration of the HR-based CRF model	67
4.15	HR-based CRFs extracted from gray matter and cerebrospinal fluid	68
4.16	Functional connectivity differences of the right amygdala	71
4.17	Association between functional connectivity and heart rate	72
4.18	Effect of simulated cardiac aliasing on functional connectivity	74
A.1	Simulation of cardiac and BOLD signals	89

Index of Tables

3.1	Main demographic and physiological characteristics of the heart rate groups . . .	36
3.2	Group arrangements	37
3.3	Cardiac response functions	43
4.1	Demographic and physiological data	52
4.2	Variance explained by different cardiac response functions	61
4.3	Fit coefficients for HR-based CRFs	66
4.4	Average percentage reduction of voxels by different correction methods	69
4.5	Functional connectivity differences of the right amygdala	72
A.1	Variance explained at the individual level	90

Ehrenwörtliche Erklärung

Hiermit erkläre ich,

dass mir die Promotionsordnung der Medizinischen Fakultät der FriedrichSchiller-Universität bekannt ist,

ich die Dissertation selbst angefertigt habe und alle von mir benutzten Hilfsmittel, persönlichen Mitteilungen und Quellen in meiner Arbeit angegeben sind,

mich folgende Personen bei der Auswahl und Auswertung des Materials sowie bei der Herstellung des Manuskripts unterstützt haben: Prof. Dr. med. Karl-Jürgen Bär, Prof. Dr. Jürgen R. Reichenbach, Dr. Andy Schumann und Dr. Gerd Wagner,

die Hilfe eines Promotionsberaters nicht in Anspruch genommen wurde und dass Dritte weder unmittelbar noch mittelbar geldwerte Leistungen von mir für Arbeiten erhalten haben, die im Zusammenhang mit dem Inhalt der vorgelegten Dissertation stehen,

dass ich die Dissertation noch nicht als Prüfungsarbeit für eine staatliche oder andere wissenschaftliche Prüfung eingereicht habe und

dass ich die gleiche, eine in wesentlichen Teilen ähnliche oder eine andere Abhandlung nicht bei einer anderen Hochschule als Dissertation eingereicht habe.

Ort, Datum

Unterschrift des Verfassers

Acknowledgements

I would like to express my deepest gratitude to Prof. Dr. Kar-Jurgen Bär for his support, patience, and persistence. Thanks Prof. Bär for getting me to the end.

I am extremely thankful to Dr. Gerd Wagner for all the years under his guidance. Gerd encouraged me to learn more, to be curious, and inspired me to become a better scientist.

I owe a special debt of gratitude to my colleagues, specially, Dr. Andy Schumann. Thanks Andy for your support and help during the writing of the thesis and the many hours of conversation about exciting research topics.

Many words of thanks go to Prof. Dr. Jürgen R. Reichenbach for proofreading the thesis and providing valuable comments and suggestions.

Lastly, I give special thanks to my girlfriend Cecilia, who has always been there for me, with love and understanding. I feel so lucky to have met you in my life.

Curriculum Vitae

Name: Feliberto de la Cruz Monte de Oca

 [0000-0002-6529-2679](https://orcid.org/0000-0002-6529-2679)

E-mail: feliberto.cruz@uni-jena.de

 researchgate.net/profile/Feliberto_De_La_Cruz

Education and Work Experience

- 2015 - 2020** Ph.D. candidate at the Faculty of Medicine, Friedrich-Schiller-Universität Jena
- 2013 - present** Research Assistant at the *Lab for Autonomic Neuroscience, Imaging and Cognition (LANIC)*, Department of Psychosomatic Medicine and Psychotherapy, Universitätsklinikum Jena
- 2011 - 2012** Visiting Student at “Instituto de Neurociencias de Alicante” (IN), Alicante, Spain
- 2009 - 2012** Research Assistant at the Center for Advanced Studies of Cuba (CEAC), Havana, Cuba
- 2004 - 2009** Diploma of Energy and Nuclear Technologies Engineer, Higher Institute of Applied Science and Technologies (www.instec.cu), Havana, Cuba

Scientific Publications

1. **de la Cruz F.**, Schumann A., Köhler S., Reichenbach J. R., Wagner G., and Bär K.-J. (2019). “The relationship between heart rate and functional connectivity of brain regions involved in autonomic control.” *NeuroImage*, 196:318 - 328.
2. Bär K.-J., Köhler S., **de la Cruz F.**, Schumann A., Zepf F. D., and Wagner G. (2020). “Functional consequences of acute tryptophan depletion on raphe nuclei connectivity and network organization in healthy women.” *NeuroImage*, 207:116362.

-
3. Wagner G., **de la Cruz F.**, Köhler S., Pereira F., Richard-Devantoy S., Turecki G., Bär K.-J. & Jollant F. (2019). “Connectomics-Based Functional Network Alterations in both Depressed Patients with Suicidal Behavior and Healthy Relatives of Suicide Victims.” *Scientific Reports* 9(1).
 4. Wagner G., Köhler S., Peikert G., **de la Cruz F.**, Reess T. J., Rus O. G., Schultz C. C., Koch K., and Bär K.-J. (2019). “Checking and washing rituals are reflected in altered cortical thickness in obsessive-compulsive disorder.” *Cortex*, 117:147 - 156.
 5. Kahl M., Wagner G., **de la Cruz F.**, Köhler S., and Schultz C. C. (2018). “Resilience and cortical thickness: a MRI study.” *European Archives of Psychiatry and Clinical Neuroscience*.
 6. Schumann A., Köhler S., **de la Cruz F.**, Güllmar D., Reichenbach J. R., Wagner G., and Bär K.-J. (2018). “The Use of Physiological Signals in Brainstem/Midbrain fMRI.” *Frontiers in Neuroscience*, 12:718.
 7. Köhler S., Schumann A., **de la Cruz F.**, Wagner G., and Bär K.-J. (2018). “Towards response success prediction: An integrative approach using high-resolution fMRI and autonomic indices.” *Neuropsychologia*, 119:182-190.
 8. Wagner G., Krause-Utz A., **de la Cruz F.**, Schumann A., Schmahl C., and Bär K.-J. (2018). “Resting-state functional connectivity of neurotransmitter producing sites in female patients with borderline personality disorder.” *Progress in Neuro-Psychopharmacology and Biological Psychiatry*, 83:118-126.
 9. Wagner G., **de la Cruz F.**, Köhler S., and Bär K.-J. (2017). “Treatment Associated Changes of Functional Connectivity of Midbrain/Brainstem Nuclei in Major Depressive Disorder.” *Scientific Reports*, 7(1):8675.
 10. **de la Cruz F.**, Schumann A., Köhler S., Bär K.-J., and Wagner G. (2017). “Impact of the heart rate on the shape of the cardiac response function.” *NeuroImage*, 162:214-225.
 11. Wagner G., Herbsleb M., **de la Cruz F.**, Schumann A., Köhler S., Puta, C., Gabriel H. W., Reichenbach J. R., and Bär K.-J. (2017). “Changes in fMRI activation in anterior hippocampus and motor cortex during memory retrieval after an intense exercise intervention.” *Biological Psychology*, 124:65-78.
 12. Schultz C. C., Wagner G., **de la Cruz F.**, Berger S., Reichenbach J. R., Sauer H., and Bär K.-J. (2017). “Evidence for alterations of cortical folding in anorexia nervosa.” *European Archives of Psychiatry and Clinical Neuroscience*, 267(1):41-49.

-
13. Bär K.-J., Herbsleb M., Schumann A., **de la Cruz F.**, Gabriel H. W., and Wagner G. (2016). "Hippocampal-brainstem connectivity associated with vagal modulation after an intense exercise intervention in healthy men." *Frontiers in Neuroscience*, 10:145.
 14. Wagner G., Gussew A., Köhler S., **de la Cruz F.**, Smesny S., Reichenbach J. R., and Bär K.-J. (2016). "Resting state functional connectivity of the hippocampus along the anterior–posterior axis and its association with glutamatergic metabolism." *Cortex*, 81:104 - 117.
 15. Bär K.-J., **de la Cruz F.**, Schumann A., Köhler S., Sauer H., Critchley H., and Wagner G. (2016). "Functional connectivity and network analysis of midbrain and brainstem nuclei." *NeuroImage*, 134:53-63.
 16. Pester B., **de la Cruz F.**, Bar K., Witte H., and Leistriz L. (2016). "Detecting spatially highly resolved network modules: A multi subject approach." In *2016 38th Annual International Conference of the IEEE Engineering in Medicine and Biology Society (EMBC)*, pages 5481-5484.
 17. Wagner G., **de la Cruz F.**, Schachtzabel C., Güllmar D., Schultz C. C., Schlösser R. G., Bär K.-J., and Koch K. (2015). "Structural and functional dysconnectivity of the fronto-thalamic system in schizophrenia: A dcm-dti study." *Cortex*, 66:35 - 45.
 18. Bär K.-J., **de la Cruz F.**, Schumann A., and Wagner G. (2015). "Relation of autonomic measures to the default mode network." *Autonomic Neuroscience*, 192:11.
 19. Wagner G., Herbsleb M., **de la Cruz F.**, Schumann A., Brüner F., Schachtzabel C., Gussew A., Puta C., Smesny S., Gabriel H. W., Reichenbach J. R., and Bär K.-J. (2015). "Hippocampal Structure, Metabolism, and Inflammatory Response after a 6-Week Intense Aerobic Exercise in Healthy Young Adults: A Controlled Trial." *Journal of Cerebral Blood Flow & Metabolism*, 35(10):1570-1578.
 20. Bär K.-J., **de la Cruz F.**, Berger S., Schultz C. C., and Wagner G. (2015). "Structural and functional differences in the cingulate cortex relate to disease severity in anorexia nervosa." *Journal of psychiatry & neuroscience*, 40 4:269-79.
 21. Moreno A., Jago P., **de la Cruz F.**, and Canals S. (2013). "Neurophysiological, metabolic and cellular compartments that drive neurovascular coupling and neuroimaging signals." *Frontiers in neuroenergetics*, 5:3.

Conference Abstracts

1. **de la Cruz F.**, Schumann A., Köhler S., Wagner G., and Bär K.-J. “Causal relationships between neuromodulatory centers and DMN regions.” *Organization for Human Brain Mapping* (2019), Rome, Italy.
2. **de la Cruz F.**, Schumann A., Köhler S., Wagner G., and Bär K.-J. “Differences in resting state functional connectivity associated with heart rate regulation.” *Organization for Human Brain Mapping* (2018), Singapur.
3. **de la Cruz F.**, Schumann A., Köhler, S., Bär K.-J., and Wagner G. “Ultra-Fast vs Slow EPI Acquisition: Implications for Physiological Noise Correction.” *Organization for Human Brain Mapping* (2017), Vancouver, Canada.